

<b>OCRWM</b>	<b>MODEL COVER SHEET</b>	1. QA: QA Page 1 of 102
--------------	--------------------------	----------------------------

## 2. Type of Mathematical Model

Process Model       Abstraction Model       System Model

## Describe Intended Use of Model

Describes the methods used to determine hydrologic properties based on the available field data from the unsaturated zone at Yucca Mountain, Nevada, and documents validation of the active fracture model (AFM).

## 3. Title

Analysis of Hydrologic Properties Data

## 4. DI (including Rev. No. and Change No., if applicable):

MDL-NBS-HS-000014 REV00

## 5. Total Attachments

3

## 6. Attachment Numbers - No. of Pages in Each

I-2, II-1, III-21

	Printed Name	Signature	Date
7. Originator	H.H. Liu	SIGNATURE ON FILE	4-3-03
8. CSO	M. Zhu	SIGNATURE ON FILE	4/3/2003
9. Checker	P. Persoff	SIGNATURE ON FILE	4/3/2003
10. QER	K. Gilkerson	SIGNATURE ON FILE	4/3/2003
11. Responsible Manager/Lead	Y-S. Wu	SIGNATURE ON FILE	4/3/2003
12. Responsible Manager	J.S.Y. Wang	SIGNATURE ON FILE	4/3/2003

## 13. Remarks

Block 7. C.F. Ahlers, S. Mukhopadhyay, R.F. Hedegaard, and J.E. Houseworth contributed to Section 6. G. Zhang and Y-S. Wu contributed to Section 7.

## Initial Issue

TER log number addressed in this Model Report

TER-02-0081

**OFFICE OF CIVILIAN RADIOACTIVE WASTE MANAGEMENT**  
**MODEL REVISION RECORD**

1. Page: 2 of 102

2. Model Title:  
Analysis of Hydrologic Properties Data

3. DI (including Rev. No. and Change No., if applicable):

MDL-NBS-HS-000014 REV00

4. Revision/Change No.	5. Description of Revision/Change
REV00	<p>Initial Issue</p> <p>This report is a revision of an Analysis/Model Report by the same title--Document Identifier ANL-NBS-HS-000002 (BSC 2001 [159725]). This previous scientific analysis did not document activities to validate the AFM.</p> <p>In this new model report, the entire documentation was revised. Side bars are not used because the changes were too extensive to use Step 5.9d)1).</p>

## TABLE OF CONTENTS

ACRONYMS .....	9
1. PURPOSE .....	11
2. QUALITY ASSURANCE .....	13
3. USE OF SOFTWARE .....	15
4. INPUTS .....	17
4.1 DATA AND PARAMETERS .....	17
4.1.1 Data .....	17
4.1.2 Parameters and Parameter Uncertainties .....	21
4.2 CRITERIA .....	21
4.3 CODES AND STANDARDS .....	23
5. ASSUMPTIONS .....	25
6. MODEL DISCUSSION .....	27
6.1 FRACTURE PROPERTIES .....	30
6.1.1 Fracture Permeability .....	30
6.1.2 Fracture Frequency, Intensity, Fracture Interface Area, Aperture, and van Genuchten Parameters .....	37
6.1.3 Fracture Porosity .....	40
6.2 MATRIX PROPERTIES .....	47
6.2.1 Matrix Permeability .....	49
6.2.2 Porosity .....	51
6.2.3 Matrix van Genuchten Parameters .....	51
6.2.4 Matrix Relative Permeability .....	52
6.3 THERMAL PROPERTIES .....	54
6.4 FAULT PROPERTIES .....	57
6.5 CONFIRMATION OF FRACTURE PROPERTIES .....	59
6.5.1 ESF Seepage Tests .....	59
6.5.2 Approach .....	60
6.5.3 Results and Discussion .....	62
6.6 ACTIVE FRACTURE MODEL (AFM) .....	64
6.6.1 Active Fracture Concept .....	64
6.6.2 Constitutive Relationships .....	65
6.7 AFM AND A FRACTAL-BASED FLOW MODEL .....	68
6.7.1 Evidence of Fractal Flow- Patterns in Unsaturated or Multiphase Flow Systems .....	68
6.7.2 Fractal Dimension .....	69
6.7.3 Consistency of the AFM and a Fractal Flow Pattern .....	71
6.8 COMPARISON WITH A FILM-FLOW MODEL .....	74
6.8.1 Film Flow Model .....	74
6.8.2 Model Comparison .....	79

**TABLE OF CONTENTS**

6.9	UNCERTAINTY, ALTERNATIVE MODELS (APPROACHES) AND OTHER ISSUES .....	80
7.	VALIDATION .....	81
7.1	MODEL VALIDATION ACTIVITIES .....	81
7.2	VALIDATION OF THE ACTIVE FRACTURE MODEL WITH CARBON-14 AND MINERAL COATING DATA .....	81
7.2.1	Model validation with Carbon-14 Data.....	82
7.2.2	Model Validation with Mineral Coating Data.....	85
8.	CONCLUSIONS .....	87
9.	INPUTS AND REFERENCES .....	89
9.1	CITED DOCUMENTS.....	89
9.2	CODES, STANDARDS, REGULATIONS, AND PROCEDURES.....	95
9.3	SOURCE DATA, LISTED BY DATA TRACKING NUMBER .....	95
9.4	OUTPUT DATA, LISTED BY DATA TRACKING NUMBER .....	99
10.	ATTACHMENTS .....	101
	ATTACHMENT I—DATA POINT VALUES IN FIGURES 10 AND 11.....	I-1
	ATTACHMENT II—DATA POINT VALUES IN FIGURE 7.....	II-1
	ATTACHMENT III - DESCRIPTION OF EXCEL FILES.....	III-1

## LIST OF FIGURES

1.	Schematic Showing Locations of Selected Boreholes.....	32
2.	Fracture Permeabilities for Topopah Spring Middle Nonlithophysal Unit. ....	36
3.	A Conceptual Model for Estimating Fracture Porosity Using Gas Tracer Testing Data.....	43
4.	Graph of Fitting of Equation 48 to Equation 50 using a Number of Data Points for $p^* < 5$ .....	63
5.	Capillary Pressure Curves of Fracture Continuum for $\gamma = 0, 0.5, \text{ and } 0.9$ .....	66
6.	Relative Permeability Curves of Fracture Continuum for $\gamma = 0, 0.5, \text{ and } 0.9$ .....	67
7.	Relation between $N$ and $l$ (Attachment II). The data points correspond to observed values for the Tptpmn unit. ....	69
8.	Schematic Showing Demonstration of “Box” Counting Procedure for Several Box Sizes, With the Shaded Areas Containing Saturation and Active Flow.....	70
9.	Match of Equation 78b to Surface Transmissivity-Film Thickness Measurements .....	76
10.	Matches of Equation 78 to (a) Film Thickness and (b) Surface Transmissivity- Film Thickness.....	77
11.	Match of Equation 78b to Surface Transmissivity-Film Thickness Measurements .....	78
12.	Comparison Between Relative Permeability-Saturation Relations Calculated Using the AFM with $m = 0.633$ (Table 7) for Several $\gamma$ Values (Solid Lines) and Relations Calculated from the Film-Flow Model with $\lambda$ Values (Dashed Lines) .....	79
13.	Comparisons Between Simulated Water Travel Times (Ages) for Rock Matrix at Boreholes (a) USW UZ-1 and (b) USW SD-12, as well as the Corresponding Carbon-14 Ages for Several $\gamma$ Values.....	84
14.	Simulated Average Portion of Active Fracture for the Relevant Model Layers (tsw32 to tsw38) as a Function of Infiltration Rate and $\gamma$ .....	86

INTENTIONALLY LEFT BLANK

**LIST OF TABLES**

1.	Qualified Software Used in this Report.....	15
2.	Data Tracking Numbers for Input Data Used.....	18
3.	Project Requirements and YMRP Acceptance Criteria Applicable to this Model Report.....	22
4.	GFM2000 Lithostratigraphy, UZ Model Layer, and Hydrogeologic Unit Correlation.....	28
5.	Scientific Notebooks.....	29
6.	Uncalibrated Fracture Permeabilities for the UZ Model Layers.....	33
7.	Fracture Properties for UZ Model Layers.....	40
8.	Matrix Properties Developed from Core Data.....	49
9.	Matrix Thermal Properties for the UZ Model Layers.....	56
10.	Bulk Thermal Conductivities of Repository Model Layers.....	57
11.	Fault Thermal Properties.....	57
12.	Calculated Fault Fracture Properties.....	59
13.	Log Values of van Genuchten Fracture $\alpha$ Estimated from the ESF Seepage Tests (Niche 3650).....	63

INTENTIONALLY LEFT BLANK

**ACRONYMS**

AC	Acceptance Criterion
ACC	Accession Number
AFM	Active Fracture Model
AP	Administrative Procedure
BSC	Bechtel SAIC Company, LLC
CFu	Crater Flat Undifferentiated Hydrogeologic Unit
CHn	Calico Hills Nonwelded Hydrogeologic Unit
CRWMS	Civilian Radioactive Waste Management System
DIRS	Document Input Reference System
DLA	Diffusion Limited Aggregation
DLS	Detailed Line Survey
DOE	U.S. Department of Energy
DST	Drift Scale Test
DTN	Data Tracking Number
ECRB	Enhanced Characterization of Repository Block
ESF	Exploratory Studies Facility
FEPs	Features, Events, and Processes
FY	Fiscal Year
GFM	Geologic Framework Model
HGU	Hydrogeologic Unit
LA	License Application
LBNL	Lawrence Berkeley National Laboratory
M&O	Management and Operations Contractor
NSP	Nevada State Plane
OCRWM	Office of Civilian Radioactive Waste Management
PA	Performance Assessment
PTn	Paintbrush nonwelded hydrogeologic unit
QA	Quality Assurance
QARD	Quality Assurance Requirements and Description
QIP	Quality Implementing Procedure

**ACRONYMS (Continued)**

RH	Relative Humidity
SHT	Single Heater Test
STN	Software Tracking Number
TBV	to be verified
TCw	Tiva Canyon welded hydrogeologic unit
TDMS	Technical Data Management System
TPO	Technical Product Output
TSPA	Total System Performance Assessment
TSw	Topopah Spring welded hydrogeologic unit
TWP	Technical Work Plan
USGS	United States Geological Survey
UZ	Unsaturated Zone
WP	Work Package
YMP	Yucca Mountain Project
YMRP	Yucca Mountain Review Plan, Information Only

## 1. PURPOSE

This Model Report describes the methods used to determine hydrologic properties based on the available field data from the unsaturated zone (UZ) at Yucca Mountain, Nevada, and documents validation of the active fracture model (AFM). This work was planned in *Technical Work Plan (TWP) for: Performance Assessment Unsaturated Zone* (BSC 2002 [160819], Sections 1.10.2, 1.10.3, and 1.10.8). Fracture and matrix properties are developed by analyzing available survey data from the Exploratory Studies Facility (ESF), Cross Drift for Enhanced Characterization of Repository Block (ECRB), and/or boreholes; air injection testing data from surface boreholes and from boreholes in the ESF; and data from laboratory testing of core samples. The AFM is validated on the basis of experimental observations and theoretical developments. This report is a revision of an Analysis Model Report, under the same title, as a scientific analysis with Document Identifier number ANL-NBS-HS-000002 (BSC 2001 [159725]) that did not document activities to validate the AFM.

The principal purpose of this work is to provide representative uncalibrated estimates of fracture and matrix properties for use in the model report *Calibrated Properties Model* (BSC 2003 [160240]). The present work also provides fracture geometry properties for generating dual-permeability grids as documented in the Scientific Analysis Report, *Development of Numerical Grids for UZ Flow and Transport Modeling* (BSC 2003 [160109]). The resulting calibrated property sets and numerical grids from these reports will be used in the Unsaturated Zone Flow and Transport Process Model (UZ Model), and Total System Performance Assessment (TSPA) models.

The fracture and matrix properties developed in this Model Report include:

- Fracture properties (frequency, permeability, van Genuchten  $\alpha$  and  $m$  parameters, aperture, porosity, and interface area) for each UZ Model layer
- Matrix properties (porosity, permeability, and van Genuchten  $\alpha$  and  $m$  parameters) for each UZ Model layer
- Thermal properties (grain density, wet and dry thermal conductivity, and grain specific heat) for each UZ Model layer
- Fault properties for each major hydrogeologic unit.

These properties incorporate the available measurement data, as applicable, to estimate fracture and matrix properties. Field data from liquid release testing in the ESF and other relevant data are also used to validate these properties and provide bounds on property values.

Another objective of this report is to document activities to validate the AFM based on experimental observations and theoretical developments. The AFM is a conceptual model that describes the fracture-matrix interaction in the UZ of Yucca Mountain. It is intended to be used to represent the hydrologic characteristics of rock fractures for the UZ Flow Model, UZ Radionuclide Transport Model under ambient conditions, Mountain-Scale and Drift-Scale Thermal-Hydrological-Chemical Models, and Multiscale Thermohydrology Model. These

validation activities are documented in Section 7 of this report regarding use of independent lines of evidence to provide additional confidence in the use of the AFM in the UZ models.

This model report was planned in the TWP (BSC 2002 [160819], Section 1.10) and there are some deviations from the TWP in this report. Data from the large-infiltration-plot test at Alcove 8 / Niche 3 and data from the large-block test have not been used for model validation because they were not available in time for this report. An interpretation of the AFM based on fractal flow patterns is discussed in Section 6.7, in addition to the alternative model (film-flow model in Section 6.8) that was planned in the TWP (BSC 2002 [160819], Section 2.7). Software infil2grid V1.7 (LBNL 2002 [154793]) was used, not V1.6 (LBNL 1999 [134754]) as planned in the TWP (BSC 2002 [160819], Table II-2). This is because infil2grid V1.7 (LBNL 2002 [154793]) can handle eight-character grid element names, while infil2grid V1.6 (LBNL 1999 [134754]) cannot. Uncertainties associated with calibration measurement and test equipment (BSC 2002 [160819], Table 2-5) are not discussed in this report because they are already reflected in the measurements and expected to be insignificant compared with uncertainties associated with data limitation and spatial variability.

A list of relevant features, events, and processes (FEPs) is presented in Section 6. Constraints and limitations are as follows: the fracture permeability, van Genuchten fracture  $\alpha$  and  $m$ , matrix permeability, and van Genuchten matrix  $\alpha$  and  $m$  reported here are uncalibrated and serve only as initial estimates in the Calibrated Properties Model. The calibrated properties, as well as the other properties, are intended for use in the mountain-scale and drift-scale UZ Models. Data availability is associated with parameter uncertainty that is represented in the uncertainty estimates given in this report. The use of the AFM is limited to conditions under which the continuum approach and the relevant hypotheses of the AFM are valid (CRWMS M&O 2000 [141187], Section 6.4; Section 6.6 of this report).

## 2. QUALITY ASSURANCE

Development of this model report and the supporting modeling activities have been determined to be subject to the Yucca Mountain Project's quality assurance (QA) program (BSC 2002 [160819], Section 8.2, Work Package (WP) AUZM06). Approved QA procedures identified in the TWP (BSC 2002 [160819], Section 4) have been used to conduct and document the activities described in this model report. The TWP also identifies the methods used to control the electronic management of data (BSC 2002 [160819], Section 8.4, WP AUZM06) during the modeling and documentation activities.

This model report provides uncalibrated values for hydrologic properties of natural barriers identified in AP-2.22Q, *Classification Criteria and Maintenance of the Monitored Geologic Repository Q-List* as "Quality Level – 1" items important to waste isolation. The report contributes to the analyses and modeling data used to support performance assessment (PA). The conclusions of this model report do not affect the proposed repository design or permanent items as discussed in AP-2.22Q.

INTENTIONALLY LEFT BLANK

### 3. USE OF SOFTWARE

The software programs used in this study are listed in Table 1. These are appropriate for the intended application and were used only within the range of validation. They were obtained from Software Configuration Management, and qualified under AP-SI.1Q, *Software Management*.

Table 1. Qualified Software Used in this Report

Software Name	Version	Software Tracking Number (STN)	DIRS Reference Number
TOUGH2	1.4	10007-1.4-01	146496
T2R3D	1.4	10006-1.4-00	146654
infil2grid	1.7	10077-1.7-00	154793

Standard Excel spreadsheets and visual display graphics programs (Excel 97 SR-1 and Tecplot V7.0) were also used but are not subject to software quality assurance requirements. All information needed to reproduce the work using these standard software programs is included in this report, with references specified (See Attachment III). Names of files based on these programs are given in Sections 6 and 7. (Excel files involving computations are specified in Sections 6.1 and 6.2.) A detailed description of these files are presented in Attachment III.

INTENTIONALLY LEFT BLANK

## 4. INPUTS

Fracture properties are developed based on available fracture survey data from the ESF, ECRB Cross Drift, and boreholes and air-injection testing data from vertical boreholes and ESF alcoves. Matrix properties are determined by combining core and small-scale matrix property data. Properties are determined by computing means, standard deviations, and standard errors for each UZ Model layer (BSC 2003 [160109]) for each property. Fracture porosities are determined based on the analyses of gas tracer data from the ESF. When no data for a specific layer are available, analogs are identified and used to assign properties. Field-testing data from the ESF are used to confirm the magnitude of parameters by establishing appropriate bounds for values. Fracture mineral coating data collected from ESF and carbon-14 data from vertical boreholes are used for validating the AFM. The data used in this report are appropriate for this study because they represent fracture and matrix properties available from the UZ at Yucca Mountain. The appropriateness of the data is also discussed in Sections 6 and 7 when they are used for developing UZ properties or validating the AFM.

### 4.1 DATA AND PARAMETERS

#### 4.1.1 Data

The input data used in property-set development include the following:

- Fracture properties developed from detailed line survey (DLS) fracture data (collected from the ESF North and South Ramps, Main Drift, and ECRB Cross Drift and which provide spatially varying frequency, length, and fracture dips and strikes) and fracture frequency data from boreholes (DTN: LB990501233129.001 [106787]).
- Air-injection testing data (from vertical boreholes) that are used for fracture permeability estimates (DTNs: GS960908312232.013 [105574] through LB980120123142.005 [114134] in Table 2).
- Air-injection and/or gas tracer data from the Upper Tiva Canyon, Bow Ridge fault, and Upper Paintbrush Contact Alcoves, the Single Heater Test (SHT) area, and the Drift Scale Test (DST) area that provide fracture permeability and porosity estimates (DTNs: LB990901233124.004 [123273], LB980912332245.002 [105593] and GS990883122410.002 [135230]).
- Data from liquid release test in the ESF niches that provide fracture van Genuchten  $\alpha$  and porosity estimates (DTNs: LB980901233124.003 [105592] and LB0110LIQR0015.001 [156907]).
- Measured properties from core samples (including effective porosity, bulk density, porosity, particle density, volumetric water content, saturation, water potential, hydraulic conductivity, matrix van Genuchten  $\alpha$  and  $m$  values, and residual saturation) and stratigraphic descriptions for samples from boreholes that are used for developing matrix properties for UZ model layers (DTNs: MO0109HYMXPROP.001 [155989] through GS940208314211.008 [145581] in Table 2).

- Thermal properties by lithostratigraphic unit, developed from small-scale measurements. Development of these properties is documented in a separate model report describing thermal conductivity of the potential repository horizon (BSC 2002 [160319]) (DTNs: SN0206T0503102.005 [160258] and SN0208T0503102.007 [160257]).
- Numerical grids and calibrated properties that are used for validating the AFM (Table 2). Development of these data are documented in a separate scientific analysis report (BSC 2003 [160109]) and a model report describing the Calibrated Properties Model, respectively (BSC 2003 [160240]).

Specific input data sets and the associated Data Tracking Numbers (DTNs) are provided in Table 2. Geology information from ESF (CRWMS M&O 1998 [102679], Table 2) is also used for estimating matrix properties (Attachment III). This report does not discuss Principal Factors as defined in Attachment I of AP-3.15Q, *Managing Technical Product Inputs*.

Table 2. Data Tracking Numbers for Input Data Used

Data Description	DTN	Data Use*
Matrix saturation, water potential, and hydrologic property data	MO0109HYMXP.001 [155989]	6.1.3.3 Att. III
Physical properties and water potential for borehole samples from USW WT-24	GS980708312242.010 [106752]	Att. III
Physical properties and water potential for borehole samples from USW SD-6	GS980808312242.014 [106748]	Att. III
Physical properties and hydraulic-conductivity measurements from USW WT-24	GS980708312242.011 [107150]**	Att. III
Physical properties and saturated-hydraulic-conductivity measurements from USW SD-6	GS980908312242.038 [107154]**	Att. III
Physical properties and saturated-hydraulic-conductivity measurements from boreholes USW SD-7, USW SD-9, USW SD-12, USW UZ-14 and UE-25 UZ#16	GS980908312242.041 [107158]**	Att. III
Measured physical and hydraulic properties of core samples from Busted Butte boreholes	GS990308312242.007 [107185] GS990708312242.008 [109822]	Att. III
Physical properties and saturated hydraulic conductivity of cores from surface samples from the ESF main drift 29+00m to 57+00m	GS971008312231.006 [107184]**	Att. III
Water-retention data of borehole samples and surface samples from ESF north ramp	GS980908312242.037 [107180]**	Att. III

NOTE: \* Sections where the data used are described in detail.

\*\* These DTNs are not used for calculating Principal Factors.

Table 2. Data Tracking Numbers for Input Data Used (Continued)

Data Description	DTN	Data Use*
Unsaturated hydraulic properties of borehole samples from the PTn exposure in the ESF north ramp	GS980408312242.008 [107161]**	Att. III
Physical properties and saturated hydraulic conductivity measurements of core samples from boreholes in the ESF north ramp	GS980908312242.040 [107169]**	Att. III
Physical properties of borehole samples from the PTn exposure in the ESF north ramp	GS980308312242.005 [107165]**	Att. III
Unsaturated water-retention data for samples from USW SD-6	GS980908312242.039 [145272]	Att. III
Moisture-retention data for samples from boreholes USW SD-7, USW SD-9, USW SD-12 and UE-25 UZ#16	GS960808312231.003 [147590]	Att. III
Unsaturated hydraulic properties from USW WT-24	GS980808312242.012 [149375]**	Att. III
Moisture-retention data from boreholes USW UZ-N27 and UE-25 UZ#16.	GS950608312231.008 [144662]	Att. III
Unsaturated hydraulic conductivity and water potential in Busted Butte volcanic tuff cores	GS010608312242.001 [160822]	Att. III
Lithostratigraphic classification of core samples for the Busted Butte Phase 2 test block	LA0207SL831372.001 [160824]**	Att. III
Lithostratigraphic information and chemical analyses from drill cores collected in ESF	LAJF831222AQ98.014 [160825]**	Att. III
Stratigraphic description and data for the Yucca Mountain tuff in boreholes NRG#2B, NRG-7/7A, SD-9, UZ-14, UZ#16, UZ-N11, UZ-N33, UZ-N34, UZ-N53, UZ-N54, UZ-N55	GS950108314211.009 [152556]	Att. III
USW UZ-7a shift drilling summaries, lithologic logs, structural logs, weight logs, and composite borehole log from 0.0' to 770.0'	TM000000UZ7ARS.001 [160826]**	Att. III
Table of contacts in borehole USW UZ-N35	GS940208314211.007 [155533]	Att. III
Table of contacts for the Tiva Canyon tuff in borehole USW UZ-N36	GS940308314211.018 [145589]	Att. III
Lithostratigraphic data for Paintbrush Group bedded tuff units in boreholes USW UZ-N11, USW UZ-14, USW NRG-7/7A, USW SD-9, USW UZ-N37, USW NRG-6, UE-25 NRG#2B, USW UZ-N31, USW UZ-N32, USW SD-12, UE-25 UZ#16, USW UZ-N54, USW UZ-N53	GS950108314211.008 [152558]	Att. III
Stratigraphic descriptions of the Pah Canyon tuff in boreholes UE-25 NRG#2B, UE-25 NRG#4, USW NRG-6, USW NRG-7/7A, USW SD-9, USW SD-12, USW UZ-14, USW UZ-N31, USW UZ-N32, and USW UZ-N37	GS950708314211.028 [160827]	Att. III
Tables of contacts in boreholes USW UZ-N57, UZ-N58, UZ-N59, and UZ-N61	GS940208314211.008 [145581]	Att. III

NOTE: \* Sections where the data used are described in detail.

\*\* These DTNs are not used for calculating Principal Factors.

Table 2. Data Tracking Numbers for Input Data Used (Continued)

<b>Data Description</b>	<b>DTN</b>	<b>Data Use*</b>
Developed fracture hydrologic properties for UZ model layers (FY99)	LB990501233129.001 [106787]	6.1.2 6.1.3.1 6.1.3.3
Air permeability data from vertical boreholes	GS960908312232.013 [105574]**	Section 6.1.1 Figure 2 Table 6 Att. III
Air permeability data from Alcoves 1,2,3	GS970183122410.001 [105580]**	Table 6 Att. III
Air-injection and permeability data-SHT area	LB960500834244.001 [105587]**	Figure 2 Table 6 Att. III
Air-injection and permeability data-DST area	LB970600123142.001 [105589]** LB980120123142.004 [105590]** LB980120123142.005 [114134]**	Figure 2 Table 6 Att. III
Pre-excavation air-permeability data from Niches 3566, 3650 3107, and 4788	LB990901233124.004 [123273]	Figure 2
Air-injection, tracer test, and fracture porosity data	LB980912332245.002 [105593]	6.1.3.1 6.1.3.2 6.1.3.3
Ghost Dance fault permeability	GS990883122410.002 [135230]**	6.4
ESF seepage test data	LB980901233124.003 [105592]**	6.5.1, 6.5.2 6.5.3 6.1.3.4
ESF seepage test data	LB0110LIQR0015.001 [156907]	6.5.3 6.1.3.4
Geologic Framework Model (GFM2000)	MO0012MWDGFM02.002 [153777]	6.4 Att. III
1-D site-scale calibrated properties: supporting files	LB02091DSSCP3I.001 [161292]	7.2.1
Calibrated hydrologic properties for UZ model	LB02091DSSCP3I.002 [161433]	7.2.1
Supporting files of calibrated hydrologic properties for UZ model	LB0208UZDSCPMI.001 [161285]	7.2.2
Yucca Mountain Project borehole locations	MO9906GPS98410.000 [109059]	7.2.1
Diffusion of sorbing and non-sorbing radionuclides	LA000000000034.002 [148603]	7.2.1

NOTE: \* Sections where the data used are described in detail.

\*\* These DTNs are not used for calculating Principal Factors.

Table 2. Data Tracking Numbers for Input Data Used (Continued)

Data Name	DTN	Data Use*
Infiltration maps	GS000308311221.005 [147613]	7.2.2
3D UZ numerical grid	LB03023DKMGRID.001 [162354]	7.2.2
Thermal properties of nonrepository geologic layers	SN0206T0503102.005 [160258]	6.3
Thermal conductivity of the potential repository horizons	SN0208T0503102.007 [160257]	6.3

NOTE: \* Sections where the data used are described in detail.

\*\* These DTNs are not used for calculating Principal Factors.

#### 4.1.2 Parameters and Parameter Uncertainties

This model report describes the development of hydrologic properties based on the available field data from the UZ at Yucca Mountain, Nevada, and documents activities to validate the AFM. The input parameters for validating the AFM include the calibrated hydrologic property set (porosity, permeability, and van Genuchten parameters) for the UZ model listed in Table 2 (DTN: LB02091DSSCP3I.002 [161433]). The development of the calibrated property sets is documented in the model report *Calibrated Properties Model* (BSC 2003 [160240]). (Note that uncalibrated properties (including DTN: LB990501233129.001 [106787]) are not used for the model validation activities described in Section 7 of this report.) Uncertainties of these calibrated properties are approximated, based on property measurements at small scales, and result from the development of hydrologic properties for UZ Model layers to be discussed in this report. (The determination of these uncertainties is presented in *Calibrated Properties Model* (BSC 2003 [160240]).) A key parameter in the AFM is the active fracture parameter  $\gamma$  (Liu et al. 1998 [105729]). Evaluation of its uncertainty, by comparing simulation results corresponding to different  $\gamma$  values with field observations, is part of the model validation activity to be discussed in Section 7 of this report.

#### 4.2 CRITERIA

The general requirements to be satisfied by TSPA are stated in 10 CFR 63.114 [156605] (Requirements for performance assessment). Technical requirements to be satisfied by TSPA are identified in the Yucca Mountain *Project Requirements Document* (Curry and Loros 2002 [157916]). The acceptance criteria that will be used by the Nuclear Regulatory Commission (NRC) to determine whether the technical requirements have been met are identified in *Yucca Mountain Review Plan, Information Only* (YMRP; NRC 2003 [162418]). The pertinent requirements and criteria for this model report are summarized in Table 3.

Table 3. Project Requirements and YMRP Acceptance Criteria Applicable to this Model Report

Requirement Number <sup>a</sup>	Title	10 CFR 63 Link	YMRP Acceptance Criteria
PRD-002/T-015	Requirements for Performance Assessment	10 CFR 63.114 (a–c, e–g)	Criteria 1 to 3 for <i>Flow Paths in the Unsaturated Zone</i> <sup>b</sup>
PRD-002/T-016	Requirements for Multiple Barriers	10 CFR 63.115 (a–c) 10 CFR 63.113 (a)	Criteria 1 to 3 for <i>Demonstration of Multiple Barriers</i> <sup>c</sup>

NOTE: <sup>a</sup> from Curry and Loros (2002 [157916])

<sup>b</sup> from NRC (2003 [162418], Section 2.2.1.3.6.3)

<sup>c</sup> from NRC (2003 [162418], Section 2.2.1.1.3)

The criteria identified in Section 2.2.1.1.3 *Acceptance Criteria*, (for Section 2.2.1.1 *System Description and Demonstration of Multiple Barriers*), which are based on meeting the requirements at 10 CFR 63.113(a) and 63.115(a)–(c) are:

- Acceptance Criterion 1, *Identification of Barriers is Adequate*:

The hydrogeologic units above and below the proposed repository are natural barriers important to waste isolation. Their capability is determined by their hydrologic properties.

- Acceptance Criterion 2, *Description of Barrier Capability to Isolate Waste is Acceptable*:

The capability of the identified barriers to prevent or substantially delay the movement of water or radioactive materials is adequately identified and described. The uncertainty associated with barrier capabilities is adequately described.

- Acceptance Criterion 3, *Technical Basis for Barrier Capability is Adequately Presented*:

The technical bases are consistent with the technical basis for the performance assessment. The technical basis for assertions of barrier capability is commensurate with the importance of each barrier's capability and the associated uncertainties.

The criteria identified in Section 2.2.1.3.6.3 *Acceptance Criteria* (for 2.2.1.3.6 *Flow Paths in the Unsaturated Zone*), which are based on meeting the requirements of 10 CFR 63.114(a)–(c) and (e)–(g), relating to flow paths in the saturated zone model abstraction, are:

- Acceptance Criterion 1, *System Description and Model Integration are Adequate*:

The process-level model flow for paths in the unsaturated zone adequately incorporates important physical phenomena, and uses consistent and appropriate assumptions throughout.

The aspects of geology, hydrology, and physical phenomena that may affect flow paths in the unsaturated zone are adequately considered. Conditions and assumptions in the

process-level model of flow paths in the unsaturated zone are readily identified and consistent with the body of data presented in the description.

The process-level model of flow paths in the unsaturated zone uses assumptions, technical bases, and data that are appropriate and consistent with other process-level models. The descriptions and technical bases are transparent and traceable to site and design data.

Adequate spatial variability of model parameters and boundary conditions are employed in process-level models to estimate flow paths in the unsaturated zone.

Average parameter estimates used in the process-level model of flow paths in the unsaturated zone are representative of the temporal and spatial discretizations considered in the model.

- Acceptance Criterion 2, *Data Are Sufficient for Model Justification:*

Hydrological values used in the safety case are adequately justified. Adequate descriptions of how data were used, interpreted, and appropriately synthesized into the parameters are provided.

Sensitivity or uncertainty analyses are performed to assess data sufficiency, and determine the possible need for additional data.

Accepted and well-documented procedures are used to construct numerical models.

Reasonably complete process-level conceptual and mathematical models are used in the analyses. In particular: (i) mathematical models are provided that are consistent with conceptual models and site characteristics; and (ii) the robustness is demonstrated by comparison of results from different mathematical models.

- Acceptance Criterion 3, *Data Uncertainty Is Characterized and Propagated Through the Model Abstraction:*

Models use parameter values, assumed ranges, probability distributions, and/or bounding assumptions that are technically defensible, and reasonably account for uncertainties and variabilities.

The technical bases for the parameter values used are provided.

The initial conditions, boundary conditions, and computational domain used in sensitivity analyses and/or similar analyses are consistent with available data. Parameter values are consistent with the initial and boundary conditions and the assumptions of the conceptual models for the Yucca Mountain site.

Uncertainties in the characteristics of the natural system are considered.

### 4.3 CODES AND STANDARDS

No specific formally established standards have been identified as applying to this analysis and modeling activity.

INTENTIONALLY LEFT BLANK

## 5. ASSUMPTIONS

This section documents the only assumption made to determine hydrologic properties and validate the AFM, based on data available from the UZ of Yucca Mountain. This assumption is as follows:

1. Since a systematic approach for upscaling properties directly from small-scale measurements is still lacking for unsaturated fractured rock, simple averaging schemes are assumed to be appropriate in most cases for the upscaling purpose in the analyses to be reported in this study. The relation of Paleologos et al. (1996 [105736], p. 1336), originally developed for porous media, is assumed to be appropriate for upscaling matrix permeability when an upper limit of 1.5 orders of magnitude is used for the amount of upscaling. Hydrologic property data have been determined on scales that are generally much smaller than the scales characterizing the subsurface heterogeneity (e.g., characteristic sizes for model layers). While considerable progress has been made in developing upscaling schemes for porous media, the scale-dependent behavior of a hydrologic property for fractured rocks can be very different from that for porous media. For example, the existence of fractures in a fractured rock, which may act as a capillary barrier, can increase tortuosity of liquid water in the matrix, and therefore reduce large-scale matrix permeability compared with the case without fractures. It is necessary to make this assumption to determine rock properties using small-scale measurements. Note that the rock properties developed herein are mainly used as initial estimates for use in the inversion process documented in a separate Model Report describing the Calibrated Properties Model (BSC 2003 [160240]). The upscaling issue is further considered in the inversion process, which provides large-scale properties by matching the large-scale simulation results with grid block-scale observations averaged from small-scale data. Based on the above reasoning, no confirmation is needed for this assumption. This assumption is used in Sections 6.1 and 6.2.

INTENTIONALLY LEFT BLANK

## 6. MODEL DISCUSSION

In this section, the methodologies and data used to determine representative estimates of the fracture and matrix properties for the UZ Model layers are discussed. The concept and mathematical formulations of the AFM are also presented. Table 4 shows the relationships between the lithostratigraphy of the *Geologic Framework Model (GFM2000)* (BSC 2002 [159124]) and the UZ Model layers, as documented in a Scientific Analysis Report describing development of numerical grids for UZ flow and transport modeling (BSC 2003 [160109], Table 11). (Note that the relationship between major units and hydrogeologic units in Table 4 is slightly different from Table 1 of Flint (1998 [100033]). Most of these estimates of fracture and matrix properties are used as inputs in the inversion modeling studies documented in the Model Report *Calibrated Properties Model* (BSC 2003 [160240]). The key scientific notebooks (with relevant page numbers) used for this study are listed in Table 5. One assumption is used in this section, as presented in Section 5. The intended use of the output data, developed using approaches in this section, is given in Section 1.

In this report, the subsurface heterogeneity of the Yucca Mountain UZ is represented by a number of model layers, each of which is considered to have uniform hydrologic properties. This is based on the following considerations: First, the overall behavior of flow and transport processes in the Yucca Mountain UZ is mainly determined by relatively large-scale heterogeneities introduced by stratification of the tuffs. Second, the complexity of models for heterogeneity needs to be consistent with data availability. Third, this layered approach is supported by field observations, such as matrix water saturation distributions. For a given geologic unit, measured matrix saturation distributions can be very similar in different boreholes (Flint 1998 [100033], pp. 24–30, Figures 5–9), indicating that matrix flow behavior and effective hydraulic properties should be similar within the unit. Further discussion of this issue is provided in a separate Model Report describing conceptual and numerical models for UZ flow and transport (CRWMS M&O 2000 [141187], Section 6.4.3).

It should be noted that van Genuchten (1980 [100610]) relationships, originally developed for porous media, are used as constitutive relations for the active fracture continuum defined in the AFM (Section 6.6 of this report). Not all connected fractures are active in conducting liquid water in the UZ of Yucca Mountain (Liu et al. 1998 [105729], pp. 2638–2641). The active fracture continuum consists of fractures that actively conduct liquid water. The use of van Genuchten relationships is based on a conceptual model that describes flow in fractures using porous medium equivalence. A further discussion of this conceptual model is provided in a separate Model Report, *Conceptual and Numerical Models for UZ Flow and Transport* (CRWMS M&O 2000 [141187], Section 6.4.4). Recently, Liu and Bodvarsson (2001 [160110]) developed a new constitutive-relationship model for unsaturated flow in fracture networks, based mainly on numerical experiments. They found that the van Genuchten model is consistent with the new model for low fracture saturations corresponding to the ambient conditions.

Table 4. GFM2000 Lithostratigraphy, UZ Model Layer, and Hydrogeologic Unit Correlation

<b>Major Unit (Modified from Montazer and Wilson 1984 [100161])</b>	<b>GFM2000 Lithostratigraphic Nomenclature</b>	<b>UZ Model Layer (BSC 2003 [160109], Table 11)</b>	<b>Hydrogeologic Unit (Flint 1998 [100033], Table 1)</b>
Tiva Canyon welded (TCw)	Tpcr	tsw11	CCR, CUC
	Tpcp	tsw12	CUL, CW
	TpcLD		
	Tpcpv3	tsw13	CMW
	Tpcpv2		
Paintbrush nonwelded (PTn)	Tpcpv1	ptn21	CNW
	Tpbt4	ptn22	BT4
	Tpy (Yucca)	ptn23	TPY
		ptn24	BT3
	Tpbt3	ptn25	TPP
	Tpp (Pah)		
	Tpbt2		
	Tptrv3		
	Tptrv2	ptn26	BT2
Topopah Spring welded (TSw)	Tptrv1	tsw31	TC
	Tptrn	tsw32	TR
		tsw33	TUL
	Tptrl, Tptf	tsw34	TMN
	Tptpul, RHHtop		
	Tptpmn	tsw35	TLL
	Tptpll	tsw36	TM2 (upper 2/3 of Tptpln)
	Tptpln		TM1 (lower 1/3 of Tptpln)
	Tptpv3	tsw38	PV3
	Tptpv2	tsw39 (vit, zeo)	PV2

Source: BSC (2003 [160109], Table 11)

Table 4. GFM2000 Lithostratigraphy, UZ Model Layer, and Hydrogeologic Unit Correlation (continued)

<b>Major Unit (Modified from Montazer and Wilson 1984 [100161])</b>	<b>GFM2000 Lithostratigraphic Nomenclature</b>	<b>UZ Model Layer (BSC 2003 [160109], Table 11)</b>	<b>Hydrogeologic Unit (Flint 1998 [100033], Table 1)</b>
Calico Hills nonwelded (CHn)	Tptpv1	ch1 (vit, zeo)	BT1 or BT1a (altered)
	Tpbt1		
	Tac (Calico)	ch2 (vit, zeo)	CHV (vitric) or CHZ (zeolitic)
		ch3 (vit, zeo)	
		ch4 (vit, zeo)	
		ch5 (vit, zeo)	
	Tacbt (Calicobt)	ch6 (vit, zeo)	BT
	Tcpuv (Prowuv)	pp4	PP4 (zeolitic)
	Tcpuc (Prowuc)	pp3	PP3 (devitrified)
	Tcpmd (Prowmd)	pp2	PP2 (devitrified)
	Tcplc (Prowlc)		
	Tcplv (Prowlv)	pp1	PP1 (zeolitic)
	Tcpbt (Prowbt)		
Tcbuv (Bullfroguv)			
Tcbuc (Bullfroguc)	bf3		
Tcbmd (Bullfrogmd)			
Tcblc (Bullfroglc)			
Tcblv (Bullfroglv)	bf2	BF2 (nonwelded)	
Tcbbt (Bullfrogbt)			
Tctuv (Tramuv)			
Tctuc (Tramuc)	tr3	Not Available	
Tctmd (Trammd)			
Tctlc (Tramlc)			
Tctlv (Tramlv)	tr2	Not Available	
Tctbt (Trambt) and below			

Source: BSC (2003 [160109], Table 11)

Table 5. Scientific Notebooks

<b>LBNL Scientific Notebook ID</b>	<b>M&amp;O Scientific Notebook ID</b>	<b>Relevant Pages</b>	<b>Citation</b>
YMP-LBNL-GSB-1.1.2	SN-LBNL-SCI-003-V1	93–94, 117–127, 145-146	Ahlers 2000 [155853]
YMP-LBNL-YWT-SM-3	SN-LBNL-SCI-100-V3	69–79	Wang 2003 [161654]
YMP-LBNL-GSB-LHH-3	SN-LBNL-SCI-215-V1	35–53, 101	Wang 2003 [161654]
YMP-LBNL-UZ-CFA-1	SN-LBNL-SCI-003-V2	57–83	Wang 2003 [161654]
YMP-LBNL-HHL-GZ-1	SN-LBNL-SCI-227-V1	8–19, 21–54, 70– 71, 73-84, 87	Wang 2003 [161654]
YMP-LBNL-YSW-3	SN-LBNL-SCI-199-V1	92-99	Wang 2003 [161654]
YMP-LBNL-GSB-LHH-2	SN-LBNL-SCI-098-V1	64–68	Liu 2001 [155675]

This report also addresses the following FEPs that were taken from the License Application (LA) FEP List (DTN: MO0301SEPFEPS1.000 [161496]). The LA FEP List is a revision to the previous project FEP list (Freeze et al. 2001 [154365]), which was used to develop the list of included FEPs in the TWP (BSC 2002 [160819], Table 2-6). The selected FEPs are those taken from the LA FEP List that are associated with the subject matter of this report, regardless of the anticipated status for exclusion or inclusion in TSPA-LA as represented in BSC (2002 [160819]). The results of this model are part of the basis for the treatment of FEPs as discussed in the *Total System Performance Assessment-License Application Methods and Approach* (BSC 2002 [160146], Section 3.2.2). The cross-reference for each FEP to the relevant sections of this report is also given below.

- YMP FEP Database Number 2.2.07.08.0A: Fracture Flow in the UZ. (This FEP is addressed in Sections 6.6-6.8 of this report.)
- YMP FEP Database Number 1.2.02.01.0A: Fractures. (This FEP is addressed in Sections 6.1 and 6.6 of this report.)
- YMP FEP Database Number 2.2.03.01.0A: Stratigraphy. (This FEP is addressed in Sections 6.1- 6.4 of this report.)
- YMP FEP Database Number 2.2.07.02.0A: Unsaturated Groundwater Flow in Geosphere. (This FEP is addressed in Section 6.6 of this report.)
- YMP FEP Database Number 2.2.07.04.0A: Focusing of unsaturated flow (fingers, weeps). (This FEP is addressed in Sections 6.6 and 7 of this report.)
- YMP FEP Database Number 2.2.03.02.0A: Rock Properties of Host Rock and Other Units. (This FEP is addressed in Sections 6.1-6.5 of this report.)

The following subsections present the methods used to determine fracture properties, matrix properties, thermal properties, and fault properties, followed by an analysis confirming specific fracture properties utilizing field data. A description of the AFM is also presented in Section 6.6. The validation of the AFM is documented in Section 7.

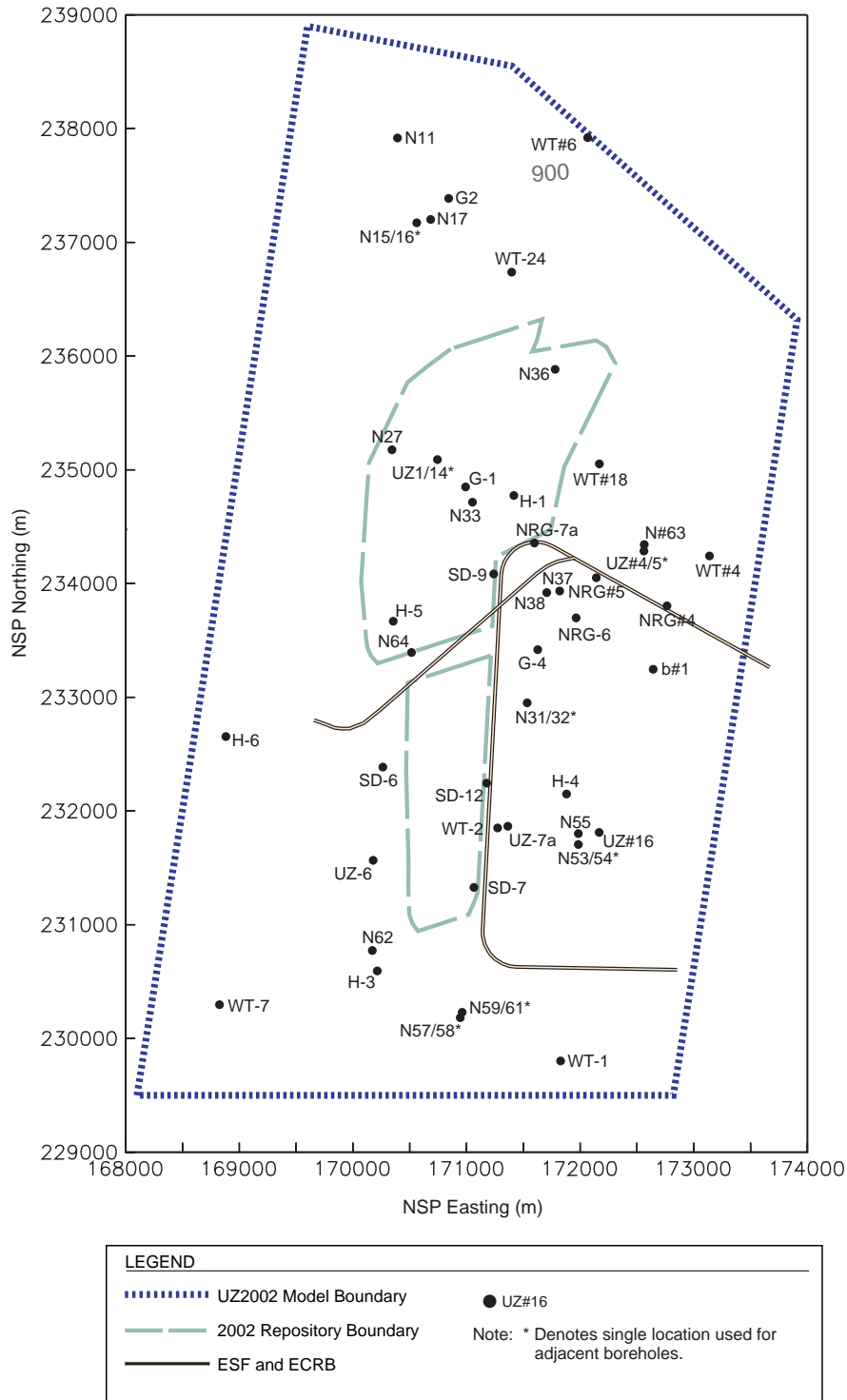
## **6.1 FRACTURE PROPERTIES**

Fracture properties determined in this report include fracture frequency, fracture aperture, fracture porosity, fracture interface area, uncalibrated van Genuchten fracture  $\alpha$  and  $m$ , and uncalibrated fracture permeability. The development of fracture properties is documented in a Scientific Notebook (Wang 2003 [161654], SN-LBNL-SCI-215-V1, pp. 35–53). Excel files used for calculating fracture properties are listed and described in Attachment III. Excel files lecan97.xls, UTCA\_BRFA.xls, drift.xls, and airk.xls are used for calculating fracture permeability values, and Fpor.xls is used for determining fracture porosity values.

### **6.1.1 Fracture Permeability**

The fracture permeabilities calculated here for the UZ Model layers are based on air permeabilities inferred from air-injection tests performed in vertical boreholes and in ESF

alcoves. Permeabilities inferred from air-injection tests in boreholes are representative of fracture absolute permeabilities. These permeabilities were determined based on pneumatic-pressure data and are calculated using a modified version of Hvorslev's (1951 [101868], p. 30, Case 8) solution for steady-state elliptic flow (LeCain 1995 [101700], p. 10). The determined permeability values are combined here to determine effective fracture permeabilities for the UZ Model layers. Geometric means of these fracture permeabilities are considered to reflect upscaling of these permeabilities for use as single values representative for each model layer. Note that permeability is an intrinsic property for a test medium and theoretically independent of test fluids, as long as the test medium can be viewed as a continuum. Thus, fracture permeabilities derived from air injection tests are considered to be applicable for describing liquid water flow in fractures.



Source: BSC (2003 [160240], Figure 1).

Figure 1. Schematic Showing Locations of Selected Boreholes.

For the Tiva Canyon welded hydrogeologic unit (TCw), fracture permeabilities were based on air-injection tests performed in boreholes NRG-7a, NRG-6, SD-12, and UZ#16 and in the Upper Tiva Canyon, Bow Ridge fault, and Upper Paintbrush Contact Alcoves (Alcoves 1, 2 and 3, respectively). For the Paintbrush nonwelded hydrogeologic unit (PTn), the permeability data are from borehole NRG-7a and in the Upper Paintbrush Contact Alcove (Alcove 3). For the Topopah Spring welded hydrogeologic unit (TSw), the permeability data are from boreholes NRG-7a, NRG-6, SD-12 and UZ#16 and from the Single Heater and Drift Scale Test areas in Alcove 5. For the Calico Hills nonwelded hydrogeologic unit (CHn), permeability data are available only from a single sampled interval in the borehole UZ#16. The locations of the boreholes are given in Figure 1. No air-injection data are available for the Prow Pass (pp), Bullfrog (bf), and Tram (tr) units. For model layers where no data are available, analogs to other units are used based on those designated for matrix properties (Flint 1998 [100033], p. 46), the degree of zeolitic alteration, and degree of welding. These fracture permeabilities are used as prior information and initial estimates for a separate model report describing the calibrated properties model.

Table 6 lists the geometric means of the fracture permeabilities for the UZ Model layers. The lithostratigraphic units were assigned to the UZ Model layers as listed in Table 4. The fracture permeabilities were treated as isotropic, and the data from vertical boreholes and from the horizontal and inclined boreholes in the ESF alcoves were combined. The scales of these measurements are similar, as discussed in Section 6.1.1.1.

Table 6. Uncalibrated Fracture Permeabilities for the UZ Model Layers

UZ Model Layer	Fracture Permeability (m <sup>2</sup> )				
	Basis <sup>a</sup>	k <sub>G</sub> <sup>b</sup>	log(k <sub>G</sub> )	σ <sub>log(k<sub>G</sub>)</sub> <sup>c</sup>	N <sup>d</sup>
tcw11	BRFA	3.0E-11	-10.52	-	2
tcw12	UTCA UPCA NRG-6 NRG-7a SD-12 UZ#16	5.3E-12	-11.28	0.78	80
tcw13	UPCA NRG-7a	4.5E-12	-11.35	1.15	3
ptn21	UPCA NRG-7a	3.2E-12	-11.49	0.88	12
ptn22	NRG-7a	3.0E-13	-12.52	0.20	4
ptn23	NRG-7a	3.0E-13	-12.52	0.20	4
ptn24	NRG-7a	3.0E-12	-11.52	-	1
ptn25	NRG-7a	1.7E-13	-12.78	0.10	7
ptn26	NRG-7a	2.2E-13	-12.66	-	1
tsw31	Average TSW	8.1E-13	-12.09	-	-
tsw32	NRG-6 NRG-7a SD-12 UZ#16	7.1E-13	-12.15	0.66	31

Table 6. Uncalibrated Fracture Permeabilities for the UZ Model Layers (continued)

UZ Model Layer	Fracture Permeability ( $m^2$ )				
	Basis <sup>a</sup>	$k_G$ <sup>b</sup>	$\log(k_G)$	$\sigma_{\log(k_G)}$ <sup>c</sup>	N <sup>d</sup>
tsw33	NRG-6 NRG-7a SD-12 UZ#16	7.8E-13	-12.11	0.61	27
tsw34	SHT DST NRG-6 NRG-7a SD-12 UZ#16	3.3E-13	-12.48	0.47	180
alternate tsw34	SHT DST NRG-6 NRG-7a SD-12 UZ#16	1.5E-13	-12.81	0.75	180
tsw35	NRG-7a UZ#16	9.1E-13	-12.04	0.54	31
tsw3[67]	SD-12 UZ#16	1.3E-12	-11.87	0.28	19
tsw38	Average TSw	8.1E-13	-12.09	-	-
tsw39	Average TSw	8.1E-13	-12.09	-	-
ch1Ze	ch2Ze	2.5E-14	-13.60	-	-
ch1VI	ptn26	2.2E-13	-12.66	-	-
ch[23456]VI	ptn26	2.2E-13	-12.66	-	-
ch[2345]Ze	UZ#16	2.5E-14	-13.60	-	1
ch6	ch2Ze	2.5E-14	-13.60	-	-
pp4	ch2Ze	2.5E-14	-13.60	-	-
pp3	ptn26	2.2E-13	-12.66	-	-
pp2	ptn26	2.2E-13	-12.66	-	-
pp1	ch2Ze	2.5E-14	-13.60	-	-
bf3	ptn26	2.2E-13	-12.66	-	-
bf2	ch2Ze	2.5E-14	-13.60	-	-
tr3	ptn26	2.2E-13	-12.66	-	-
tr2	ch2Ze	2.5E-14	-13.60	-	-

Output-DTN: LB0205REVUZPRP.001 [159525]

DTNs: GS960908312232.013 [105574]; GS970183122410.001 [105580];  
LB970600123142.001 [105589]; LB980120123142.004 [105590];  
LB980120123142.005 [114134]; LB960500834244.001 [105587]

NOTE: <sup>a</sup> Identifies the corresponding air-injection borehole(s) and/or alcove(s) or analog to another model layer(s). UTCA-Upper Tiva Canyon Alcove, BRFA- Bow Ridge fault Alcove, UPCA-Upper Paintbrush Contact Alcove, SHT- Single Heater Test Area, DST-Drift Scale Test Area, and NRG-6, NRG-7a, SD-12, and UZ#16 are vertical boreholes. (This column is presented for information only and is not from the cited DTN.)

<sup>b</sup> Geometric mean

<sup>c</sup> Standard deviation

<sup>d</sup> Number of sampled intervals

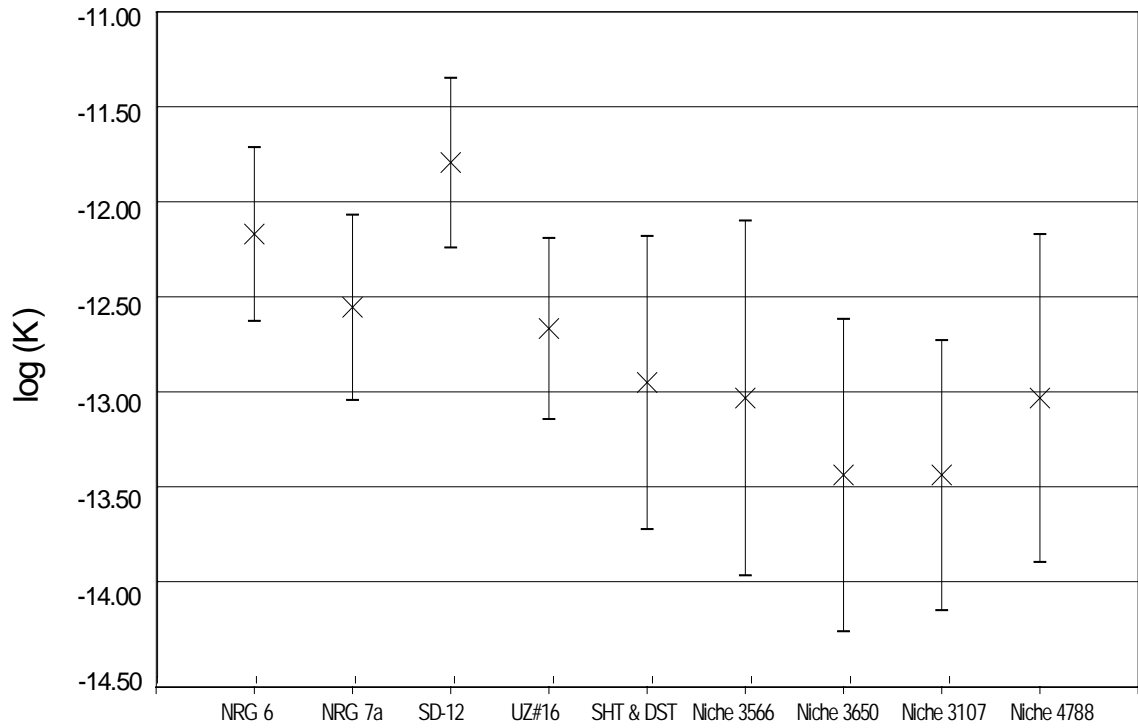
“-“ means that no data are available

The mean fracture permeabilities range from  $2.5 \times 10^{-14} \text{ m}^2$  to  $3.0 \times 10^{-11} \text{ m}^2$ . The Tiva Canyon welded unit (TCw) has the highest fracture permeabilities. Topopah Spring welded unit (TSw) fracture permeabilities are, in general, higher than those for the nonwelded Paintbrush (PTn) and Calico Hills (CHn) units. Two fracture permeabilities are shown for the Topopah Spring middle nonlithophysal unit (tsw34). These represent two different approaches for weighting the available air-injection data. For tsw34, there were 143 sampled intervals in the Alcove 5 heater test areas compared to 37 sampled intervals in the four vertical borehole injection tests. For the first case, the data from Alcove 5 were weighted with those from the vertical borehole tests ( $k = 0.8 k_{G, \text{vertical boreholes}} + 0.2 k_{G, \text{Alcove 5}}$ ). In the alternate tsw34 case, each sampled interval is weighted equally.

The uncertainty and variability of fracture permeabilities for the UZ Model layers are reflected by the standard deviations reported in Table 6. These standard deviations would result in 95% confidence intervals covering three orders of magnitude, even for the units that had a large number of sampled intervals. The data indicate that fracture permeabilities are highly variable.

#### 6.1.1.1 Scaling Issues

As noted previously, the permeabilities measured in the vertical boreholes and alcoves were combined to determine the fracture permeability for each UZ Model layer. The packer lengths were approximately 4 m for vertical boreholes, 1 to 3 m for Alcoves 1, 2, and 3, and 5 to 12 m in the SHT and DST areas (Alcove 5). These data were all considered to be on the same relative scale and representative of the fracture permeability on the scale of the UZ Model after upscaling, using geometric means. Additional air-permeability data on a scale of one-foot intervals are also available from air-injection testing in niches in the ESF in the Topopah Spring middle nonlithophysal unit (tsw34). The air-injection data from the niche studies are not used here for determining mean fracture permeabilities for the model layers, since these data are on a smaller scale and may not be representative of larger-scale effective permeability. Figure 2 compares the geometric means and range of data (mean  $\pm$  standard deviation) for the model layer tsw34 corresponding to Tptpmn (Table 4) (Wang 2003 [161654], SN-LBNL-SCI-215-V1, p. 101). The data shown for the niche studies are inferred from pre-excavation air-injection testing. The ranges of the data overlap, but the geometric means for the measurements from the niche studies are generally lower than the other values. This would be expected because the mean permeability decreases as the scale of the measurement decreases (Neuman 1994 [105731]).



DTNs: GS960908312232.013 [105574], LB960500834244.001 [105587], LB970600123142.001 [105589], LB980120123142.004 [105590], LB980120123142.005 [114134], LB990901233124.004 [123273]

NOTE: Permeabilities were inferred from air-injection data. X indicates geometric mean, and range is ± one standard deviation. Details of calculations are shown in Wang (2003 [161654], SN-LBNL-SCI-215-V1, p. 101) and in spreadsheet drift.xls, in Attachment III, p. 19.

Figure 2. Fracture Permeabilities for Topopah Spring Middle Nonlithophysal Unit.

### 6.1.2 Fracture Frequency, Intensity, Fracture Interface Area, Aperture, and van Genuchten Parameters

Fracture frequency, interface area, and the van Genuchten  $m$  are determined from qualified fracture property data (DTN: LB990501233129.001 [106787]) developed from field data. These include Detailed Line Survey (DLS) fracture data (collected from the ESF North and South Ramps, Main Drift, and ECRB Cross Drift, providing spatially varying frequency, length, and fracture dips and strikes) and fracture frequency data from boreholes. For completeness, mathematical equations used for developing these properties in DTN: LB990501233129.001 [106787] are also described here.

For calculating fracture frequencies using the DLS in the ESF and ECRB Cross Drift, the mean fracture frequency is given by the inverse of the mean spacing. The mean spacing is calculated by:

$$\bar{s} = \frac{1}{nf - 1} \sum_2^{nf} (D_i - D_{i-1}) \quad (\text{Eq. 1})$$

where  $D_i$  is the distance or station along the ESF where fracture  $i$  intersects the DLS and  $nf$  is the number of fractures. This is the *apparent* spacing. It is not the normal distance between the fracture planes and is therefore a rough estimate of the *true* spacing. These values were not corrected for any possible bias in orientation in the DLS. The mean fracture frequency is given by the inverse of the mean apparent spacing:

$$\bar{f} = \frac{1}{\bar{s}} \quad (\text{Eq. 2})$$

For calculating fracture frequency from borehole data, the data are processed to normalize for core recovery, corrected for bias in orientation, and scaled to represent larger length fracture. To correct for orientation bias for data from vertical boreholes, dip distributions are used as follows (modified from Lin et al. 1993 [116797], p. 24 [Eq. 3-1]):

$$f_{cb} = \frac{\sum_i f_{i,0-19^\circ \text{ dip}}}{\cos(10^\circ)} + \frac{\sum_i f_{i,20-39^\circ \text{ dip}}}{\cos(30^\circ)} + \frac{\sum_i f_{i,40-59^\circ \text{ dip}}}{\cos(50^\circ)} + \frac{\sum_i f_{i,60-90^\circ \text{ dip}}}{\cos(75^\circ)} \quad (\text{Eq. 3})$$

where  $f_{cb}$  is the fracture frequency corrected for orientation bias and  $f_i$  is the fracture frequency corresponding to the range of dip distribution. Finally, these values are corrected to represent larger length fractures on the scale of those characterized in the ESF. A simple correction ratio is used based on comparisons of ESF data with corresponding vertical boreholes for that model layer:

$$\bar{f} = f_{corrected} = f_{cb} R \quad (\text{Eq. 4})$$

$$R = \left( \frac{f_{ESF}}{f_{borehole}} \right)_{average}$$

Two correction factors  $R$  were calculated, one for welded units using data for the Topopah Springs middle nonlithophysal hydrogeologic unit (tsw34) and one for nonwelded units using data for the Pah Canyon Tuff in the Paintbrush hydrogeologic unit (ptn25). These units were selected because both ESF and borehole data are available; these were considered to be representative of the other units.

The fracture intensity is calculated by dividing the trace length of the fracture by the area surveyed. The area surveyed was 6 m (3 m above and below the traceline) times the length along the tunnel considered for that interval. The average fracture intensity  $I$  (m/m<sup>2</sup>) is given by:

$$I = \frac{\sum_{i=1}^{nf} t_i}{\text{area}} = \frac{\sum_{i=1}^{nf} t_i}{(6 \text{ m})(\text{interval length in meters})} \quad (\text{Eq. 5})$$

where  $t_i$  is trace length in meters for fracture  $i$ .

The fracture interface area is calculated by dividing the fracture area by the volume of the interval surveyed. The volume for the interval is estimated by multiplying the interval length surveyed by the square of the geometric mean of surveyed fracture trace length. The average fracture interface area per volume  $A_{fm}$  (m<sup>2</sup>/m<sup>3</sup>) is given by:

$$A_{fm} = \frac{\sum_{i=1}^{nf} \pi r_i^2}{\text{volume}} = \frac{\sum_{i=1}^{nf} \pi r_i^2}{(\text{interval length})(\text{geometric mean of trace lengths})^2} \quad (\text{Eq. 6})$$

where  $r$  is the radius of fracture  $i$ , or one-half the trace length of fracture  $i$ .

Fracture apertures are calculated by the cubic law with the fractures fully connected. The fracture aperture  $b$  is then given by (Bear et al. 1993 [116773], p. 15):

$$b = \left( \frac{12k}{f} \right)^{1/3} \quad (\text{Eq. 7})$$

where  $k$  is the fracture permeability. The fracture aperture determined in this way is an effective “hydraulic” aperture, not a “physical” aperture. Note that the above equation is modified from Equation 1.2.28 of Bear et al. (1993 [116773], p. 15). The  $k$  here refers to “bulk” fracture permeability rather than permeability in a fracture as defined by Bear et al. (1993 [116773], p. 15).

Fitted parameters are required to utilize the van Genuchten equation relating the effective saturation  $S_e$  and capillary pressure  $P_c$  (derived from Equations 2, 22, and 24 of van Genuchten 1980 [100610], pp. 892–895):

$$P_c = \frac{1}{\alpha} (S_e^{-1/m} - 1)^{1/n} \quad (\text{Eq. 8a})$$

where  $\alpha$ ,  $m$ , and  $n = \frac{1}{1-m}$  are the van Genuchten parameters. The effective saturation is defined by

$$S_e = \frac{S - S_r}{S_s - S_r} \quad (\text{Eq. 8b})$$

where  $S$  is total water saturation,  $S_s$  is saturated saturation, and  $S_r$  is residual saturation.

A simplified form of the Young-Laplace equation is assumed to directly calculate the van Genuchten fracture  $\alpha$  ( $\alpha_f$ ) from  $b$ . Note that the subscript  $f$  refers to fractures. The resulting relationship is:

$$\alpha_f = \frac{b}{2\tau_\sigma \cos\theta} \quad (\text{Eq. 9})$$

where  $\tau_\sigma$  is the surface tension of pure water at 20°C (0.072 N/m) and  $\theta$  is the contact angle. Essentially, Equation 9 states that van Genuchten  $\alpha$  can be estimated as the inverse of the air-entry value, which is often used in the soil science literature (Wang and Narasimhan 1993 [106793], p. 374). The contact angle  $\theta$  is set to be zero (Wang and Narasimhan 1993 [106793], p. 329), since the rock is expected to be water wetting, and no other specific data are available.

Fracture aperture and fracture van Genuchten alpha ( $\alpha_f$ ) are calculated from fracture frequency and fracture permeability estimates using Equations 7 and 9. The estimated mean apertures are approximately 100 to 400  $\mu\text{m}$  except for model layer tcw11, which had a relatively high fracture permeability, resulting in a higher estimated fracture aperture. The fracture van Genuchten alpha parameters ( $\alpha_f$ ) are on the order of  $10^{-3} \text{ Pa}^{-1}$ . There are large uncertainties in these values for the Calico Hills formation and lower units, because little or no fracture permeability and fracture frequency data are available.

The van Genuchten fracture  $m$  parameter ( $m_f$ ) is determined by fitting Equation 8a to the aperture-size distribution calculated from Equation 7. A  $m_f$  value of 0.633, determined based on the above method, is given in DTN: LB990501233129.001 [106787]. This value is used in this study. Note that an alternative method to estimate  $m_f$  is not available in the literature.

The developed fracture properties are given in Table 7.

Table 7. Fracture Properties for UZ Model Layers

UZ Model Layer	Permeability (m <sup>2</sup> )				Frequency (m <sup>-1</sup> )			Van Genuchten parameter			porosity (-)	Std (-)	Afm
	k <sub>G</sub>	log(k <sub>G</sub> )	σ <sub>log(k<sub>G</sub>)</sub>	N	f	σ <sub>f</sub>	N	α (Pa <sup>-1</sup> )	log(α)	m (-)			
tcw11	3.0E-11	-10.52	-	2	0.92	0.94	76	5.0E-3	-2.30	0.633	2.4E-2	-	1.56
tcw12	5.3E-12	-11.28	0.78	80	1.91	2.09	1241	2.2E-3	-2.66	0.633	1.7E-2	-	13.39
tcw13	4.5E-12	-11.35	1.15	3	2.79	1.43	60	1.9E-3	-2.73	0.633	1.3E-2	-	3.77
ptn21	3.2E-12	-11.49	0.88	12	0.67	0.92	76	2.7E-3	-2.57	0.633	9.2E-3	-	1
ptn22	3.0E-13	-12.52	0.20	4	0.46	-	-	1.4E-3	-2.86	0.633	1.0E-2	-	1.41
ptn23	3.0E-13	-12.52	0.20	4	0.57	-	63	1.2E-3	-2.91	0.633	2.1E-3	-	1.75
ptn24	3.0E-12	-11.52	-	1	0.46	0.45	18	3.0E-3	-2.53	0.633	1.0E-2	-	0.34
ptn25	1.7E-13	-12.78	0.10	7	0.52	0.6	72	1.1E-3	-2.96	0.633	5.5E-3	-	1.09
ptn26	2.2E-13	-12.66	-	1	0.97	0.84	114	9.6E-4	-3.02	0.633	3.1E-3	-	3.56
tsw31	8.1E-13	-12.09	-	-	2.17	2.37	140	1.1E-3	-2.96	0.633	5.0E-3	-	3.86
tsw32	7.1E-13	-12.15	0.66	31	1.12	1.09	842	1.4E-3	-2.86	0.633	8.3E-3	-	3.21
tsw33	7.8E-13	-12.11	0.61	27	0.81	1.03	1329	1.6E-3	-2.80	0.633	5.8E-3	-	4.44
tsw34	3.3E-13	-12.48	0.47	180	4.32	3.42	10646	6.7E-4	-3.18	0.633	8.5E-3	2.50E-03	13.54
alternate tsw34	1.5E-13	-12.81	0.75	180									
tsw35	9.1E-13	-12.04	0.54	31	3.16	-	595	1.0E-3	-2.99	0.633	9.6E-3	-	9.68
tsw3[67]	1.3E-12	-11.87	0.28	19	4.02	-	526	1.1E-3	-2.96	0.633	1.3E-2	-	12.31
tsw38	8.1E-13	-12.09	-	-	4.36	-	37	8.9E-4	-3.05	0.633	1.1E-2	-	13.34
tsw39	8.1E-13	-12.09	-	-	0.96	-	46	1.5E-3	-2.82	0.633	4.3E-3	-	2.95
ch1Ze	2.5E-14	-13.60	-	-	0.04	-	3	1.4E-3	-2.86	0.633	1.6E-4	-	0.11
ch1VI	2.2E-13	-12.66	-	-	0.10	-	11	2.1E-3	-2.69	0.633	6.1E-4	-	0.3
ch[23456]VI	2.2E-13	-12.66	-	-	0.14	-	25	1.9E-3	-2.73	0.633	7.7E-4	-	0.43
ch[2345]Ze	2.5E-14	-13.60	-	1	0.14	-	25	8.9E-4	-3.05	0.633	3.7E-4	-	0.43
ch6	2.5E-14	-13.60	-	-	0.04	-	-	1.4E-3	-2.86	0.633	1.6E-4	-	0.11
pp4	2.5E-14	-13.60	-	-	0.14	-	-	8.9E-4	-3.05	0.633	3.7E-4	-	0.43
pp3	2.2E-13	-12.66	-	-	0.20	-	-	1.6E-3	-2.78	0.633	9.7E-4	-	0.61
pp2	2.2E-13	-12.66	-	-	0.20	-	-	1.6E-3	-2.78	0.633	9.7E-4	-	0.61
pp1	2.5E-14	-13.60	-	-	0.14	-	-	8.9E-4	-3.05	0.633	3.7E-4	-	0.43
bf3	2.2E-13	-12.66	-	-	0.20	-	-	1.6E-3	-2.78	0.633	9.7E-4	-	0.61
bf2	2.5E-14	-13.60	-	-	0.14	-	-	8.9E-4	-3.05	0.633	3.7E-4	-	0.43
tr3	2.2E-13	-12.66	-	-	0.20	-	-	1.6E-3	-2.78	0.633	9.7E-4	-	0.61
tr2	2.5E-14	-13.60	-	-	0.14	-	-	8.9E-4	-3.05	0.633	3.7E-4	-	0.43

Output – DTN: LB0205REVUZPRP.001

NOTE: k is permeability (geometric mean).

σ is standard deviation.

N is number of samples.

f is fracture frequency.

α and m are fitting parameters for the van Genuchten water potential relationship.

Std refers to standard deviation for fracture porosity.

Afm refers to fracture matrix interface area (m<sup>2</sup>/m<sup>3</sup>).

“-“ means that no data are available

## 6.1.3 Fracture Porosity

### 6.1.3.1 General Strategy

Fracture porosity is herein defined as the effective porosity of fractures in which fluid flow and solute transport take place. In this study, a combination of porosity data derived from gas tracer tests in the ESF, and porosity estimates, based on the geometry of fracture networks, are used to develop representative fracture porosities for the UZ Model layers. The calculation of the

fracture porosity is documented in a Scientific Notebook (Wang 2003 [161654], SN-LBNL-SCI-215-V1, pp. 43–53).

Gas tracer tests were performed in the ESF to obtain estimates of the effective fracture porosity for the Topopah Spring middle nonlithophysal welded tuff, corresponding to the tsw34 model layer (DTN: LB980912332245.002 [105593]). Since gas tracer travel times through the fractured rocks are directly related to the storage of the corresponding fracture networks, analyses of tracer breakthrough data can provide reliable estimates of fracture porosity for the model layer tsw34.

Gas tracer test data are available only for model layer tsw34. Alternative approaches are available to estimate fracture porosity based on the geometry of fractures observed in the ESF. These geometric representations of porosity are used to apply the tsw34 value to the other units. The 1-D and 2-D porosities to be discussed below refer to porosities determined from 1-D borehole and 2-D mapping data, respectively. A so-called 2-D porosity for a model layer can be estimated using the aperture and the total fracture length per unit area (fracture intensity). The fracture intensity is based on tracer lengths given by the DLS in the ESF and the area enclosing the traces (see Equation 5). The equation used to calculate the 2-D porosity is:

$$\phi_{2-D} = bI \quad (\text{Eq. 10})$$

where  $I$  is the fracture intensity ( $\text{m}/\text{m}^2$ ) (DTN: LB990501233129.001 [106787]). When no intensity data are available (in cases where the unit does not intersect any portion of the ESF or ECRB Cross Drift) (BSC 2001 [159725], Section 6.1), the so-called 1-D porosity can be estimated by treating all fractures as continuous. The 1-D porosity is then calculated by:

$$\phi_{1-D} = b\bar{f} \quad (\text{Eq. 11})$$

Note that a large degree of uncertainty exists in the estimates based on Equations 10 and 11 for the following reasons. First, the estimated apertures are “hydraulic” apertures and may be very different from the average geometric apertures, since they are estimated based on air-permeability data. Second, Equations 10 and 11 only consider 2-D or 1-D geometric features, while actual fracture networks are three-dimensional. Therefore, direct estimates from these equations may not be reliable. However, it is reasonable to consider that these estimates would provide more reliable relative ratios of the fracture porosity for different stratigraphic units. Based on these considerations, a fracture porosity is determined by using the corresponding estimate from these equations to determine a ratio of fracture porosity between units. Because the porosity, based on analyses of the gas tracer tests, is available for the tsw34, this value was used with these ratios to estimate fracture porosity for the other units:

$$\phi_{\text{model layer x}} = \phi_{\text{tsw34}} \frac{\phi_{2-D, \text{model layer x}}}{\phi_{2-D, \text{tsw34}}} \quad \text{or} \quad \phi_{\text{model layer x}} = \phi_{\text{tsw34}} \frac{\phi_{1-D, \text{model layer x}}}{\phi_{1-D, \text{tsw34}}} \quad (\text{Eq. 12})$$

where  $\phi_{\text{tsw34}}$  is fracture porosity for tsw34, estimated from the gas tracer data, and  $\phi_{2-D}$  and  $\phi_{1-D}$  refer to values calculated using Equations 10 and 11, respectively. The developed fracture porosity values for the UZ Model layers are given in Table 7. All of these values are on the order of 1%. An alternative approach would have been to use 1% for all units. Use of this scaling

scheme for estimating fracture porosities is an approximation for determining the spatial variability of porosity among the model layers.

Note that the overall strategy is essentially a combination of the two general approaches available for estimating fracture porosities in the literature. The first approach is based on field tracer transport data. Researchers outside the Yucca Mountain Project have also used similar approaches. For example, inverse modeling was used to analyze a radially convergent flow tracer test in a fractured chalk formation, resulting in a calibrated fracture porosity of 0.3% (National Research Council 1996 [139151], pp. 292–293). The second general approach is based on the geometry of a fracture network. This approach considers all the fractures under consideration as connected and requires that fracture apertures can be exactly determined. Although a large degree of uncertainty exists in fracture porosity values estimated from this approach (for several reasons), this approach has often been used when field tracer test data are not available. For example, in their review of numerical approaches for modeling multiphase flow in fractured petroleum reservoirs, Kazemi and Gilman (1993 [147209], pp. 270–271, 312–313) discuss the determination of fracture porosity, based on fracture geometry data. Considering that gas tracer test data are only available for one model layer (tsw34) and a large degree of uncertainty exists when the second approach is used, use of both approaches provides significantly better estimates for fracture porosity in units through the UZ. A combination of the above two approaches makes the best use of the relevant data.

### 6.1.3.2 Fracture Porosity from Gas Tracer Testing Data

The estimated fracture porosities (DTN: LB980912332245.002 [105593]) were developed based on several simplifications (Figure 3): Flow and transport are two-dimensional; dispersion, gas compressibility and matrix diffusion are ignored; and the testing medium is homogeneous. The estimations were made using:

$$\phi_f^* = \frac{Qt_{0.5}}{\pi r_L^2 L} \quad (\text{Eq. 13})$$

where  $\phi_f^*$  is the estimated fracture porosity,  $Q$  is the volumetric withdrawal rate ( $Q_{\text{withdrawal}}$  in Figure 3),  $t_{0.5}$  is the mean travel time of tracer,  $r_L$  is the distance between the tracer injection and withdrawal zones, and  $L$  is the length of injection zone.

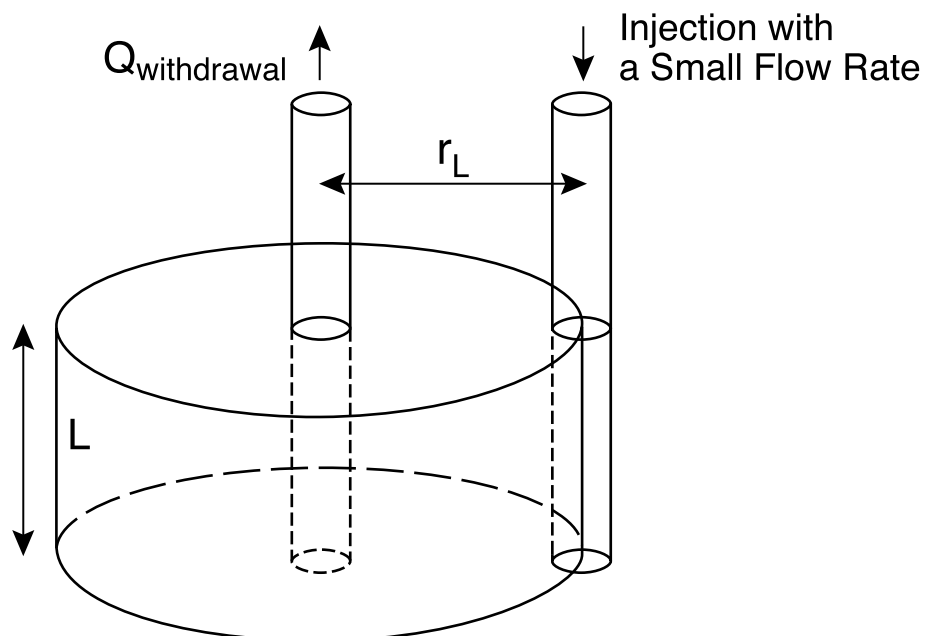


Figure 3. A Conceptual Model for Estimating Fracture Porosity Using Gas Tracer Testing Data

The average fracture porosity, estimated from Equation 13 using gas tracer data collected from the DST block and Niche 3107, is  $1.02\text{E-}2$  (DTN: LB980912332245.002 [105593]).

### 6.1.3.3 Effects of Several Factors on Fracture-Porosity Estimation Based on Gas Tracer Testing Data

The estimation of fracture porosity based on Equation 13 does not consider the effects of several factors: gas compressibility, heterogeneity, anisotropy, cavities, dispersion and matrix diffusion. Potential effects of these factors on estimating fracture porosity are discussed below.

Gas compressibility does not have a significant effect on the porosity estimation, because gas-pressure disturbances introduced by the gas tracer tests are small (relative pressure changes are on the order of several percent) as inferred from Appendix A of Freifeld (2001 [161806]).

Heterogeneity was ignored in estimating fracture porosity, based on Equation 13. It is reasonable to estimate an *effective* porosity by considering homogeneity within the measurement scale (on the order of several meters) considering that the scale is much smaller than a UZ-model-layer scale. Heterogeneity above the measurement scale is captured by standard deviation of the estimates. It is physically unjustified to estimate porosity variation below measurement (support) scales. (At a scale much smaller than the measurement scale, fracture porosity cannot be defined.) However, it should be noted that the heterogeneity below the measurement scale may have considerable effects on the fracture porosity estimates. If the tracer is injected into a fast path, the resulting analysis underestimates the fracture porosity. Otherwise, the analysis may overestimate the porosity. Nevertheless, those effects are reflected in the variability of the estimated fracture porosities.

Effects of anisotropy are essentially captured in porosity estimation because different configurations (orientations) were used in gas tracer tests performed in the Drift Scale Test block and Niche 3107.

Not enough data exist to evaluate effects of cavities on porosity estimation in detail. However, appropriateness of the estimates can be partially demonstrated by comparing them with those from the other sites without cavities, which will be discussed later on. A discussion of cavity porosities and their estimates for geological units corresponding to the proposed repository horizon is given in BSC (2002 [160319], p. 86, Table 7-10).

While the dispersion process is not expected to significantly affect the average trace travel time used to calculate fracture porosity (Equation 13), Moench (1989 [101146], Figure 2) implies that considering dispersion may result in larger porosity estimates than those determined from Equation 13 (Wang 2003 [161654], SN-LBNL-SCI-215-V1, p. 53). Therefore, ignoring dispersion may partially compensate for the effects of cavities. Also, note that dispersion is a result of spatial variability of permeability within testing rocks.

The determination of fracture porosity depends on the tracer travel times. Diffusion of trace into the matrix delays the breakthrough and causes overestimation of fracture porosity. Effects of matrix diffusion on the fracture porosity estimation can be quantified by an analytical solution. Based on mass balance, radial tracer transport in a system (with matrix diffusion) like that shown in Figure 3 can be described by the following differential equation (Wang 2003 [161654], SN-LBNL-SCI-215-V1, pp. 44–45):

$$\frac{\partial c}{\partial t} + \frac{q_{fw}}{\phi_f} \frac{\partial c}{\partial r_s} = \frac{A_{fm}\phi_m S_{mg} D_m}{\phi_f} \frac{\partial c_m}{\partial x} \quad x=0 \quad (\text{Eq. 14})$$

with

$$q_{fw} = \frac{Q}{2\pi r_w L} \quad (\text{Eq. 15})$$

$$r_s = \frac{1}{2} \frac{r_L^2 - r^2}{r_w} \quad (\text{Eq. 16})$$

and

$$D_m = D_0 \tau \quad (\text{Eq. 17})$$

where  $c$  is the tracer concentration in fractures at a location with a distance  $r$  from the withdrawal borehole, and at time  $t$ ,  $r_w$  is the radius of withdrawal borehole,  $\phi_f$  is fracture porosity (considering matrix diffusion),  $A_{fm}$  is the fracture-matrix interface area per unit volume of bulk rock,  $\phi_m$  is the matrix porosity,  $S_{mg}$  is the gas saturation in the matrix,  $D_0$  is the molecular-

diffusion coefficient for gas in air,  $\tau$  is the tortuosity factor,  $c_m$  is the tracer concentration in the matrix, and  $x$  is the distance from the fracture-matrix interface.

Equation 14 is similar enough in form to Equation 4 of Starr et al. (1985 [101479]) that the solution to Equation 14 can be obtained from it. Under conditions of continuous injection with concentration  $c_0$ , Starr et al. (1985 [101479]) derived the solution to their Equation 4 as follows:

$$\frac{c}{c_0} = 0 \quad T^0 < 0 \quad (\text{Eq. 18})$$

$$\frac{c}{c_0} = \text{erfc}\left(\frac{A^0}{T^0}\right) \quad T^0 > 0 \quad (\text{Eq. 19})$$

where  $A^0$  and  $T^0$  are functions of the relevant transport parameters (Starr et al. 1985 [101479], p. 1044). The corresponding relations between transport parameters here and those of Starr et al. (1985 [101479]) can be easily obtained by comparing Equation 14 with their Equation 4. Based on these relations and using  $r_{sw} = \frac{1}{2}(r_L^2 - r_w^2)/r_w \cong 1/2 r_L^2/r_w$  for  $r_w \ll r_L$ , expressions for  $A^0$  and  $T^0$  at the withdrawal borehole ( $r = r_w$ ) can be obtained from the corresponding expressions of Starr et al. (1985 [101479], p. 1044) (Wang 2003 [161654], SN-LBNL-SCI-215-V1, pp. 46–47):

$$A^0 = \frac{A_{fm}\phi_m S_{mg} D_m^{1/2} (\pi L r_L^2)}{2Q} \quad (\text{Eq. 20})$$

$$T^0 = \left(t - \frac{\phi_f r_L^2 \pi L}{Q}\right)^{1/2} \quad (\text{Eq. 21})$$

Note that under continuous tracer injection conditions, average tracer travel time  $t_{0.5}$  corresponds to 50% of the relative tracer concentration:

$$\frac{c(t_{0.5})}{c_0} = \text{erfc}\left[\frac{A^0}{T^0(t_{0.5})}\right] = 0.5 \quad (\text{Eq. 22})$$

Combining Equations 13 with 20-22 yields

$$\frac{\phi_f}{\phi_f^*} = 1 - \frac{t_{0.5}}{\phi_f^*} D_m \left[ \frac{A_{fm}\phi_m S_{mg}}{2\beta} \right]^2 \quad (\text{Eq. 23})$$

where  $\beta$  is a constant (0.48) defined by  $\text{erfc}(\beta) = 0.5$  and determined from Domenico and Schwartz (1990 [100569], p. 637). The  $\phi_f$  and  $\phi_f^*$  are identical if the matrix diffusion does not exist ( $D_m = 0$ ), as shown in Equation 23. This equation can be used to correct the porosity

estimates from Equation 13 to consider the effects of matrix diffusion. Values for  $A_{fm}$  and  $\phi_m$  (for tsw34) are available from DTN: LB990501233129.001 [106787]. The travel time  $t_{0.5}$  is calculated using Equation 13 from DTN: LB980912332245.002 [105593]. The average  $t_{0.5}$  is 210 min and average  $\phi_f^*$  is 1.02E-2 (Wang 2003 [161654], SN-LBNL-SCI-215-V1, pp. 48–49).  $S_{mg}$  (0.1) is calculated from the average matrix water saturation within tsw34 (DTN: MO0109HYMXPROP.001 [155989]). The value for  $D_m$  is calculated from Equation 17.  $D_0$  (2.65E-5 m<sup>2</sup>/s) is determined from Pruess (1987 [100684], pp. 5–6):

$$D_0 = \frac{D_{va}^0}{P} \left( \frac{T + 273.15}{273.15} \right)^\theta \quad (\text{Eq. 24})$$

with  $D_{va}^0 = 2.3\text{E-}5 \text{ m}^2/\text{s}$  and  $\theta = 1.80$  for a temperature of 20°C and an air pressure of 1 bar. The tortuosity for the gas tracer is estimated from the well-known relation of Millington and Quirk (1961 [139143]):

$$\tau = \frac{\theta_g^{7/3}}{\phi_m^2} \quad (\text{Eq. 25})$$

where  $\theta_g = \phi_m S_{mg}$  is the volumetric gas content in the matrix. Substituting the determined parameter values (including the average  $t_{0.5}$  and  $\phi_f^*$  values) into the right hand of Equation 23 yields:

$$\frac{\phi_f}{\phi_f^*} = 0.83 \quad (\text{Eq. 26})$$

This factor is used to consider the effects of matrix diffusion (on average) by multiplying the porosity estimates in DTN: LB980912332245.002 [105593] by the factor value of 0.83. The resultant average fracture porosity for tsw34 is 0.0085, and the corresponding standard deviation is 2.5E-3. This porosity value is used in Equation 12 for determining fracture porosities in other UZ Model layers. The final fracture-porosity estimates are given in Table 7. Note that uncertainty exists in the estimated porosity value (Equation 26). However, it is difficult to quantify this uncertainty for the given data because site-specific parameter values calculating this ratio are not available for a tracer test. Nevertheless, as shown in Section 6.1.3.4, the fracture porosity values estimated using Equation 26 are reasonable compared with values determined from other sources in the UZ and from other sites.

#### 6.1.3.4 Comparisons with Fracture Porosities Estimated from Other Sources

To demonstrate the reasonableness of the fracture porosity estimates (given in Table 7), these estimates were compared with those determined from other sources in the UZ and from other sites.

- Fracture porosities were also estimated from water content data calculated from water travel times observed from water release tests in the Tptpmn (tsw34) of the UZ (DTNs: LB980901233124.003 [105592]; LB0110LIQR0015.001 [156907]) (See Section 6.5 of

this report). The mean value of the estimates is  $\phi_f = 0.018$  and the standard deviation is 0.014.

- CRWMS M&O (2001 [153045], Table 9) reports fracture porosity estimates obtained by inversion of the seepage data collected in the Tptpmn unit. The mean and standard deviation are 0.011 and 0.008, respectively.
- Fracture porosity was estimated from gas pressure data collected from Apache Leap Research Site (Neuman et al. 2001 [160849], p. 320). The estimated mean and standard deviation are 0.014 and 0.0017, respectively.
- Fracture porosity for a fractured chalk formation, estimated using inversion modeling of a tracer test, was 0.003 (National Research Council 1996 [139151], p. 293).
- Fracture porosities estimated from gas tracer tests in the northern Ghost Dance Fault in the UZ range were from 0.001 to 0.07 (LeCain et al. 2000 [144612], Table 18).
- Preliminary estimates based on water travel times observed from water release tests in Tptpll (tsw35) were 0.013 and 0.067. The small porosity value is believed to mainly result from the fracture network rather than cavities (BSC 2001 [158463], Section 6.11.3.2, p. 246). This value is close to the current estimate for Tptpll (0.0096).
- The calibrated fracture porosity, based on the Alcove 1 infiltration test data, was about 0.028 (BSC 2001 [158726], Section 6.8.1.2, Table 6-33). The test site is located in the upper portion of the tcw unit. The calibrated value was close to the current estimate for tcw11 (0.024) (Table 7).

These fracture porosity values (obtained using different methodologies, based on different types of data and/or from different sites) are consistent with the current estimates (given in Table 7) that are on the order of 1%, indicating the reasonableness of these estimates.

## 6.2 MATRIX PROPERTIES

Matrix properties include matrix permeability and van Genuchten (1980 [100610]) parameters used to describe water retention and relative permeability relations. They were determined from laboratory measurements made on core samples from the UZ. Some boreholes from which core samples came are shallow, variously penetrating the TCw, PTn, and top portions of the TSw. There are some deep boreholes from which core samples have been collected and analyzed for the entire depth: NRG-6, NRG-7a, SD-7, SD-9, SD-12, UZ-7a, UZ-14, and UZ#16. Six of these penetrate into the Calico Hills Formation, five penetrate into the Prow Pass Tuff, and one, SD-7, penetrates the Bullfrog and Tram Tuffs. Core samples have also been collected from portions of two other deep boreholes: SD-6 and WT#24. All the associated DTNs and their use can be found in the description of the relevant Excel files in Attachment III of this report.

Sample collection and laboratory measurement methodologies, as well as estimates of core uncertainty, are described by Flint (1998 [100033], pp. 11–19) and Rousseau et al. (1999 [102097], pp. 125–153). Core samples are grouped and analyzed according to the hydrogeologic units characterized by Flint (1998 [100033], pp. 19–46) and detailed in a Scientific Notebook

(Wang 2003 [161654], SN-LBNL-SCI-003-V2, pp. 57–83). Table 4 shows these hydrogeologic units in relation to the lithostratigraphy of GFM2000 and the UZ Model layers.

The calculation of matrix properties is described in a Scientific Notebook (Wang 2003 [161654], SN-LBNL-SCI-003-V2, pp. 57–83). Calculated matrix properties are given in Table 8. The Excel files used to perform these calculations are listed and described in Attachment III. The matrix porosity and permeability values are calculated with hydroprops\_fin.xls (Attachment III). The unsaturated hydraulic properties are calculated with MRC\_Q\_TCw\_fin.xls, MRC\_Q\_PTn\_fin.xls, MRC\_Q\_TSw\_fin.xls, MRC\_Q\_CHCF\_fin.xls, vG\_Summary\_fin.xls, and PV2 deep borehole data.xls (Attachment III).

Table 8. Matrix Properties Developed from Core Data

HGU	$\phi$	$\sigma$	n	SE	upscaled	upscaled	$\sigma_{\log(k)}$	n	nd	SE <sub>log(k)</sub>	1/ $\alpha$	log(1/ $\alpha$ )	SE <sub>log(1/<math>\alpha</math>)</sub>	m	SE	S <sub>r</sub>	$\eta$	SE
					k	log(k)												
CCR & CUC	0.241	0.073	124	0.007	4.7E-15	-14.33	0.47	3	0	0.27	8.27E+4	4.918	0.279	0.388	0.085	0.02	3.47	17.88
CUL & CW	0.088	0.032	694	0.001	6.4E-20	-19.20	2.74	15	25	0.43	5.46E+5	5.737	0.178	0.280	0.045	0.20	12.29	19.35
CMW	0.200	0.055	96	0.006	1.8E-16	-15.74	2.38	5	1	0.97	2.50E+5	5.398	0.188	0.259	0.042	0.31	6.08	0.00
CNW	0.387	0.069	104	0.007	4.0E-14	-13.40	2.05	10	0	0.65	2.03E+4	4.308	0.199	0.245	0.032	0.24	-2.58	0.33
BT4	0.428	0.100	58	0.013	4.1E-13	-12.39	1.41	11	0	0.43	4.55E+3	3.658	0.174	0.219	0.019	0.13	-0.26	1.17
TPY	0.233	0.057	39	0.009	1.3E-15	-14.90	0.64	2	0	0.46	7.63E+4	4.883	0.379	0.247	0.064	0.07	3.46	16.73
BT3	0.413	0.082	73	0.010	1.3E-13	-12.87	1.09	11	1	0.31	8.90E+3	3.950	0.088	0.182	0.008	0.14	-0.56	0.49
TPP	0.498	0.041	159	0.003	1.1E-13	-12.96	0.39	11	0	0.12	2.12E+4	4.325	0.104	0.300	0.023	0.06	0.26	0.42
BT2	0.490	0.095	176	0.007	6.7E-13	-12.17	1.12	21	0	0.24	1.74E+4	4.239	0.170	0.126	0.013	0.05	-2.64	0.67
TC	0.054	0.036	75	0.004	4.4E-17	-16.36	3.02	6	5	0.91	2.71E+5	5.432	0.310	0.218	0.054	0.21	6.14	17.21
TR	0.157	0.030	449	0.001	3.2E-16	-15.50	0.94	46	1	0.14	9.43E+4	4.974	0.116	0.290	0.025	0.07	5.00	17.49
TUL	0.155	0.030	438	0.001	2.8E-17	-16.56	1.61	37	12	0.23	1.75E+5	5.244	0.111	0.283	0.024	0.12	7.06	17.98
TMN	0.111	0.020	277	0.001	4.5E-19	-18.34	0.97	74	35	0.09	1.40E+6	6.147	0.108	0.317	0.042	0.19	10.90	19.28
TLL	0.131	0.031	502	0.001	3.7E-17	-16.44	1.65	51	24	0.19	6.01E+4	4.779	0.521	0.216	0.061	0.12	6.27	17.23
TM2 & TM1	0.103	0.025	298	0.001	2.3E-20	-19.63	3.67	21	42	0.46	3.40E+6	6.532	0.097	0.442	0.073	0.20	14.48	21.25
PV3	0.043	0.040	125	0.004	2.9E-18	-17.54	1.57	16	2	0.37	1.00E+6	6.000	0.278	0.286	0.065	0.42	9.04	18.53
PV2a	0.275	0.096	13	0.027	a	a	a	a	a	a	2.17E+5	5.336	0.156	0.059	0.007	0.36	5.03	15.63
PV2v	0.229	0.132	40	0.021	4.3E-13	-12.37	1.38	16	0	0.34	1.94E+4	4.287	0.042	0.293	0.011	0.13	-0.19	0.23
BT1a	0.285	0.051	46	0.008	3.5E-17	-16.45	2.74	9	1	0.87	4.72E+6	6.674	0.183	0.349	0.073	0.38	7.39	18.61
BT1v	0.331	0.091	76	0.010	2.1E-13	-12.67	1.11	35	0	0.19	1.35E+4	4.131	0.049	0.240	0.008	0.06	-2.07	0.23
CHV	0.346	0.049	130	0.004	1.6E-12	-11.81	1.62	46	0	0.24	3.39E+3	3.530	0.094	0.158	0.008	0.06	-3.80	0.23
CHZ	0.322	0.048	520	0.002	5.2E-18	-17.28	0.91	99	17	0.08	4.45E+5	5.649	0.094	0.257	0.022	0.26	8.30	18.10
BTa	0.271	0.046	73	0.005	8.2E-19	-18.08	2.05	9	8	0.50	6.42E+6	6.808	0.043	0.499	0.036	0.36	11.87	21.01
BTv	b	b	b	b	b	b	b	b	b	b	5.04E+4	4.703	0.207	0.147	0.020	b	-0.87	14.77
PP4	0.321	0.047	52	0.006	1.5E-16	-15.81	2.74	6	2	0.97	5.00E+5	5.699	0.401	0.474	0.224	0.29	7.13	19.55
PP3	0.318	0.032	168	0.002	6.4E-15	-14.20	0.75	51	0	0.11	1.32E+5	5.120	0.084	0.407	0.031	0.08	3.37	18.01
PP2	0.221	0.058	127	0.005	5.4E-17	-16.27	1.18	34	3	0.19	6.22E+5	5.794	0.147	0.309	0.041	0.10	6.69	18.09
PP1	0.297	0.043	280	0.003	8.1E-17	-16.09	1.52	27	1	0.29	1.13E+5	5.052	0.234	0.272	0.036	0.30	6.05	17.63
BF3/TR3	0.175	0.104	126	0.009	1.1E-15	-14.95	1.64	7	1	0.58	8.94E+4	4.951	0.931	0.193	0.117	0.11	3.11	16.20
BF2	0.234	0.049	40	0.008	c	c	c	c	c	c	8.46E+6	6.927	0.032	0.617	0.070	0.21	8.86	21.17

Output – DTN: LB0207REVUZPRP.002

NOTE: (a) BT1a was used as an analog for permeability because only one permeability data point is available for PV2a.  
 (b) BT1v was used as an analog for porosity, residual saturation, and permeability because only one sample is available for BTv.  
 (c) PP1 was used as an analog for permeability because only one measurable permeability data point is available for BF2.

k is permeability.  
 $\sigma$  is standard deviation.  
 n is number of samples.  
 $\phi$  is porosity.  
 nd is number of samples with non-detected permeability measurements.  
 $\alpha$  and m are fitting parameters for the van Genuchten water potential relationship.  
 SE is standard error.  
 S<sub>r</sub> is residual liquid saturation.  
 $\eta$  is defined in Equation 34.  
 HGU refers to hydrogeologic units. Relation between HGU and UZ model layers is given in Table 4.  
 E-15 is the same as 10<sup>-15</sup>.

### 6.2.1 Matrix Permeability

Matrix permeability was measured on core samples from several boreholes (including SD-6 and WT#24) at Yucca Mountain. Measurements are available for layers from the CUC down to the BF2 (Table 8). Two different permeameters were used to measure permeability, with the detection limit of the first higher than the second. Most of the samples were tested using the first

permeameter; the second was used to test some new samples and retest some old samples tested using the first permeameter, including some with permeabilities too low to measure (nondetect results). When the same sample was tested on both permeameters, the permeability measured on the one with the lower detection limit was used. This was because the permeameter with the lower detection limit was expected to result in a more reliable measurement.

The measured data are presented in terms of saturated hydraulic conductivity (m/s),  $K$ , which is converted to permeability ( $m^2$ ),  $k$ , by the following relationship

$$k = \frac{K\mu_w}{g\rho_w} \quad (\text{Eq. 27})$$

where  $\mu_w$  is the viscosity of water ( $0.001 \text{ N s/m}^2$ ),  $g$  is the acceleration of gravity ( $9.81 \text{ m/s}^2$ ), and  $\rho_w$  is the density of water ( $998 \text{ kg/m}^3$ ). These parameter values correspond to a temperature of  $20^\circ\text{C}$  (a typical room temperature at which the hydraulic conductivities were measured) (Lide 2002 [160832], p. 6-3).

Permeability is considered to be a log-normally distributed quantity (Gelhar 1993 [101388], p. 2). Therefore, the geometric mean was used to represent the average permeability of each model layer. The standard deviation of the log-transformed permeabilities,  $\log(k)$ , is used as the basis for uncertainty, which is detailed below. Where there are no nondetect measurements in the data set for a layer, the calculation of the average and standard deviation of the data is simple. When there are nondetect measurements present, they must be taken into account because they may represent important information about the extent of the lognormal distribution below the detection limit. They are taken into account as follows:

- All data points, including nondetects, are ranked and assigned a percentile.
- The data points are fit to a lognormal distribution, based on their percentile ranking. The fitting parameters are  $k_g$ , the geometric mean of the permeability data, and  $\sigma_{\log(k)}$ , the standard deviation of the log transformed permeability data.

The geometric mean permeabilities calculated above represent the average behavior of the core-scale samples. For a given model layer, this averaged permeability can be very different from the effective matrix permeability used to represent large-scale water flow and solute transport due to the scale effects (e.g., Paleologos et al. 1996 [105736], Figure 4, p. 1337). While many upscaling methods are available in the literature, a method for highly heterogeneous porous media is described by the following expression (Paleologos et al. 1996 [105736], p. 1336)

$$k_e = k_g \exp\left[\sigma_{\ln(k)}^2 \left(\frac{1}{2} - D\right)\right] \quad (\text{Eq. 28})$$

where  $k_e$  is the effective permeability,  $k_g$  is the geometric mean of small (core) scale permeability,  $\sigma_{\ln(k)}^2$  is the variance of the natural log-transformed permeability, and  $D$  is a function of spatial dimensions (e.g. 2-D and 3-D) and the correlation scale of  $\ln(k)$ . Note that the geometric mean permeability is not the same as the effective permeability in a general case. For a 3-D isotropic problem,  $D = 1/3$  when the characteristic size of a flow domain under

consideration (say, a model layer) is much larger than the correlation length (Paleologos et al. 1996 [105736], p. 1336). For a site-scale model layer, these conditions are approximately satisfied. In this case, Equation 28 can be rewritten as

$$\log(k_e) = \log(k_g) + 0.38\sigma_{\log(k)}^2 \quad (\text{Eq. 29})$$

where  $\sigma_{\log(k)}^2$  is the variance of the log transformed permeability.

In these layers, the amount of upscaling predicted by Equation 28 is as large as five orders of magnitude. An upper limit of 1.5 orders-of-magnitude upscaling is imposed on layers CUL and CW, CMW, CNW, TC, TM2 and TM1, and BT1a and PP4 (Assumption 1). For all other layers, the amount of upscaling predicted by Equation 28 is less than 1.5 orders of magnitude. Use of this limiting scheme is based mainly on the following consideration. Equation 28 was developed for a porous medium (single continuum), and can only be considered as an approximation for a dual-continuum system. For example, the existence of fractures, which may act as a capillary barrier, can increase tortuosity of liquid water flow in the matrix and therefore reduce the effective permeability compared to the case without fractures. This situation is not considered in Equation 28.

### 6.2.2 Porosity

Matrix porosity was also measured on core samples from the UZ. Porosity was determined after drying samples in a 105°C oven for at least 48 hours to obtain a standard dry weight (Flint 1998 [100033], p. 17). Porosity is considered to be a normally distributed quantity, so the arithmetic mean of core measurements and standard deviation were used to characterize the porosity for a model layer.

### 6.2.3 Matrix van Genuchten Parameters

The relationships described by van Genuchten (1980 [100610], pp. 892–893) were used to characterize unsaturated flow in the matrix of Yucca Mountain. Use of the water potential versus saturation relationship allows the prediction of the relative permeability relationship. The predicted relative permeability is compared with permeability data where available.

The van Genuchten parameters are  $S_s$  (satiated saturation),  $S_r$  (residual saturation),  $\alpha$ , and  $m$ . Satiated saturation is defined to be 1.0, i.e., residual gas saturation is neglected. Residual saturation is calculated based on two porosity measurements as described below. With satiated and residual saturation fixed,  $\alpha$  and  $m$  are adjusted to fit water potential and saturation data.

#### 6.2.3.1 Residual Saturation

Residual saturation was determined from relative humidity (RH) porosity and total porosity. RH porosity was measured after drying a sample for 48 hours in a 60°C and 65% relative humidity oven. This process is designed to remove water from the pores that contributes to flow, leaving only bound water and water in the smallest pores (Flint 1998 [100033], pp. 17–18). Layer average values for RH porosity are calculated in the same manner as total porosity (see Section 6.2.2). The layer average values of RH porosity are subtracted from the layer average values of total porosity to provide an estimate of residual water content (i.e., the amount of water left in the

pores and bound to the minerals after relative permeability (or hydraulic conductivity) has been reduced to zero). Residual saturation was calculated by dividing the residual water content by total porosity.

### 6.2.3.2 Matrix $\alpha$ and $m$

Desaturation data (water potential and saturation) from a number of samples (at least one for each layer) were measured, while a core sample was drying. DTNs associated with these data and their uses are given in descriptions of Excel files MRC\_Q\_TCw\_fin.xls, MRC\_Q\_PTn\_fin.xls, MRC\_Q\_Tsw\_fin.xls, and MRC\_Q\_CHCF\_fin.xls (Attachment III of this report). These data were used to calculate the  $\alpha$  and  $m$  parameters for each layer by fitting to Equation 8. The best-fit parameters were obtained by minimizing the sum of the squared saturation residuals,

$$\sum_{i=1}^n r_i^2 = \sum_{i=1}^n (S_i - S(\Psi_i))^2 \quad (\text{Eq. 30})$$

where  $r_i$  is a saturation residual,  $n$  is the number of saturation and water potential data pairs for a layer,  $S_i$  is a saturation data point, and  $S(\Psi_i)$  is the saturation predicted by the van Genuchten relationship for water potential,  $\Psi_i$ .

The uncertainty or standard error of  $\alpha$  and  $m$  is given by the diagonal terms of the covariance matrix,

$$\mathbf{C} = s_0^2 (\mathbf{J}^T \mathbf{J})^{-1} \quad (\text{Eq. 31})$$

where  $\mathbf{C}$  is the covariance matrix,  $s_0^2$  is the error variance, and  $\mathbf{J}$  is the Jacobian matrix. It should be noted that standard error,  $SE$ , can be related to the standard deviation,  $\sigma$ , which is given for other properties, by

$$SE = \frac{\sigma}{\sqrt{n}} \quad (\text{Eq. 32})$$

### 6.2.4 Matrix Relative Permeability

DTNs associated with data (used for calculating relative permeability) and their uses are given in descriptions of Excel files MRC\_Q\_TCw\_fin.xls, MRC\_Q\_PTn\_fin.xls, MRC\_Q\_Tsw\_fin.xls, MRC\_Q\_CHCF\_fin.xls, and VG\_Summary\_fin.xls (Attachment III of this report). According to van Genuchten (1980 [100610], p. 893), relative permeability ( $k_r$ ) can be related to effective water saturation ( $S_e$ ) as

$$k_r = S_e^{1/2} \left\{ [1 - (1 - S_e^{1/m})]^m \right\}^2 \quad (\text{Eq. 33})$$

However, recent studies indicate that a more general expression for relative permeability is (Schaap and Leij 2000 [160841], pp. 843–844):

$$k_r = S_e^\eta \left\{ [1 - (1 - S_e^{1/m})]^m \right\}^2 \quad (\text{Eq. 34})$$

where  $\eta$  is an empirical constant. Many studies show that  $\eta$  is not 0.5 as assumed by van Genuchten (1980 [100610]), but varies over a very large range (Schaap and Leij 2000 [160841], pp. 843–844). This is consistent with the matrix relative permeability data collected from the UZ.

To determine an  $\eta$  estimate for a UZ model layer, the following equation was used to fit the unsaturated conductivity ( $K$ ) data collected within the model layer:

$$\frac{K(S_e)}{K(S_0)} = \frac{S_e^\eta \left\{ [1 - (1 - S_e^{1/m})]^m \right\}^2}{S_0^\eta \left\{ [1 - (1 - S_0^{1/m})]^m \right\}^2} \quad (\text{Eq. 35})$$

$K(S_0)$  is the conductivity at a saturation  $S_0$ , which is selected to be close to one. Equation 35 is derived by writing Equation 34 for a general value of  $S_e$  and for  $S_e=S_0$ . The fitted  $\eta$  values are reported in Table 8 for different model layers (Wang 2003 [161654], SN-LBNL-SCI-003-V2, pp. 63–83). They range from –2.58 to 14.48, which are consistent with cited by Schaap and Leij (2000 [160841], p. 844). Note that directly fitted  $\eta$  values are available only for hydrogeologic units CMW, CNW, BT4, BT3, TPP, BT2, PV2v, BT1v and CHV where unsaturated hydraulic conductivity data are collected (Table 8). For other units, the following empirical relation is used to estimate the  $\eta$  values:

$$\eta = Am - B \log(k) + C \quad (\text{Eq. 36})$$

and the corresponding standard errors are estimated by

$$SE_\eta = SE_A m - SE_B \log(k) + SE_C \quad (\text{Eq. 37})$$

where  $k$  is absolute permeability and  $A$  (8.14),  $B$  (1.99), and  $C$  (-28.24) are empirical parameters determined by fitting Equation 36 to  $\eta$  values for hydrogeologic units CMW, CNW, BT4, BT3, TPP, BT2, PV2v, BT1v and CHV where unsaturated hydraulic conductivity data are collected (Wang 2003 [161654], SN-LBNL-SCI-003-V2, pp. 63–83).  $SE_A$ ,  $SE_B$ , and  $SE_C$  are the standard errors for  $A$ ,  $B$ , and  $C$ , respectively, and determined from the curve fitting (Wang 2003 [161654], SN-LBNL-SCI-003-V2, p. 82). Values calculated from Equations 36 and 37 are reported in Table 8.

A comparison between the currently obtained results based on Equation 34 and the van Genuchten relative permeability-saturation relation, Equation 33 can be easily made with

$$\frac{k_r(S_e)}{k_{r,VG}(S_e)} = S_e^{\eta-0.5} \quad (\text{Eq. 38})$$

where subscript “VG” refers to relative permeability obtained from the van Genuchten relation, Equation 33. Equation 38 is derived from Equations 33 and 34. Since estimated  $\eta$  values were very different from 0.5 for many model layers (Table 8), relative permeabilities predicted with van Genuchten relation, Equation 33, have considerable errors, especially for low saturations.

The errors become insignificant for saturations close to one, which is the case for welded units under the ambient conditions. Also note that a large degree of uncertainty in estimated  $\eta$  values exists because of data limitations. Therefore, the van Genuchten relation is still used in modeling studies in this report.

### 6.3 THERMAL PROPERTIES

Thermal properties include rock grain density, dry and wet rock thermal conductivities, rock grain specific heat capacity, matrix porosity, lithophysae porosity, and fracture porosity (Table 7). These properties are basic inputs into model studies involving heat flow.

Thermal properties for the UZ Model layers were developed from the thermal-property data for the various lithostratigraphic layers (DTNs: SN0206T0503102.005 [160258] and SN0208T0503102.007 [160257]). The first of these two DTNs supplies thermal properties for most of the lithostratigraphic layers except the geological layers at the proposed repository horizon. The second DTN deals with thermal properties of the geological layers in the repository horizon, namely the upper lithophysal, the middle nonlithophysal, the lower lithophysal, and the lower nonlithophysal stratigraphic units of Topopah Spring welded tuff. The development of data in DTN: SN0208T0503102.007 [160257] is discussed in a Model Report entitled *Thermal Conductivity of the Potential Repository Horizon Model Report* (BSC 2002 [160319]).

The matrix porosities in DTN: SN0206T0503102.005 [160258] and DTN: SN0208T0503102.007 [160257] are based on petrophysical measurements. Borehole petrophysical measurements of bulk density and neutron porosity are used to make quantitative estimates of matrix porosity (BSC 2002 [160319], Section 4). These data provide substantial information regarding the spatial heterogeneity of porosity across the entire site. To arrive at the thermal conductivities of the geological layers in the model reports mentioned above, those matrix porosity data (as well as the thermal conductivity of the solid minerals, and the geometry and connectivity of the solid) were treated as spatial random functions (BSC 2002 [160319]). A geostatistical method, sequential Gaussian simulation, was used to develop 50 independent, equally likely realizations of these uncertain properties. The measured porosity data (and other data) were used to condition the geostatistical simulations. These conditioned property sets then served as inputs to the matrix thermal conductivity model, yielding geostatistically based realizations of the matrix thermal conductivity. Since the developed matrix thermal-conductivity data were dependent on the input matrix porosity data, the porosity data in the above two DTNs are adopted as appropriate matrix porosities in preference to those given in Table 8 for the thermal property set.

The correlation of the UZ Model layers with the geological units is shown in Table 4. In most cases, a UZ Model layer directly corresponds to a unique lithostratigraphic unit. In such instances, the thermal properties are adopted directly from their corresponding stratigraphic unit without alteration. On the other hand, when a UZ Model layer is composed of two or more adjacent lithostratigraphic units, the averaging technique of Francis (1997 [127326], pp. 5–7) is used for estimating the properties while assuming an equal thickness for all the relevant units. The conceptual model underlying this technique is that heat flow is one-dimensional and in a direction normal to interfaces between the units under consideration. This is appropriate considering that heat flow in the ambient system and in the disturbed system (during repository

heating) at Yucca Mountain is predominantly vertical. (This is because the horizontal dimensions of the repository horizon are much larger than the vertical dimension.) The corresponding equivalent thermal conductivity ( $\lambda_{wet\ or\ dry,\ eq}$ ), grain density ( $\rho_{g,eq}$ ), and heat capacity ( $C_{p,eq}$ ) are calculated using the following equations which were derived from those of Francis (1997 [127326], pp. 5–7) assigning a uniform thickness for different geologic units within each model layer containing more than one geologic units (Table 4):

$$\lambda_{k,eq} = \frac{n \prod_{i=1}^n \lambda_{k,i}}{\sum_{j=1}^n \left( \prod_{i=1, i \neq j}^n \lambda_i \right)} \quad (k = \text{wet or dry}) \quad (\text{Eq. 39})$$

$$\rho_{g,eq} = \frac{\sum_{i=1}^n \rho_{g,i}}{n} \quad (\text{Eq. 40})$$

$$C_{p,eq} = \frac{\sum_{i=1}^n C_{p,i} \rho_{g,i}}{n \rho_{g,eq}} \quad (\text{Eq. 41})$$

where  $n$  is the total number of the involved lithostratigraphic units, and  $\lambda_{g,i}$ ,  $\rho_{g,i}$  and  $C_{p,i}$  are heat conductivity, grain density, and heat capacity, respectively, for a lithostratigraphic unit  $i$ . Note that the use of an equal thickness for all the relevant units within a model layer is adequate here because differences between thermal properties for these units (within a model layer) are not significant. Additionally, resultant matrix porosities are the simple arithmetic mean of the porosities for the constituent stratigraphic units. The determined thermal properties for the UZ Model layers are given in Table 9. The determination of the properties is described in a Scientific Notebook (Wang 2003 [161654], SN-LBNL-SCI-100-V3, pp. 69–79).

The thermal conductivities listed in Table 9 are matrix thermal conductivities. For lithophysal stratigraphic units and corresponding UZ Model layers, it is often necessary to use the bulk thermal conductivities instead of the matrix thermal conductivities. For stratigraphic units Tptpul, Tptpmn, Tptpll and Tptpln (or UZ Model layers tsw33, tsw34, tsw35 and tsw36), lithophysal porosities are listed in Table 9 (from DTN: SN0208T0503102.007 [160257]). For these stratigraphic units, the bulk thermal conductivities are also listed in DTN: SN0208T0503102.007 [160257]. The bulk thermal conductivities of the corresponding UZ Model layers are listed in Table 10. For further details, refer to the Scientific Notebook (Wang 2003 [161654], SN-LBNL-SCI-100-V3, pp. 69–79).

The thermal properties of the faults are developed using the averaging techniques discussed above (Francis 1997 [127326]). The UZ Model represents faults as having four layers that are defined by the major hydrogeologic units (HGU), TCw, PTn, TSw, and CHn/Cfu. For each of these units, averages are taken across all the stratigraphic subunits. For example, to obtain the matrix thermal properties of tcwf, averages were taken over Tpcr, Tpcp, Tpcpv3, and Tpcpv2. The details of the calculations can again be found in a Scientific Notebook (Wang 2003

[161654], SN-LBNL-SCI-100-V3, pp. 76–79). The calculated fault thermal properties are listed in Table 11.

The data reported in Tables 9, 10, and 11 have been compiled and submitted to the TDMS under Output - DTN: LB0210THRMLPRP.001.

Table 9. Matrix Thermal Properties for the UZ Model Layers

Model Layer	Grain Density (kg/m <sup>3</sup> )	Grain Specific Heat Capacity (J/kg-K)	Dry Thermal Conductivity (W/m-K)	Wet Thermal Conductivity (W/m-K)	Matrix Porosity (-)	Lithophysae Porosity (-)
tcw11	2514	985	1.3023	1.8039	0.1183	N/A
tcw12	2514	985	1.3023	1.8039	0.1183	N/A
tcw13	2274	1040	0.6698	0.7944	0.0457	N/A
ptn21	2288	1040	0.4890	1.0660	0.3541	N/A
ptn22	2288	1040	0.4890	1.0660	0.3541	N/A
ptn23	2288	1040	0.4890	1.0660	0.3541	N/A
ptn24	2288	1040	0.4890	1.0660	0.3541	N/A
ptn25	2288	1040	0.4890	1.0660	0.3541	N/A
ptn26	2283	1040	0.5374	0.9569	0.2513	N/A
tsw31	2274	1040	0.6698	0.7944	0.0457	N/A
tsw32	2514	985	1.3023	1.8039	0.1183	N/A
tsw33	2358	985	1.3234	1.9059	0.1425	0.123
tsw34	2466	985	1.4553	2.1276	0.1287	0.025
tsw35	2325	985	1.3998	2.0701	0.1486	0.088
tsw36	2473	985	1.5356	2.1958	0.1058	0.03
tsw37	2473	985	1.5356	2.1958	0.1058	0.03
tsw38	2274	1040	0.6698	0.7944	0.0457	N/A
tsw39	2274	1040	0.6698	0.7944	0.0457	N/A
ch1Ze	2288	1040	0.4890	1.0660	0.3541	N/A
ch1VI	2288	1040	0.4890	1.0660	0.3541	N/A
ch[2-5]V	2256	1038	0.5996	1.2708	0.3282	N/A
ch[2-5]Z	2256	1038	0.5996	1.2708	0.3282	N/A
ch6	2256	1038	0.5996	1.2708	0.3282	N/A
pp4	2103	1040	0.5375	1.1095	0.2974	N/A
pp3	2103	1040	0.5375	1.1095	0.2974	N/A
pp2	2385	1009	0.7326	1.3421	0.2331	N/A
pp1	2038	1040	0.5641	1.1302	0.2731	N/A
bf3	2106	1018	0.7570	1.3292	0.1883	N/A
bf2	2012	1040	0.5765	1.1400	0.2615	N/A
tr3	2371	1019	0.6137	1.2272	0.2799	N/A
tr2	2224	1040	0.4977	1.0778	0.3354	N/A

Output - DTN: LB0210THRMLPRP.001

Table 10. Bulk Thermal Conductivities of Repository Model Layers

Model Layer	Dry Thermal Conductivity (W/m-K)	Wet Thermal Conductivity (W/m-K)
tsw33	1.164	1.675
tsw34	1.419	2.074
tsw35	1.278	1.889
tsw36	1.49	2.13

Output - DTN: LB0210THRMLPRP.001

Table 11. Fault Thermal Properties

Major Unit	Fault Layer	Grain Density (kg/m <sup>3</sup> )	Grain Specific Heat Capacity (J/kg-K)	Dry Thermal Conductivity (W/m-K)	Wet Thermal Conductivity (W/m-K)	Matrix Porosity (-)
TCw	tcwf	2394	1011	0.8846	1.1030	0.082
PTn	ptnf	2286	1040	0.5086	1.0164	0.31
TSw	tswf	2368	1003	0.9980	1.2988	0.1026
CHn/CFu	chnf	2198	1034	0.5731	1.1706	0.295

NOTE: CFu is assigned the same property value as CHn.

Output - DTN: LB0210THRMLPRP.001

## 6.4 FAULT PROPERTIES

The UZ Model represents faults as having four layers defined by the major HGUs: TCw, PTn, TSw, and CHn/CFu. The constituent sublayers of these HGUs are shown in Table 4. Fault, fracture, and thermal properties are calculated for these four layers. Each HGU has been approximately assigned the uniform properties within faults. The reason for this consolidation is that data to characterize faults are very limited. Matrix hydraulic properties in faults, however, are assigned the same as the corresponding nonfault UZ properties.

Direct measurements of fault-specific properties were limited to air-injection tests performed in Alcoves 2, 6, and 7, which are also called the Bow Ridge fault alcove, the North Ghost Dance fault access drift, and the South Ghost Dance fault access drift, respectively. Analysis of crosshole tests run in the Bow Ridge fault alcove (LeCain 1998 [100052], p. 21) and the North Ghost Dance fault access drift (DTN: GS990883122410.002 [135230]; LeCain et al. 2000 [144612]) gave the best estimates of fracture permeability in the TCw and TSw fault layers, respectively.

All other fault properties were calculated as averages of nonfault layer. Some layers are much thicker than others, and thus the properties of those layers should be weighted more heavily when calculating the fault properties. Properties were weighted by their respective average layer thickness. Porosity was arithmetically averaged because its differences between model layers within each HGU are not significant,

$$p_a = \frac{\sum_{i=1}^n p_i L_i}{\sum_{i=1}^n L_i} \quad (\text{Eq. 42})$$

where  $p_a$  is the weighted arithmetic average property (porosity),  $n$  is the number of layers being averaged,  $p_i$  is the property for layer  $i$ , and  $L_i$  is the thickness of layer  $i$ . The fracture-matrix interface areas are also calculated using Equation 42. Permeability is more appropriately harmonically averaged because it is generally considered to be log-normally distributed (Gelhar 1993 [101388], p. 2),

$$p_h = \frac{\sum_{i=1}^n L_i}{\sum_{i=1}^n \frac{L_i}{p_i}} \quad (\text{Eq. 43})$$

where  $p_h$  is the weighted harmonic average property (permeability). Layer thickness is estimated as the average (arithmetic) layer thickness over the GFM2000 model (DTN: MO0012MWDGFM02.002 [153777]) area. Another consideration for using Equation 43 is that it is exact when the flow direction is perpendicular to interfaces between model layers. This is approximately the case for the UZ because the flow direction is mainly vertical.

In principle, a more rigorous way to estimate the fault (fracture) properties is to correlate them with geologic information specific to each fault being modeled and to individual locations within each fault, such as amount of fault offset, width of the disturbed zone, and presence of contacts with significant property changes. This alternative approach, however, requires the development of relationships between hydraulic properties and geologic information that can not be reliably estimated with available data regarding fault properties.

Fracture permeability for the TCw and TSw fault layers was given by the crosshole air-injection tests described above. Permeability for the PTn and CHn/CFu fault layers was calculated by scaling the weighted average bulk-rock fracture permeability. As with the matrix permeability, equivalent fracture permeability was calculated for all four fault layers using the weighted harmonic mean of permeabilities for the corresponding nonfault model layers. The average (geometric mean) ratio of the measured permeability to the calculated equivalent permeability for layers TCw and TSw was calculated (Ahlers 2000 [155853], pp. 124–125). This factor multiplies the calculated equivalent permeability of the PTn and CHn/CFu layers to scale them upward. This process is equivalent to the process used to scale bulk-rock matrix  $\alpha$ , which is explained in Section 6.2.

Equivalent fracture spacing, equal to the inverse of fracture frequency, can be calculated using the weighted arithmetic mean. Again, it can be shown that the weighted arithmetic mean of  $1/p_i$  is equal to the harmonic mean of  $p_i$ , so the weighted harmonic mean of frequency is used to calculate the equivalent frequency for the faults.

Fracture aperture was calculated as in Section 6.1 (using Equation 7), based on the cubic law and the fault permeabilities and frequencies.

Fault fracture porosity was determined by scaling the weighted arithmetic mean of bulk-rock fracture porosity. The scaling factor is the ratio of fault fracture aperture to mean bulk-rock fracture aperture. The mean bulk-rock fracture aperture was calculated as the weighted arithmetic average of fracture aperture.

The fracture van Genuchten  $m$  ( $m_f$ ) is taken as 0.633 as for all other fractures (see Section 6.1). The fracture van Genuchten  $\alpha$  ( $\alpha_f$ ) is calculated based on the fracture aperture, using Equation 9 as documented in Section 6.1.

The fracture-to-matrix connection area for the faults was approximated as the weighted arithmetic mean of bulk rock fracture-to-matrix connection area. The rationale for the development of fault properties is documented in a Scientific Notebook (Ahlers 2000 [155853], pp. 117–127, 145–146). Table 12 presents the calculated fault fracture properties.

Table 12. Calculated Fault Fracture Properties

Major Unit	Fault Layer	Permeability ( $m^2$ )	Porosity (-)	Frequency ( $m^{-1}$ )	$\alpha_f$ ( $Pa^{-1}$ )	$m_f$ (-)	Interface area ( $m^2/m^3$ )
TCW	tcwf	2.7E-11	2.9E-2	1.9	3.8E-3	0.633	12.9
PTn	ptnf	3.1E-12	1.1E-2	0.54	2.8E-3	0.633	1.3
TSw	tswf	1.5E-11	2.5E-2	1.7	3.2E-3	0.633	8.7
CHn/CFu	chnf	3.7E-13	1.0E-3	0.13	2.3E-3	0.633	0.46

Output-DTN: LB0207REVUZPRP.001

## 6.5 CONFIRMATION OF FRACTURE PROPERTIES

Uncertainties generally exist in the estimated rock properties. This is particularly true for the fracture properties, such as fracture van Genuchten parameters and porosity, because they are not directly measured, but indirectly estimated from other property measurements. In addition to model calibration, it is useful to confirm the estimated properties by independent methods and relevant data. In this subsection, the ESF seepage test results are used to independently determine fracture van Genuchten  $\alpha$  and porosity for confirmation purposes. The determination procedures are very different from those used in Section 6.1 of this report. This confirmation activity is also documented in a Scientific Notebook by Liu (2001 [155675], pp. 64–68).

### 6.5.1 ESF Seepage Tests

After Niche 3650 (Niche 2) in the ESF was excavated, a series of seepage tests were performed by pumping water into boreholes labeled UL, UM, and UR, located above the niche (BSC 2001 [158463], Section 6.2). Water was released into several packed-off intervals in these boreholes. Tracers were also introduced during the seepage tests. Water entering the niche was

captured, and water arrival times were recorded during the tests. Based on water seepage rates and the corresponding water release fluxes for a given test interval, a seepage threshold flux was determined (DTN: LB980901233124.003 [105592]). The threshold flux is defined as the water-release flux within a test interval at which seepage into the niche no longer occurred. The threshold water flux inferred from observations and water-arrival-time data are the primary data used for determining van Genuchten fracture  $\alpha$  ( $\alpha_f$ ) and porosity. The test sites were located at the fractured middle nonlithophysal zone of the Topopah Spring welded unit, corresponding to the UZ Model layer tsw34. A detailed discussion of the tests can be found in BSC (2001 [158463], Section 6.2).

### 6.5.2 Approach

The approach for determining van Genuchten fracture  $\alpha$  from the seepage test results is based on the theory of Philip et al. (1989 [105743]). They developed analytical solutions for water exclusion from, or entry into, cavities from downward seepage through unsaturated porous media. The considerations they used to derive their solutions are as follows (Philip et al. 1989 [105743], pp. 16–23):

First, liquid water flow is downward and steady, and the concerned porous medium is isotropic and homogeneous. To be consistent with this consideration, our analyses used the results for the seepage tests associated with fracture networks. This was because a fracture network may be conceptualized as a continuum such that the solutions developed for porous media can be approximately applied. Data in DTN: LB980901233124.003 [105592] indicated that the tests were associated with either connected fracture networks or individual vertical fractures (or small groups of vertical fractures). A study by Finsterle (2000 [151875]) indicated that the continuum approach could be used for dealing with seepage (at the same scale) in practice. However, a theoretical validation of the continuum approach for the given scale is not available and further investigation may still be needed to resolve this issue.

Second, Philip et al. (1989 [105743], pp. 16–18) considered that the flow domain is infinite in extent and flow velocity in the upstream is spatially uniform. This is because liquid water flow in a fracture continuum is largely dominated by gravity and capillary-dispersion effects are weak. Therefore, it is not unreasonable to use the theory of Philip et al. (1989 [105743]) for analyzing the localized tests for fracture networks.

Third, Philip et al. (1989. [105743], p. 18, Eq. 12) considered that there exists a functional relation between unsaturated hydraulic conductivity,  $K(\Psi)$  (m/s), and moisture potential,  $\Psi$  (m), that is exponential in nature.

$$K(\Psi) = K_0 e^{\alpha'(\Psi - \Psi_0)} \quad (\text{Eq. 44})$$

where  $K_0$  (m/s) is the hydraulic conductivity at a referential water potential  $\Psi_0$  (m), and  $\alpha'$  ( $\text{m}^{-1}$ ) is the sorptive number (corresponding to  $\alpha$  in Philip et al. 1989 [105743]). In this study, we treat  $K_0$  as the saturated hydraulic conductivity, and therefore  $\Psi_0 = 0$  by definition. The sorptive number is a constant for a homogeneous porous medium, and usefully characterizes the capillary properties of the medium in unsaturated flow (Philip et al. 1989 [105743], p. 18). This number can be used to determine van Genuchten  $\alpha$ , which will be discussed below.

According to Philip et al. (1989 [105743], pp. 19, 23), the threshold water flux,  $K_{0^*}$  (m/s), can be related to the saturated hydraulic conductivity,  $K_0$  as

$$K_{0^*} = K_0 [\mathcal{G}_{\max}(s)]^{-1} \quad (\text{Eq. 45})$$

with  $s = (1/2)\alpha' l$ , where  $l$  (m) is the radius for a circular cylindrical cavity. For the ESF seepage tests, it is the radius of the niche. Under the condition that  $s$  is large (or capillary effects are weak),  $\mathcal{G}_{\max}$  can be expressed as (Philip et al. 1989 [105743], p. 23, Eq. 83)

$$\mathcal{G}_{\max}(s) = 2s + 2 - \frac{1}{s} + \frac{1}{s^2} - \dots \quad (\text{Eq. 46})$$

Based on Equations 45 and 46 a sorptive number,  $\alpha'$ , can be estimated from known saturated conductivity and threshold flux values for a given seepage test. The estimation of sorptive number values ( $\alpha'$ ) are discussed in BSC (2001 [158463], Section 6.2) and given in the data set (DTN: LB980901233124.003 [105592]). Note that in Section 6.2 of BSC (2001 [158463]), the so-called capillary strength is the same as  $(\alpha')^{-1}$  here.

The sorptive number can be related to van Genuchten fracture  $\alpha$  ( $\alpha_f$ ) by the following curve-fitting procedure. Based on the definition of relative permeability, Equation 44 leads to a relative permeability ( $k_r$ ) relation (Liu 2001 [155675], pp. 64–68)

$$\ln(k_r) = \frac{\alpha' p_c}{\rho g} \quad (\text{Eq. 47})$$

where  $p_c$  (Pa) is the capillary pressure,  $g$  (m/s<sup>2</sup>) is the gravitational acceleration, and  $\rho$  (kg/m<sup>3</sup>) is the liquid-water density. The van Genuchten (1980 [100610], Equations 3 and 8) relationships result in

$$\ln(k_r) = -\frac{m}{2} \ln[(p^*)^n + 1] + 2 \ln\left[1 - \left(1 - \frac{1}{1 + (p^*)^n}\right)^m\right] \quad (\text{Eq. 48})$$

where  $n$  and  $m=1-1/n$  are van Genuchten parameters, and  $p^*$  is a dimensionless capillary pressure defined by

$$p^* = \alpha_f |p_c| \quad (\text{Eq. 49})$$

In terms of  $p^*$ , Equation 47 can be rewritten as

$$\ln(k_r) = -\frac{\alpha'}{\rho g \alpha_f} p^* \quad (\text{Eq. 50})$$

For a given fracture  $m$  ( $m_f$ ) value and a range of  $p^*$  values,  $\alpha' / (\rho g \alpha_f)$  can be estimated by fitting Equation 50 through a number of data points calculated from Equation 48. Since  $\alpha'$  is known, the corresponding  $\alpha_f$  ( $\text{Pa}^{-1}$ ) can be easily estimated.

In addition to determining the van Genuchten fracture  $\alpha$ , the seepage test results can be used to estimate the volumetric water content of the fracture continuum. The estimated saturated water contents provide useful information for confirming fracture properties estimated in Section 6.1 of this report.

Under the conditions that water flow is one-dimensional and the wetting front has a constant velocity, the depth of the wetting front can be determined as

$$z_p = \frac{q_s t}{(\theta_{av} - \theta_r)} \quad (\text{Eq. 51})$$

where  $z_p$  ( $m$ ) is the depth from the water supply source to the wetting front,  $t$  ( $s$ ) is the arrival time of the front at depth  $z_p$ ,  $q_s$  is the constant flux of water supplied at the source,  $\theta_r$  is the residual water content, and  $\theta_{av}$  is the average volumetric water content between the source and the wetting front. Water content is defined as volume of liquid water divided by the total rock volume. For the seepage tests,  $z_p$  and  $t$  can be considered as the distance between the source and the ceiling of the niche, and the wetting front arrival time at the ceiling, respectively. A detailed discussion of the procedures to determine water content values was given in BSC (2001 [158463], Section 6.2). Letting  $\theta_r = 0$ ,  $\theta_{av}$  can be estimated for each seepage test. The estimated  $(\theta_{av} - \theta_r)$  values are reported in DTN: LB980901233124.003 [105592]. Note that the conditions for Equation 51 to hold are approximately satisfied when the capillary effects are weak, which is the case for water flow in fractures.

Finally, it should be indicated that in the above discussion, the matrix imbibition was ignored, because for the given temporal and spatial scales of the seepage tests, the matrix imbibition is expected to be insignificant compared to the amount of water flowing through fractures.

### 6.5.3 Results and Discussion

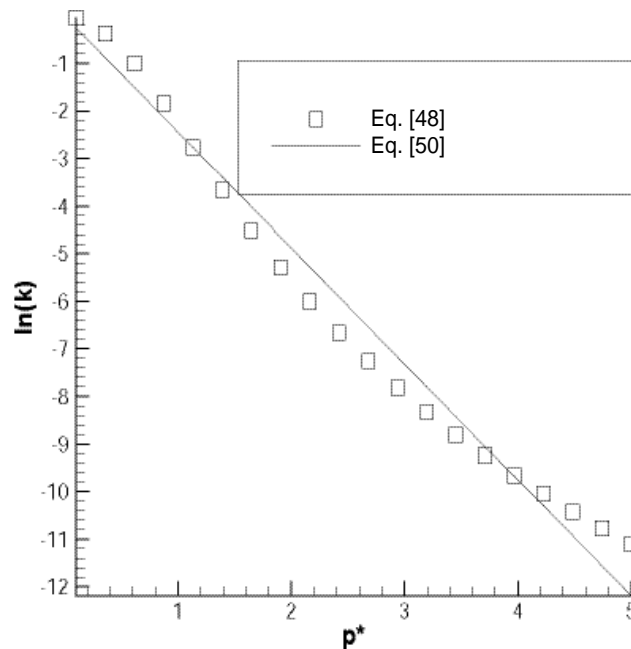
The van Genuchten fracture  $\alpha$  values estimated from the seepage test results are given in Table 13. To estimate these values, modelers applied the curve fitting procedure for  $p^* \leq 5$ , based on the following considerations. First, van Genuchten fracture  $\alpha$  is closely related to the air-entry pressure, which is mainly characterized by capillarity and relative permeability data at large saturations (or small capillary pressures). Therefore, it is appropriate to perform the curve fitting for a range of  $p^*$ , corresponding to relatively small capillary pressure values, in order to estimate the van Genuchten fracture  $\alpha$ . Second, considering a unit hydraulic head gradient condition, the water release flux at the source for a given seepage test can be considered as the unsaturated hydraulic conductivity. In this case, the ratio of the water release flux to the saturated hydraulic conductivity is an approximation of the relative permeability. The natural logs of the calculated ratio for the relevant seepage tests based on the data in DTN: LB980901233124.003 [105592] are larger than  $-5$ . In this case,  $p^* \leq 5$  results in relative permeability values that are adequate to cover this range (Figure 4). We also used  $m_f = 0.633$  for the curve fitting. The determination of this  $m$  value was given in Section 6.1 of this report. Curve fitting results are shown in Figure 4.

Table 13. Log Values of van Genuchten Fracture  $\alpha$  Estimated from the ESF Seepage Tests (Niche 3650)

Borehole (Depth(m))	Log( $\alpha_f$ ) <sup>a</sup>
Upper Left (7.01-7.32)	-3.31
Upper Middle (4.27-4.57)	-2.73
Upper Middle (5.49-5.79)	-2.90
Upper Right (4.27-4.57)	-3.10
Upper Right (4.88-5.18)	-2.69
Upper Right (5.49-5.79)	-4.23
average	-3.16

NOTE: <sup>a</sup> Log( $\alpha_f$ ) is calculated using  $\alpha'$  data (DTN: LB980901233124.003 [105592]).

Table 13 shows that the estimated fracture  $\alpha$  value varies for different test locations owing to heterogeneities. However, the average log( $\alpha_f$ ) value is  $-3.16$ , which is very close to the log( $\alpha_f$ ) value of  $-3.18$ , determined from air-permeability data for UZ Model layer tsw34 (Table 7). As indicated before, the test sites are located in zones represented by the model layer tsw34 (Table 7). It is encouraging that independent approaches used to estimate the fracture  $\alpha$ , based on different data sets, lead to similar fracture  $\alpha$  values. This convergence indicates that the approach used to estimate fracture  $\alpha$  based on air-permeability data and the resultant fracture  $\alpha$  values, reported in Section 6.1 of this report, are reasonable.



Source: Liu (2001 [155675], pp. 64–68)

Figure 4. Graph of Fitting of Equation 48 to Equation 50 using a Number of Data Points for  $p^* < 5$

The data from DTNs: LB980901233124.003 [105592] and DTN: LB0110LIQR0015.001 [156907] include values for the fracture water-content change in the seepage tests. These data were collected from Niches 3650 and 4788, which are located in the same geological unit. As discussed before, this change is equal to the average volumetric water content when assuming zero residual water content. Herein, we are interested in the water content values under the saturated condition or when the liquid-water release flux at the source is close to the saturated hydraulic conductivity (or water flux is the largest among those used in the tests for a given testing interval). In these cases, the fracture networks are highly saturated, and therefore, the water-content values are good approximations of the corresponding fracture porosities. Several water-content values of this kind were given in DTNs: LB980901233124.003 [105592] and LB0110LIQR0015.001 [156907]. They are 0.0101, 0.0242, 0.0150, 0.0124, 0.0024, 0.0200, 0.0489, and 0.0092, respectively, and the average value is 0.018. The fracture porosity for the model layer tsw34, determined in Section 6.1, is about 0.0085, in the same order of magnitude with this average value.

## 6.6 ACTIVE FRACTURE MODEL (AFM)

In a dual-continuum approach, the treatment of fracture-matrix interaction is important for accurate modeling flow and transport. This subsection discusses the AFM used in the UZ Flow and Transport Model. The validation of this conceptual model is given in Section 7.

### 6.6.1 Active Fracture Concept

Although a number of mechanisms exist, fingering flow at a fracture-network scale is considered to be a key mechanism for limiting fracture-matrix interaction, more important than that at a single-fracture scale. We expect that for unsaturated fractured rocks, the water flow pattern should be characterized by significant preferential (fingering) flow at a fracture-network scale, on account of the large nonlinearity involved in an unsaturated system and heterogeneities of fracture structure at different scales. The AFM concept is based on the reasoning that because of fingering flow, only a portion of fractures in a connected, unsaturated fracture network contribute to liquid water flow, while others are simply bypassed. The portions of the connected fractures that actively conduct water are called active fractures. We hypothesize that the number of active fractures in the Yucca Mountain UZ is small compared with the total number of connected fractures. Hence, active fractures, rather than total connected fractures, should be used in numerical models. We further hypothesize that the number of active fractures within a gridblock is large, such that a continuum approach is still valid for describing fracture flow. These hypotheses are consistent with the consideration that fractures permitting flow in the UZ are many and highly dispersed.

To use the AFM concept to model flow and transport in fractures, we treat active fractures as part of a “homogeneous” fracture continuum for a given gridblock. Note that differences exist between the AFM and the conventional, capillary-equilibrium-based, fracture water distribution model. The latter assumes that liquid water first occupies fractures with small apertures, and then occupies fractures with relatively large apertures as water potential (or water saturation) increases. In contrast, the AFM presumes gravity-dominated, nonequilibrium, preferential liquid water flow in fractures, which is expected to be similar to fingering flow in unsaturated porous

media. A liquid finger can bypass a large portion of a porous medium, which does not necessarily correspond to large pores.

Flow and transport conditions and fractured rock properties should determine the fraction of active fractures in a connected fracture network,  $f_a$ . An expression for  $f_a$  must satisfy the following conditions: all connected fractures are active ( $f_a = 1$ ) if the system is fully liquid saturated; all fractures are inactive ( $f_a = 0$ ) if the system is at residual saturation; and  $f_a$  should be related to water flux in fractures. It is generally believed that more fractures are conducive to a larger water flux. The water flux in fractures is considered to be mainly dependent on fracture saturation, because fracture water flow is gravity-dominated. A simple expression for  $f_a(-)$ , which meets these conditions and includes one parameter only, is a power function of effective water saturation in connected fractures,  $S_e(-)$ .

$$f_a = S_e^\gamma \quad (\text{Eq. 52})$$

where  $\gamma(-)$  is a positive constant depending on properties of the corresponding fracture network, and the effective water saturation in connected fractures is given by

$$S_e = \frac{S_f - S_r}{1 - S_r} \quad (\text{Eq. 53})$$

where  $S_f(-)$  is the water saturation of all connected fractures and  $S_r$  is the residual fracture saturation. Note that the saturated saturation is set to 1 and “(-)” means “dimensionless” here. In this study, Equation 52 is used to determine the fraction of active fractures because it is physically reasonable and mathematically simple. As discussed below, Equation 52 allows us to treat all the ramifications of the active fracture hypothesis (modified fracture capillarity, relative permeability, and fracture-matrix interaction reduction) in an integrated manner. The simple Equation 52 is considered as a first-order approximation. As will be shown in Section 7, it is consistent with a fractal flow pattern in a fracture network.

### 6.6.2 Constitutive Relationships

Note that only the active fracture continuum, a portion of the total fracture continuum, contributes to flow and transport in fractures and fracture-matrix interaction. Therefore, fracture hydraulic properties should be defined for active fractures. The effective water saturation of active fractures,  $S_{ae}(-)$ , is related to the effective water saturation in connected fractures,  $S_e$ , by

$$S_{ae} = \frac{S_e}{f_a} = S_e^{1-\gamma} \quad (\text{Eq. 54})$$

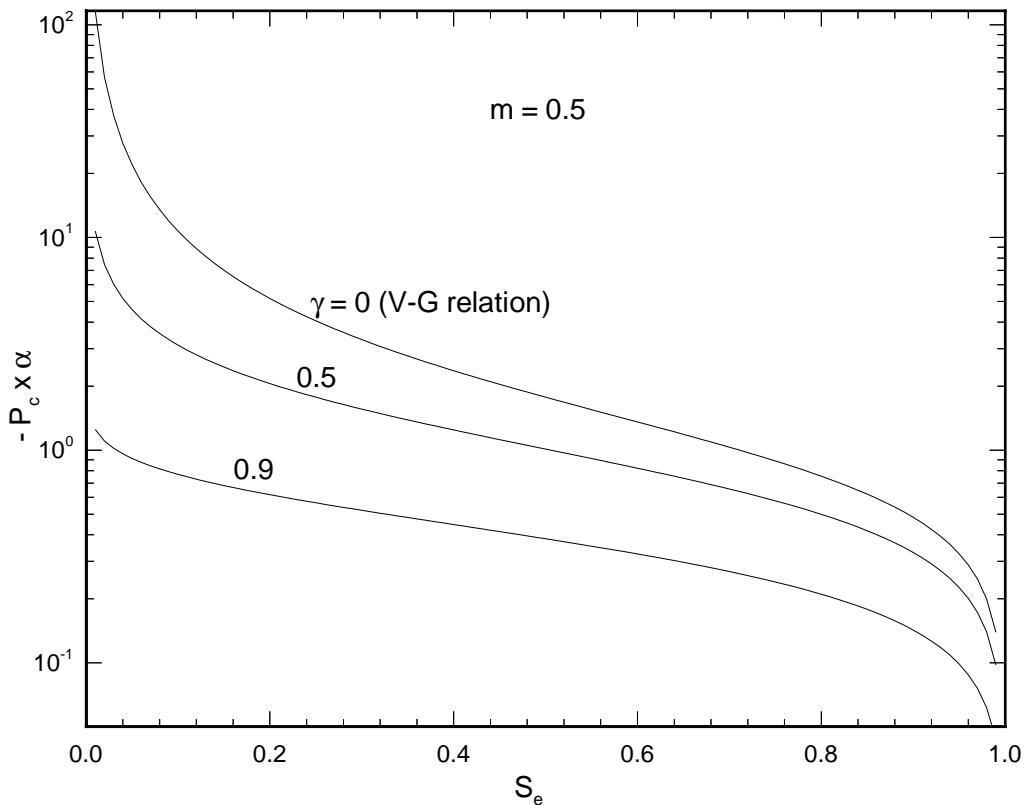
Because  $S_{ae} \leq 1$ ,  $\gamma$  should be in a range between 0 and 1. The effective water saturation of active fractures is related to the actual water saturation in active fractures,  $S_a$ , by

$$S_{ae} = \frac{S_a - S_r}{1 - S_r} \quad (\text{Eq. 55})$$

If all connected fractures are considered to be active in conducting water, as assumed in previous studies, the water capillary pressure for the fracture continuum may be described by the well-known van Genuchten relation (Equation 8).

In AFM, however, the van Genuchten capillary pressure relation is considered to be relevant for the active fracture continuum, rather than for the whole fracture continuum. The capillary pressure for active fractures is determined by replacing  $S_e$  in Equation 8 with  $S_{ae}$ ,

$$P_c(S_e) = \frac{1}{\alpha} [S_{ae}^{-1/m} - 1]^{1/n} = \frac{1}{\alpha} [S_e^{(\gamma-1)/m} - 1]^{1/n} \tag{Eq. 56}$$



Source: Liu et al. 1998 [105729], p. 2636, Figure 2

Figure 5. Capillary Pressure Curves of Fracture Continuum for  $\gamma = 0, 0.5,$  and  $0.9$

Equation 56 should be used to simulate water flow in the fracture continuum. Figure 5 shows fracture capillary pressure curves for several  $\gamma$  values. For a given effective water saturation in connected fractures, a larger  $\gamma$  value corresponds to a larger effective water saturation in active fractures, and therefore to a lower absolute value for capillary pressure.

The liquid-phase relative permeability for the active fracture continuum,  $k_{ar} (-)$ , is directly determined by the effective water saturation of active fractures. However, as only a portion of the fractures are active, the relative permeability of the entire fracture continuum,  $k_r (-)$  should be the relative permeability of active fractures multiplied by  $f_a$ , or

$$k_r = f_a k_{ar} = S_e^\gamma k_{ar} \quad (\text{Eq. 57})$$

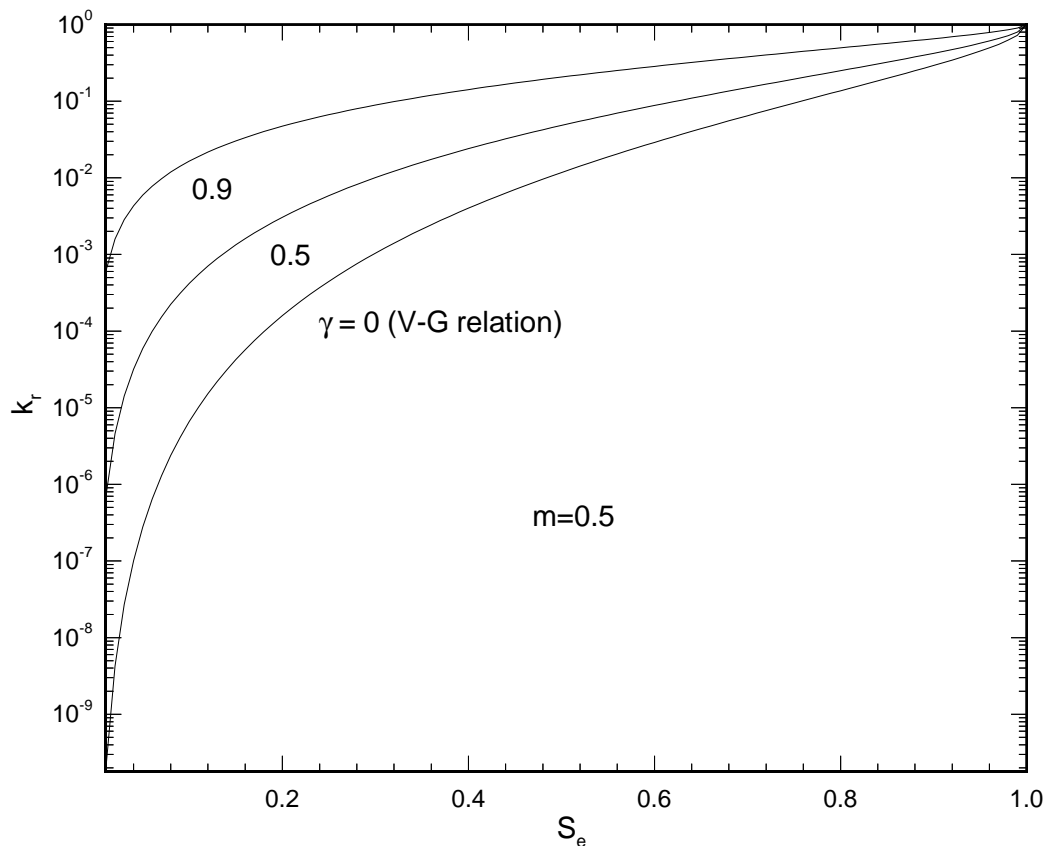
where  $k_{ar}$  can be given by the following van Genuchten permeability relation:

$$k_{ar} = S_{ae}^{1/2} [1 - \{1 - S_{ae}^{1/m}\}^m]^2 = S_e^{(1-\gamma)/2} [1 - \{1 - S_e^{(1-\gamma)/m}\}^m]^2 \quad (\text{Eq. 58})$$

Combining Equations (57) and (58) yields

$$k_r = S_e^{(1+\gamma)/2} [1 - \{1 - S_e^{(1-\gamma)/m}\}^m]^2 \quad (\text{Eq. 59})$$

Relative permeability ( $k_r$ ) curves are shown in Figure 6 for several  $\gamma$  values. In general, the relative permeability ( $k_r$ ) is affected by  $\gamma$  in a complicated manner for a given  $S_e$ . A larger  $\gamma$  value, resulting in a higher effective water saturation in active fractures ( $S_{ae}$ ), gives rise to a larger value of  $k_{ar}$ . On the other hand, a larger  $\gamma$  value corresponds to a smaller value of  $f_a$ . Because the former effect is dominant, a larger  $\gamma$  value gives a larger relative permeability for a given effective water saturation of the fracture continuum, as indicated in Figure 6.



Source: Liu et al. 1998 [105729], p. 2637, Figure 3

Figure 6. Relative Permeability Curves of Fracture Continuum for  $\gamma = 0, 0.5, \text{ and } 0.9$

In the AFM, the fracture-matrix interface area reduction factor results from three aspects. First, the average interface area between mobile water (saturated liquid water segments) in an active

fracture and the surrounding matrix is smaller than the geometric interface area. Second, the number of active fractures is smaller than that of connected fractures. Conventionally, all the connected fractures are considered to contribute to fracture-matrix interaction. Third, average active fracture spacing is much larger than that for connected fractures. Under the quasi-steady-state condition, flow and transport between fractures and surrounding matrix is inversely proportional to the corresponding fracture spacing. Based on these considerations and Equation 53, Liu et al. (1998 [105729], pp. 2636–2638) derived an expression for the reduction factor:

$$R \cong S_e^{1+\gamma} \quad (\text{Eq. 60})$$

Note that the AFM uses a combination of the volume-averaged method and a simple filter to deal with fracture flow and transport. Inactive fractures are filtered out in modeling fracture-matrix interaction, flow, and transport in the fracture continuum. We believe that filtering could add the capability to continuum approaches to capture dispersed fingering flow at a subgrid scale. Note that the  $\gamma$  factor may be interpreted as a measure of the “activity” of connected fractures. Generally speaking, a smaller  $\gamma$  value corresponds to a larger number of active fractures in a connected fracture network. For example,  $\gamma = 0$  results in  $f_a = 1$  in Equation 52, corresponding to all connected fractures being active. On the other hand,  $\gamma = 1$  corresponds to zero fracture capillary pressure (Equation 56), indicating that all active fractures are saturated. In the latter case, the fraction of active fractures is very small for small percolation fluxes, because relatively high fracture permeabilities measured at Yucca Mountain allow most of the water to flow through only a few fractures.

## 6.7 AFM AND A FRACTAL-BASED FLOW MODEL

### 6.7.1 Evidence of Fractal Flow- Patterns in Unsaturated or Multiphase Flow Systems

Fractals have been shown to be a common language for describing many different natural phenomena (Mandelbrot 1983 [160848]). A vast literature exists for discussing the validity of the fractal concept in a great number of fields. Many studies recently show that complex flow patterns in unsaturated or multiphase flow systems can be described by fractals. For example, viscous fingering in porous media has been experimentally shown to be fractal (Feder 1988 [160844], Chapter 4). (The problem of viscous fingering in porous media is of central importance in oil recovery.) Flury and Flühler (1995 [160845]) fitted a diffusion-limited-aggregation (DLA) model for solute transport in one of three field plots under unsaturated conditions, and then predicted reasonably well for the other two. A detailed description of DLA is given in Flury and Flühler (1995 [160845]). The DLA generates fractal patterns (Feder 1988 [160844], pp. 53–56). Persson et al. (2001 [160840]) further confirms the finding of Flury and Flühler (1995 [160845]) by showing that flow patterns resulting from an unsaturated field site display a fractal resemblance. Glass (1993 [160751]) demonstrated that unsaturated flow patterns in individual fractures can be reasonably modeled by a percolation-based model. Percolation-based models generate fractal patterns (Feder 1988 [160844], Section 7.8; Stauffer and Aharony 1991 [160846], Section 6.6). Detailed experimental studies on unsaturated flow patterns in natural fracture networks are still lacking in the literature.

Unsaturated flow patterns in a fracture network are expected to be (at least approximately) fractal also. This is supported by fracture coating data from the unsaturated zone of Yucca Mountain.

As will be discussed in Section 6.7.2, fracture coating is generally a signature of water flow paths. Detailed line survey data for coated fracture is available from DTN: GS980308315215.008 [107355]. Since Tptpmn (tsw34) unit has the largest number of survey intervals, data from this unit are analyzed using the box counting method that will be discussed in Section 7.2.2. The locations of the coated fractures along the survey line form a set of points in a one-dimensional space. For a given box size (length of a segment)  $l$ , there are  $30/l$  small boxes (or segments) for a given survey interval that is 30 m long.  $N$  in this subsection denotes total numbers of boxes that cover at least one location of the coated fractures (along the survey line) for all the survey intervals. The determination of  $N$  as a function of  $l$  is given in Attachment II. Figure 7 shows that the observed  $N$  values as a function of  $l$  can be fitted by a power function with a power of  $-0.5$  that corresponds to a fractal dimension of 0.5 for the set of points. A more detailed discussion of fractal dimension will be given in Section 6.7.2. This indicates that coated fractures may result from a fractal flow pattern in the corresponding fracture network. Note that for a given spatial pattern, fractal dimensions are different for different Euclidean dimensions of a space. The curve fitting is performed using Tecplot.

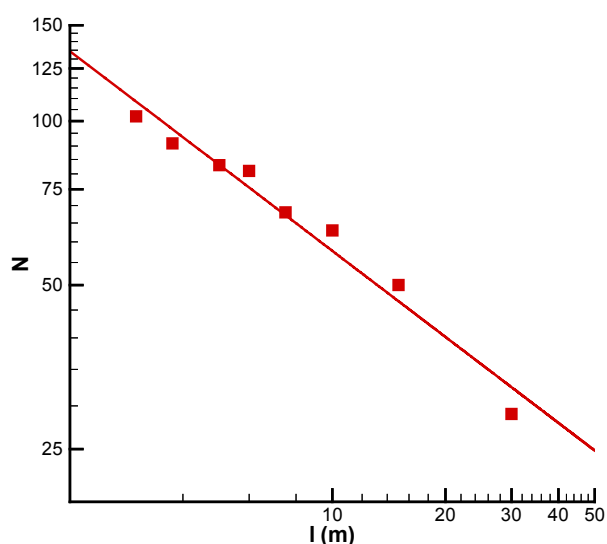


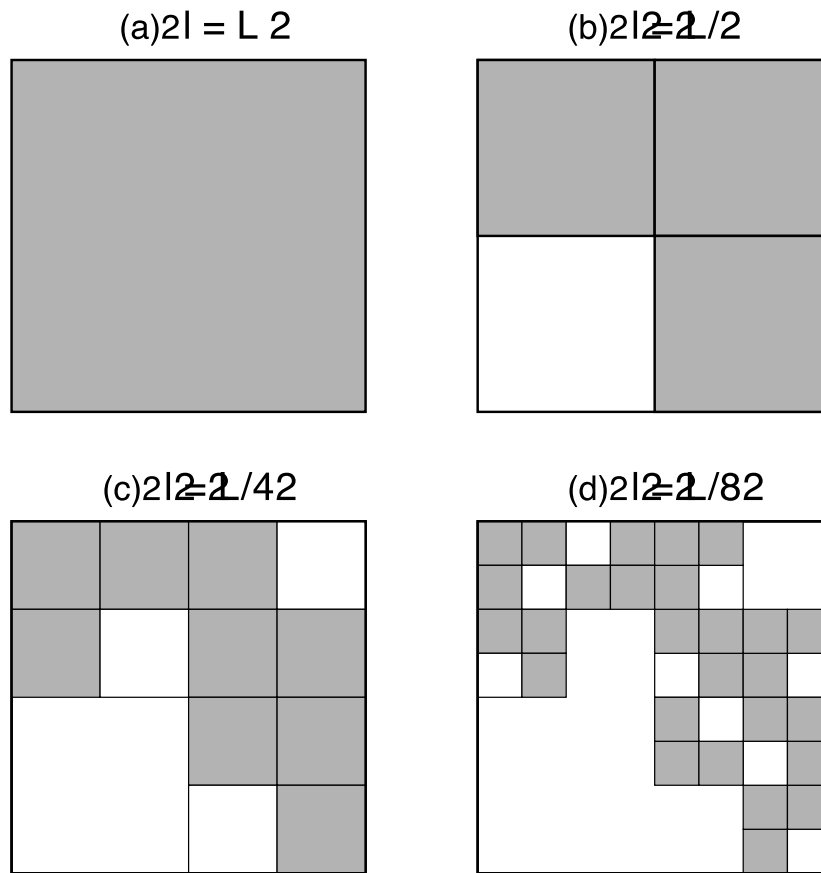
Figure 7. Relation between  $N$  and  $l$  (Attachment II). The data points correspond to observed values for the Tptpmn unit.

## 6.7.2 Fractal Dimension

A fractal pattern is characterized by the fractal dimension ( $d_f$ ) that is generally noninteger and less than the corresponding Euclidean dimension of a space,  $D$ . There are different kinds of definitions for fractal dimension (Feder 1988 [160844], Section 2.3). The most straightforward definition is based on “box counting.” In this case, the fractal dimension is determined from the following equation by counting the number ( $N$ ) of “boxes” (e.g., square and cubic for two-dimensional and three-dimensional problems, respectively), needed to cover a spatial pattern, as a function of the box size ( $l$ ) (Feder 1988 [160844], pp. 14–15):

$$N(l) = \left(\frac{L}{l}\right)^{d_f} \tag{Eq. 61}$$

where  $L$  refers to the size of whole spatial domain under consideration. Figure 8 shows a box-counting procedure for a spatial pattern with  $d_f = 1.6$  in a two-dimensional domain with size  $L$  (Yamamoto et al. 1993 [160843], Figure 3).



AT03-002

Figure 8. Schematic Showing Demonstration of “Box” Counting Procedure for Several Box Sizes, With the Shaded Areas Containing Saturation and Active Flow

Obviously, if a spatial pattern is uniformly distributed in space, the fractal dimension will be identical to the corresponding Euclidean dimension. In this case, the box number,  $N^*$ , and the box size  $l$  have the following relation

$$N^*(l) = \left(\frac{L}{l}\right)^D \tag{Eq. 62}$$

### 6.7.3 Consistency of the AFM and a Fractal Flow Pattern

Consider Figure 8a to be a gridblock containing a fracture network and the corresponding flow pattern in the fracture network to be fractal. In this case, only a portion of the medium within a gridblock contributes to water flow (Figure 8). This is conceptually consistent with the AFM (Liu et al. 1998 [105729]). Note that in Figure 8, a box is shaded if it covers one or more fractures (or fracture segments) that conduct water. For simplicity, further consider that fractures are randomly distributed in space and thus the dimension for water saturation distribution is the corresponding Euclidean dimension when all the connected fractures actively conduct water. Combining Equations 61 and 62 gives

$$[N(l)]^{1/df} = [N^*(l)]^{1/D} \quad (\text{Eq. 63})$$

The average water saturation ( $S$ ) for the whole gridblock (Figure 8a) is determined as

$$S = \frac{V}{l^D \phi N^*(l)} \quad (\text{Eq. 64})$$

where  $V$  is the total water volume (excluding residual water) in fractures within the gridblock (Figure 8a), and  $\phi$  is fracture porosity. Similarly, the average water saturation ( $S_b$ ) for shaded boxes with a size of  $l$  is given as

$$S_b = \frac{V}{l^D \phi N(l)} \quad (\text{Eq. 65})$$

From Figure 8, it is obvious that there exists a box size  $l_1 < L$  satisfying:

$$\frac{V}{l_1^D \phi} = 1 \quad (\text{Eq. 66})$$

Based on Equations 63–66, the average saturation for shaded boxes with a size of  $l_1$ ,  $S_{b1}$ , can be expressed by

$$S_{b1} = S \frac{df}{D} \quad (\text{Eq. 67})$$

Because a fractal is similar at different scales, the procedure for deriving Equation 67 from a grid-block with size  $L$  can be applied to shaded boxes with a smaller size  $l_1$ . In this case, for a given box size smaller than  $l_1$ , the number of shaded boxes will be an averaged number for those within the relatively large shaded boxes with a size of  $l_1$ . Again, one can find a box size  $l_2 < l_1$  to obtain a saturation relation:

$$S_{b2} = (S_{b1}) \frac{df}{D} = S \left( \frac{df}{D} \right)^2 \quad (\text{Eq. 68})$$

The procedure to obtain Equation 68 can be continued until it reaches an iteration level  $n^*$  at which all the shaded boxes with a size of  $l_n$  cover active fractures only. The resultant average saturation for these shaded boxes is

$$S_{bn} = (S) \left( \frac{d_f}{D} \right)^{n^*} \quad (\text{Eq. 69})$$

By definition of active fractures,  $S_{bn}$  should be equivalent to the effective saturation of active fractures. It is remarkable that Equation 69 is similar to Equation 52, obtained from a key hypothesis of the AFM that the fraction of active fractures in an unsaturated fracture network is a power function of the average effective saturation of the network. Comparing these two equations yields:

$$\gamma = 1 - \left( \frac{d_f}{D} \right)^{n^*} \quad (\text{Eq. 70})$$

Equation 70 provides the first theoretical relation between the parameter  $\gamma$  and the fractal dimension for a fractal flow system, while  $\gamma$  was initially developed as an empirical parameter (Liu et al. 1998 [105729]). Therefore, the AFM essentially captures fractional flow behavior at the subgridblock scale ( $d_f < D$ ), whereas traditional continuum approaches assume a uniform flow pattern (or effective-saturation distribution) at that scale (corresponding to  $d_f = D$  or  $\gamma = 0$ ). In other words, the AFM can be used for simulating fractal flow behavior in an unsaturated fracture network that cannot be handled by the traditional continuum approach.

Equation 70 implies that in the fractal flow model,  $\gamma$  is not a constant, but a function of saturation, because both iteration level  $n^*$  and  $d_f$  may be dependent on water saturation for a given fracture network. However, a constant  $\gamma$  is a reasonable treatment at least for a limited range of water saturations (or flow conditions), which is the case for the Yucca Mountain UZ where fracture saturation is typically less than 10% under ambient conditions. It is not totally clear how  $\gamma$  depends on the other hydraulic parameters for a large range of water saturations. Experimental evidence seems to indicate that  $\gamma$  is a weak function of saturation (at least for porous media), which will be discussed below. It is obvious from the derivation of Equation 70 that the fractal flow concept and Equation 70 can be applied to porous media also, as long as fingering flow patterns in them are fractals. Therefore, results from porous media can be used to conceptually evaluate the relation between  $\gamma$  and water saturation for unsaturated fracture networks.

Based on laboratory experimental observations collected by applying water at the top of the corresponding porous media, Wang et al. (1998 [155770], pp. 2188–2189) reported a relation between flow conditions and a parameter,  $F$ , defined as the ratio of horizontal cross-sectional area occupied by fingers to the total cross-sectional area.  $F$  corresponds to  $f_a$ , defined as the portion of active fractures in a fracture network (Liu et al. 1998 [105729]). Wang et al. (1998 [155770], pp. 2188–2189) related  $F$  to the ratio of average water flux through the whole cross-sectional area,  $q$ , to saturated hydraulic conductivity of the porous medium,  $K_s$ , by

$$F \approx \left( \frac{q}{K_s} \right)^{1/2} \quad (\text{Eq. 71})$$

for  $q/K_s = 0.4 - 1.0$ . By definition, the average water flux within fingers ( $q_F$ ) can be related to  $q$  by

$$q_F = \frac{q}{F} \quad (\text{Eq. 72})$$

and the average water saturation of fingers,  $S_F$ , can be related to the average water saturation for the whole cross-section area,  $S_e$ , by

$$S_F = \frac{S_e}{F} \quad (\text{Eq. 73})$$

It is expected that flow within a gravitational finger is gravity dominated. In this case:

$$\frac{q_F}{K_s} = k_r = S_F^{\beta^*} \quad (\text{Eq. 74})$$

Equation 74 uses the Brooks-Corey (Brooks and Corey 1964 [156915]) model for describing relative permeability ( $k_r$ )–saturation relationship.  $\beta^*$  is a constant. Combining Equation 71 to 74 yields

$$F = (S_e)^{\frac{\beta^*}{1+\beta^*}} \quad (\text{Eq. 75})$$

Comparing the above equation with Equation 51 (Liu et al. 1998 [105729], Equation 1) gives

$$\gamma = \frac{\beta^*}{1+\beta^*} \quad (\text{Eq. 76})$$

Therefore,  $\gamma$  is a constant under certain conditions in porous media. Consequently, it is expected that  $\gamma$  should be a weak function of saturation for unsaturated fracture networks if fingering flow patterns in a porous medium are considered to be an analog of flow patterns in the networks.

Note that Equation 76 cannot be directly used for estimating  $\gamma$  values for fracture networks (in the AFM) because detailed flow mechanisms are different for unsaturated fractured rock and porous media. It also needs to be emphasized that Equation 76 is valid for porous media under a condition of  $q/K_s = 0.4 - 1.0$  (Wang et al. 1998 [155770], pp. 2188–2189). The relation between  $\gamma$  and other hydraulic properties has not been established for a fracture network.

## 6.8 COMPARISON WITH A FILM-FLOW MODEL

Film flow on fracture surfaces may be an important mechanism for fast flow in unsaturated fractured rocks (Tokunaga and Wan 1997 [139195]), although the importance of the film flow in the UZ is still an issue of debate (Pruess 1999 [104250]). As an alternative conceptual model for unsaturated flow in fractures, a model assuming pure film flow within unsaturated fractures is developed to compare with the AFM. The major objective of this comparison is to demonstrate that fast flow behavior caused by film flow is already essentially captured by the current version of the AFM.

### 6.8.1 Film Flow Model

Tokunaga et al. (2000 [152914], pp. 1743–1744) both conceptually and experimentally demonstrated similarities between film flow on rough fracture surfaces and unsaturated flow in porous media. They also found that measured film thickness-potential relation data could be fitted very well by a power function, which may be related to unsaturated flow in porous media with fractal pore-size distributions (Tokunaga et al. 2000 [152914], p. 1743).

Constitutive relationships for porous media with fractal pore-size distributions have been extensively studied. The most commonly used constitutive-relationship model for these porous media is the Brooks-Corey model, although this model was not initially developed based on fractal concepts (Brooks and Corey 1964 [156915]). The Brooks-Corey model (Liu and Bodvarsson 2001 [160110]) can be expressed by

$$S_e = |P_c / P_d|^{-\lambda} \quad (\text{Eq. 77a})$$

$$k_r = \tau S_e^{(1 + \frac{2}{\lambda})} \quad (\text{Eq. 77b})$$

$$\tau = S_e^2 \quad (\text{Eq. 77c})$$

where  $P_c$  (Pa) is the capillary pressure,  $P_d$  (Pa) is the air entry pressure,  $\lambda$  (-) is a dimensionless index of pore size distribution,  $k_r$  (-) is the relative permeability,  $\tau$  (-) is the tortuosity factor, and  $S_e$  (-) is the effective saturation. Note that Equation 77a is valid when absolute values of  $P_c$  are larger than the absolute value of  $P_d$ .

Film flow is closely related to fracture surface roughness, which has also been studied extensively (National Research Council 1996 [139151]). It has been found that the surface topographies for fractures could be represented in terms of fractal geometry. Although an equivalent “pore-size distribution” for a fracture surface has not been defined, it is conceptually reasonable to hypothesize that film flow on a fractal fracture surface is similar to an unsaturated water flow process in a porous medium with fractal pore-size distribution. Based on this hypothesis, the Brook-Corey model can be adopted to develop a constitutive-relationship model for film flow. Considering average film thickness,  $f$  ( $\mu\text{m}$ ), and film transmissivity,  $T$  ( $\text{m}^2/\text{s}$ ), to be analogues of effective water saturation and hydraulic conductivity (in the model of Brooks and Corey 1964 [156915]), respectively, for a porous medium, one can obtain

$$\frac{f}{f_{ref}} = \frac{P_c}{P_{ref}}^{-\lambda} \quad (\text{Eq. 78a})$$

$$\frac{T}{T_{ref}} = \left( \frac{f}{f_{ref}} \right)^{(\eta^* + 1 + \frac{2}{\lambda})} \quad (\text{Eq. 78b})$$

$$\tau \propto f^{\eta^*} \quad (\text{Eq. 78c})$$

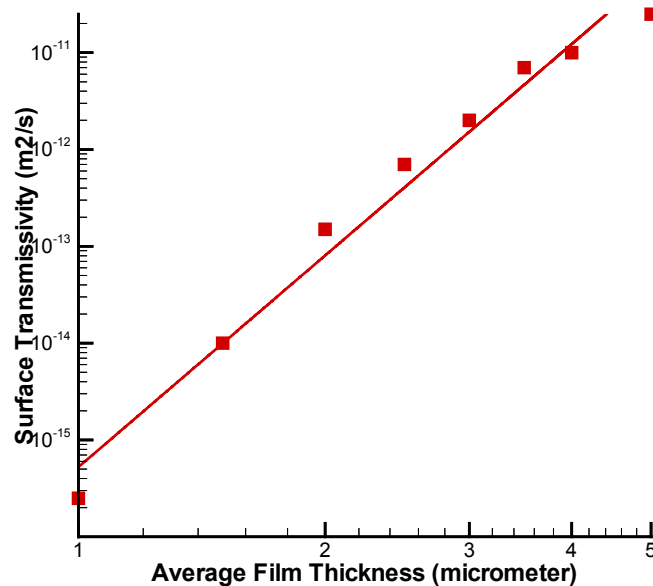
where  $f_{ref}$  ( $\mu\text{m}$ ) and  $T_{ref}$  ( $\text{m}^2/\text{s}$ ) are average film thickness and film transmissivity, respectively, for a reference capillary pressure  $P_{ref}$  (Pa), and  $\eta^*$  (-) is an empirical constant. Note that upper limits for  $f$  and  $T$ , unlike their counterparts for porous media, cannot be defined for unbounded fracture surfaces (Tokunaga et al. 2000 [152914]). Here,  $\lambda$  is considered to be a parameter characterizing the geometry of the fracture surface. Since film flow is essentially two-dimensional and pore-scale water flow in a porous medium is essentially three-dimensional, different tortuosity factors are expected for the two different cases.

Experimental observations of Tokunaga and Wan (1997 [139195]) and Tokunaga et al. (2000 [152914]) are used to verify the proposed constitutive-relationship model for film flow. Specifically, we examine whether Equation 78 could match the data. Note that the two data sets are measured for very different fracture surfaces, corresponding to a natural fracture surface of Bishop Tuff (Tokunaga and Wan 1997 [139195], p. 1298) and an artificially roughened surface (Tokunaga et al. 2000 [152914], p. 1740), respectively. Comparisons with these two data sets provide a unique opportunity to examine the validity (or robustness) of the proposed model under different conditions.

Tokunaga et al. (2000 [152914], p. 1743, Figure 6) showed that the measured film thickness—potential relation data could be fitted by a power function corresponding to  $\lambda = 0.37$  in Equation 78a. The curve fitting is performed using Tecplot for all the relevant figures in this subsection. Figure 9 shows a match of Equation 78b with the surface transmissivity—film thickness relation (Attachment I of this report) of Tokunaga et al. (2000 [152914]), which was derived from their measurements, indicating that the relation can be represented by a power function with a power value of 6.91. Using  $\lambda = 0.37$  and the power value of 6.91, we obtain  $\eta^* = 0.50$  from Equation 78b. Figure 10 shows matches of Equations 78a and 78b with the data of Tokunaga and Wan (1997 [139195]), again indicating that the data are very well represented by power functions. The resultant  $\lambda$  and  $\eta^*$  values are 1.36 and -1, respectively. Different  $\lambda$  values are obtained for the two data sets, because of the differences between the corresponding fracture surfaces, as previously mentioned. Considerably different  $\eta^*$  values are also obtained for the two surfaces as a potential result of different ranges of average film thickness involved in the two data sets (Figures 9 and 10). Further examination of the relation from Tokunaga et al. (2000 [152914]) (Figure 9) seems to indicate that it can be more accurately represented by different power functions for different thickness ranges. For example, Figure 11 shows a match of Equation 78b to the data of Tokunaga et al. (2000 [152914]) that exclude measurements below the thickness of 2  $\mu\text{m}$ , as compared with the match in Figure 9. The resultant power value is 5.67, corresponding to  $\eta^* = -0.74$  (based on Equation 78b and  $\lambda = 0.37$  given by Tokunaga et al. (2000 [152914])).

This is generally consistent with  $\eta^* = -1$  for the data of Tokunaga and Wan (1997 [139195]) (Figure 10), considering that their data involve larger values of average film thickness than those reported by Tokunaga et al. (2000 [152914]).

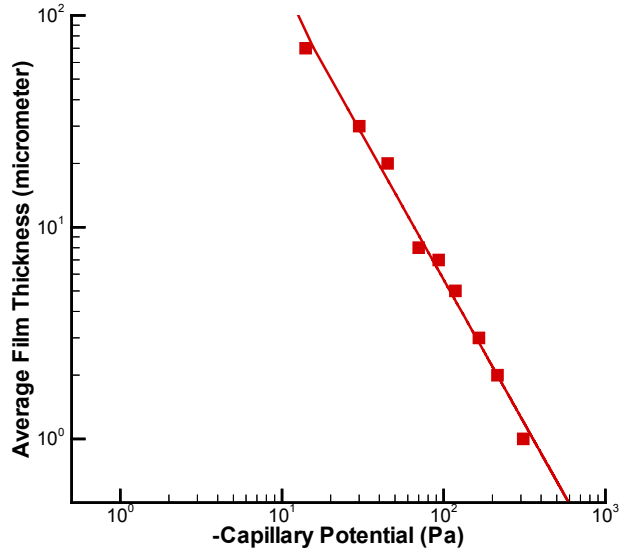
Theoretically,  $\eta^*$  should be positive because a tortuosity factor should be smaller than one (Brooks and Corey 1964 [156915]). The negative  $\eta^*$  value results from the empirical nature of Equations 79 and 78. A similar situation was also reported for several unsaturated porous media (Schaap and Leij 2000 [160841]). Based on the above analyses,  $\eta^* = -1$  seems to be reasonable for film flow with an average film thickness larger than 2  $\mu\text{m}$ . In summary, while the proposed model may need to be further evaluated using more data sets, the excellent agreement between calculation results and experimental observations of Tokunaga and Wan (1997 [139195]) and Tokunaga et al. (2000 [152914]) supports the usefulness of the model for describing film flow in unsaturated fractures.



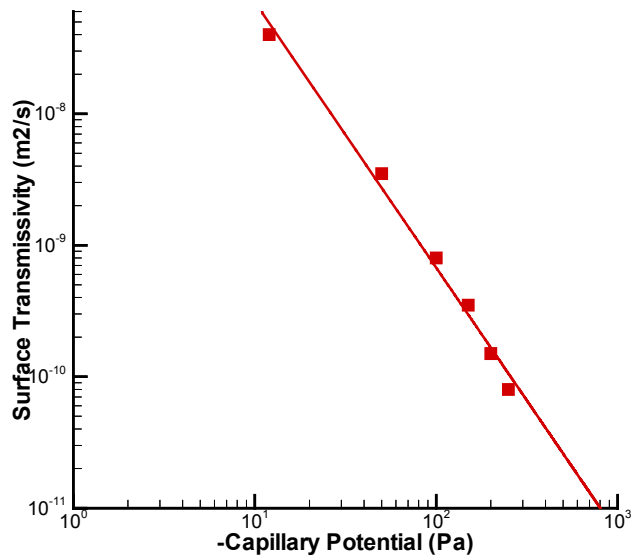
NOTE: Squares correspond to the surface transmissivity-film thickness relation (Attachment I) obtained from Figure 9 of Tokunaga et al. (2000 [152914])

Figure 9. Match of Equation 78b to Surface Transmissivity-Film Thickness Measurements

(a)

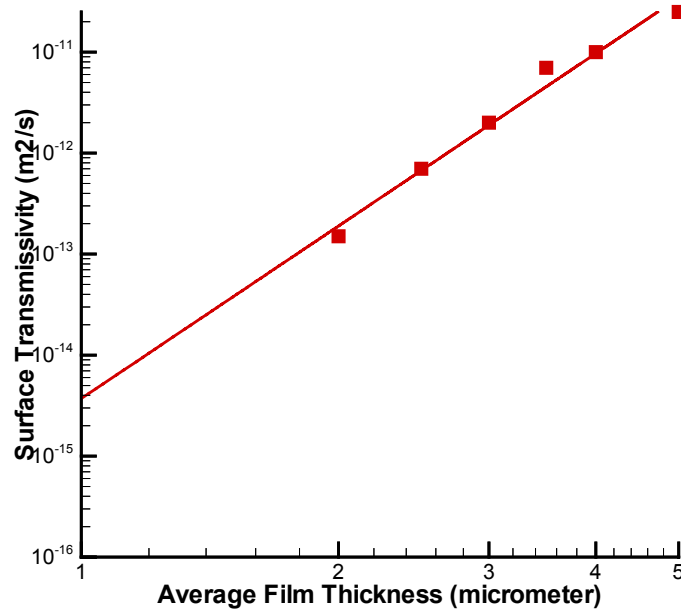


(b)



NOTE: Squares correspond to the measurements (Attachment I). (a) potential measurements given in Figure 7 of Tokunaga and Wan (1997 [139195]); (b) potential measurements given in Figure 6 of Tokunaga and Wan (1997 [139195]).

Figure 10. Matches of Equation 78 to (a) Film Thickness and (b) Surface Transmissivity-Film Thickness



NOTE: Squares correspond to the surface transmissivity-film thickness relation (Attachment I) obtained from Figure 9 of Tokunaga et al. (2000 [152914]) that exclude points below the thickness of 2  $\mu\text{m}$ , as compared with the match in Figure 9.

Figure 11. Match of Equation 78b to Surface Transmissivity-Film Thickness Measurements

Assuming that film flow only occurs in unsaturated fractures, the fractures would become saturated when the average film thickness is equal to half the average aperture. In this case, the air entry value  $P_d$  for fractures can be used as the reference capillary pressure. As a result, film thickness ratio and transmissivity ratio in Equation 78 are equivalent to the effective saturation ( $S_e$ ) and relative permeability ( $k_r$ ), respectively, for fractures. Equation 78 with  $\eta = -1$  is then rewritten as

$$S_e = \left| \frac{P_c}{P_d} \right|^{-\lambda} \quad (\text{Eq. 79a})$$

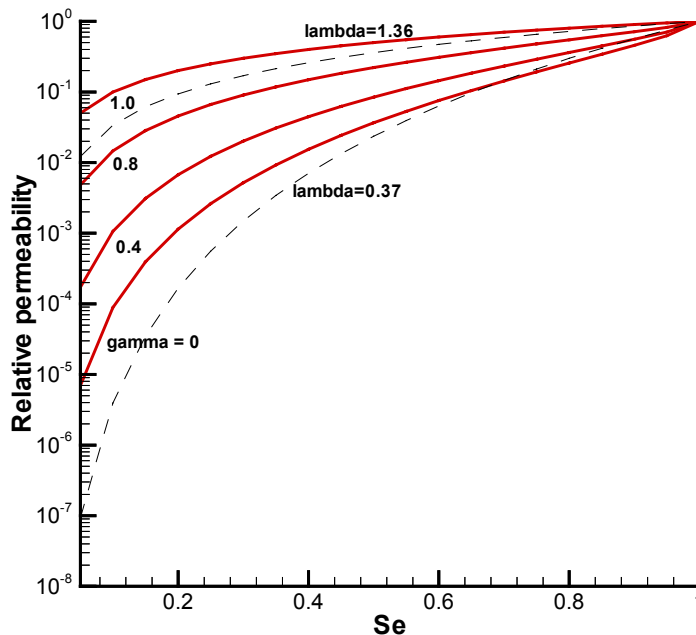
$$k_r = S_e^{2/\lambda} \quad (\text{Eq. 79b})$$

Note that for the same  $\lambda$  value, the ratio of relative permeability from the Brooks-Corey model (Equation 77) to that from Equation 79b is  $S_e^3$ , indicating that Equation 79b predicts much higher  $k_r$  value than the Brooks-Corey model at low saturations. That also explains why film flow corresponds to fast flow in unsaturated fractures. Equation 79 can be used to describe film flow within the context of the continuum approach, if all fractures are assumed to be hydraulically the same within a gridblock. Note that effects of variability in fracture aperture are not considered in

Equation 79. This issue may need further investigation in the future if the film flow is determined to be a key flow mechanism.

### 6.8.2 Model Comparison

This section provides a simple comparison between the film flow model (Equation 79) and the AFM. In welded units, water mainly percolates through fractures (Liu et al. 1998 [105729], Figure 12). For a given infiltration flux, pore velocity within fractures in a welded unit is proportional to the relative permeability, divided by the effective saturation, because fracture flow is gravity dominant (Liu et al. 1998 [105729]). Therefore, for a given relative permeability, it will be determined whether the effective saturation predicted by the film model, using parameters derived from observations by Tokunaga and Wan (1997 [139195]) and Tokunaga et al. (2000 [152914]), is approximately within the range of saturations calculated by the AFM for a range of  $\gamma$  values. If it is the case, pore velocity determined from the film-flow model should be approximately within the range of pore velocity predicted by the AFM. In other words, the fast flow behavior caused by fracture film flow is captured by the AFM.



Source: From experimental results of Tokunaga and Wan (1997 [139195]) and Tokunaga et al. (2000 [152914]).

Figure 12. Comparison Between Relative Permeability-Saturation Relations Calculated Using the AFM with  $m = 0.633$  (Table 7) for Several  $\gamma$  Values (Solid Lines) and Relations Calculated from the Film-Flow Model with  $\lambda$  Values (Dashed Lines)

Figure 12 shows a comparison between relative permeability-saturation relations calculated with the AFM and the film-flow model. For  $\lambda = 0.37$ , even the AFM with  $\gamma = 0$  (i.e., all connected fractures are active) can predict larger pore velocity at low saturations. For  $\lambda = 1.36$ , the relative permeability-saturation relation given by the film-flow model is consistent with the AFM with a  $\gamma$  value between 0.8 and 1.0. Therefore, fast flow predicted by the film-flow model with parameters obtained from observations by Tokunaga and Wan (1997 [139195]) and Tokunaga et

al. (2000 [152914]) can be captured by the AFM with different  $\gamma$  values. This largely results from the capability of the AFM to capture a large range of flow behaviors.

Although a typical  $\lambda$  value for the UZ is not available, the typical value is quite likely already bound by the two  $\lambda$  values used in Figure 12. This is based on the observation that water flow processes in the UZ are bound to those described by the AFM with  $\gamma$  values between 0 and 0.8, while relative permeability-saturation relations with this range of  $\gamma$  are bounded by the two relations determined with the two  $\lambda$  values (Figure 12). As indicated by Liu et al. (1998 [105729]), field observations support the concept that not all connected fractures are active in the UZ ( $\gamma > 0$ ). On the other hand, Liu et al. (1998 [105729], Figure 11) also showed that pore velocity within fractures in welded units is on the order of  $1.0\text{E-}4$  m/s (or 3154 m/yr) for  $\gamma=0.8$ . No evidence supports such a high pore velocity in the UZ. As a result, if film flow were indeed important in the UZ, the corresponding relative permeability-saturation relation would be bound by the relations for the two  $\lambda$  values shown in Figure 11. Consequently, the above comparison is likely valid for the Yucca Mountain UZ.

Note also that derivation of Equation 79 implies a uniform film flow in all fractures. This is supported by the widespread nature of the film flow observed from small-scale laboratory experiments (Tokunaga and Wan 1997 [139195]; Tokunaga et al. 2000 [152914]). This uniform film-flow generally results in a much larger degree of matrix diffusion (resulting from a larger fracture-matrix interfacial area) than with the AFM, and therefore a larger degree of retardation for radionuclide transport in the UZ, even when pore velocity is the same for the two models. All these considerations support the idea that AFM does not overestimate the performance of the UZ, even if film flow were the main mechanism for fracture flow in the UZ.

## **6.9 UNCERTAINTY, ALTERNATIVE MODELS (APPROACHES) AND OTHER ISSUES**

This report has two major objectives. The first objective is to determine uncalibrated properties for UZ model layers (Sections 6.1 – 6.4). Uncertainties of most of these properties are reported using the corresponding standard deviations or standard errors (e.g., Tables 6 – 8). Alternative approaches or alternative values from different sources have been used to verify the estimated properties (Sections 6.1.3.4, 6.2.4 and 6.5). As indicated in Section 1, these properties are uncalibrated and serve only as initial estimates in the Calibrated Properties Model. The calibrated properties are intended for use in the mountain-scale and drift-scale UZ models

The second objective is to evaluate the AFM presented in Section 6.6. The uncertainties of the AFM result from the representation of fracture systems with continua, the validity of the relevant hypotheses and accuracy of the estimated AFM parameters. The model validation activities (including determination of reasonable range of AFM parameter  $\gamma$ ) are reported in Section 7. Alternative model (film flow model and fractal-based model) and its comparison with the AFM are also included in Section 6.8.

## 7. VALIDATION

This section documents activities to validate the AFM and the corresponding model validation results.

### 7.1 MODEL VALIDATION ACTIVITIES

The AFM is a modification of the traditional dual-continuum model that specifies a constitutive relationship for unsaturated flow in fractures. This modification is motivated by field observations showing that under unsaturated conditions, not all fractures in a connected fracture network actually carry water flow (Liu et al. 1998 [105729], CRWMS M&O 2000 [141187], Section 6.4). The AFM has been reviewed and published by Liu et al. (1998 [105729]), and several papers describing simulation results from the UZ Model based on the AFM have been accepted for publication by *Journal of Contaminant Hydrology*, an international journal publishing scientific articles pertaining to the contamination of groundwater. Section 6.7 shows that the AFM is approximately consistent with a fractal-distribution behavior for liquid water (characterized by a fractal dimension) in a fracture network. The fractal flow behavior has been often reported in the literature for unsaturated flow and multiphase flow systems. The fractal analysis is used to analyze the fracture coating data from UZ, indicating that the UZ may also exhibit fractal flow behavior (Section 6.7). The validation of the AFM with field observations from the Yucca Mountain UZ, including fracture coating data and carbon-14 data, will be documented in this section. The criteria of model validation are given in the TWP (BSC 2002 [160819], Section I-1-3-1). The criteria for validation using carbon-14 data and fracture coating data are (a) that simulated water travel times are sensitive to AFM parameters and within the range of measured data for the TSw unit, and (b) that the simulated active portion of the fractures is similar to the percentage of fractures with mineral coatings, or (c) that other factors, not directly related to the AFM, can explain any significant disparity between simulations and the observed results. These criteria allow for validating the AFM by showing that model results based on the AFM are consistent with observations when the relevant results are sensitive to the AFM parameters. As will be shown in Section 7.2, these criteria ((a) and (b)) are met for the suitable AFM parameter values. In numerical simulations to be reported in this section, codes TOUGH2 V1.4 (LBNL 2000 [146496]) and T2R3D V1.4 (LBNL 1999 [146654]) are used. This is because these codes have been comprehensively tested and widely used for modeling UZ flow and transport. These codes also include the AFM features. The upstreaming weighting approach is used for modeling flow processes. The reasonableness of the approach was discussed in BSC (2003 [160240], Section 6).

### 7.2 VALIDATION OF THE ACTIVE FRACTURE MODEL WITH CARBON-14 AND MINERAL COATING DATA

Carbon-14 and fracture coating data are used for validating the AFM. They contain useful information regarding water flow and fracture-matrix interaction in the UZ under ambient conditions. It is especially of interest to examine if the AFM can represent two different data sets for a similar range of the AFM parameter  $\gamma$ . This model validation activity is documented in Scientific Notebooks (Wang 2003 [161654], SN-LBNL-SCI-227-V1, pp. 8–19, 21–54, 70–71, 73–84; SN-LBNL-SCI-199-V1, pp. 92–99).

### 7.2.1 Model validation with Carbon-14 Data

Carbon-14 data were collected from perched water, pore water, and gas samples from the Yucca Mountain UZ (BSC 2002 [160247], Section 6.6.4). Pore-water Carbon-14 data from various boreholes at Yucca Mountain were affected by contamination from atmospheric  $^{14}\text{CO}_2$  during drilling, which may result in apparently younger residence times (Yang 2002 [160839], Section 4.1.2; BSC 2002 [160247], Section 6.6.4.2). Carbon-14 data from gas samples are considered to be most representative of *in situ* conditions (Yang 2002 [160839], Section 4.1.2). Gas samples were collected from different kinds of boreholes including open surface-based boreholes and instrumented surface boreholes. The data from the latter boreholes (USW SD-12 and USW UZ-1) are the most reliable indicators of *in situ* conditions (BSC 2002 [160247], Section 6.6.4.3). Carbon-14 residence ages (BSC 2002 [160247], Table 20) calculated using the data from these two boreholes are used for validating the AFM. Water travel times from the ground surface to the perched water bodies are dominated by PTn where flow occurs mainly in the rock matrix and is thus insensitive to the AFM parameters (Wang 2003 [161654], SN-LBNL-SCI-227-V1, pp. 49–50). Therefore, carbon-14 data collected from perched water are not used for validating the AFM.

Gas-phase carbon-14 ages (DTN: GS961108312271.002 [121708] for borehole USW SD-12 and MO0012CARB1314.000 [153398] for borehole USW UZ-1) are interpreted to be representative of ages of the *in situ* pore water. The rationales for this interpretation are provided by Yang (2002 [160839], Section 4.1.2). This interpretation presumes rapid exchange of gas-phase  $\text{CO}_2$  (in hours to days) with dissolved  $\text{CO}_2$  and  $(\text{HCO}_3^-)$  in pore water. Furthermore, the amount of C in an aqueous-phase pore water relative to C in the  $\text{CO}_2$  gas-phase reservoir is a hundred times greater. Consequently, the aqueous phase will dominate the gaseous phase when exchange occurs, indicating the reasonableness of the interpretation (Yang 2002 [160839], Section 4.1.2).

One-dimensional numerical models are developed for boreholes USW SD-12 and USW UZ-1. Numerical grids for these models are taken from DTN: LB02091DSSCP3I.001 [161292]. The measurement elevations are determined from collar elevations of the boreholes (DTN: MO9906GPS98410.000 [109059]) and depth information given in the DTNs in the above paragraph. The calibrated rock properties for present-day, mean infiltration maps are used except  $\gamma$  values (DTN: LB02091DSSCP3I.002 [161433]). Value of the AFM parameter  $\gamma$  for model layers tsw32 to tsw38 is varied for different simulations to check the sensitivity of this parameter to simulated water travel times. Top boundary condition corresponds to the present-day infiltration rate for flow simulations and a constant tracer concentration for transport simulations. Initial conditions for solute transport include zero concentration within the fractured rocks. Previous studies indicate that dispersion processes have an insignificant effect on overall solute transport behavior in unsaturated fractured rocks (BSC 2001 [158726], Section 6.8.1), and therefore they are ignored here. An effective-diffusion-coefficient value of  $1.97\text{E-}10 \text{ m}^2/\text{s}$  is employed in this study and equal to the average value of measured coefficients for tritiated water (DTN: LA000000000034.002 [148603]; BSC 2002 [160828], Table 16). TOUGH2 V1.4 (LBNL 2000 [146496]) and T2R3D V1.4 (LBNL 1999 [146654]) codes (Table 1) are used for simulating steady-state water flow and tracer transport processes. (The input and output files associated with these software items are described in Scientific Notebook (Wang 2003 [161654], SN-LBNL-SCI-227-V1, pp. 8–19, 21–54, 70–71, and 73–84) and submitted to Technical Data Management System (TDMS) under Output DTNs: LB0212C14INFIL.001 and

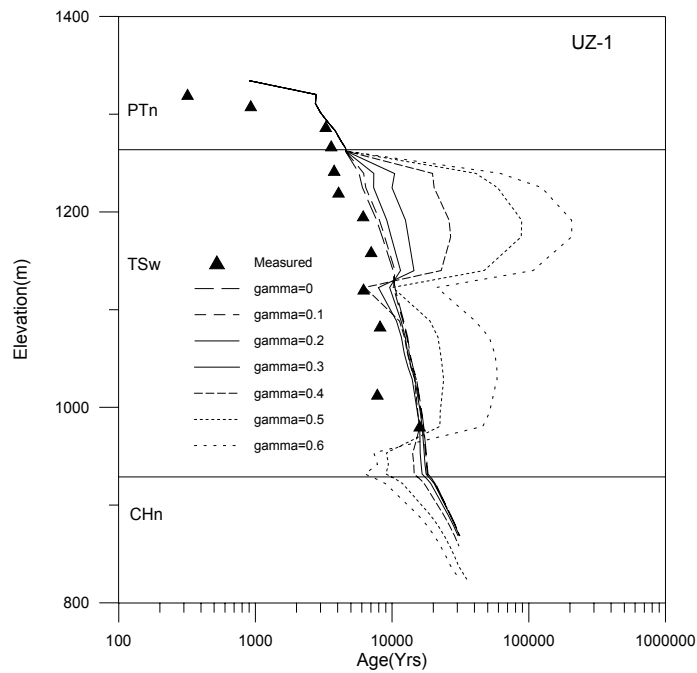
LB0212AFPGAMMA.001.) Simulated water travel times (or ages) for rock matrix are compared with carbon-14 ages. A simulated water travel time at a location is determined as the time when the matrix concentration reaches 50% of the top-boundary concentration. It represents the average travel time for water particles from the ground surface to the location.

Figure 13 shows simulated water travel times (ages) for different  $\gamma$  values of UZ Model layers tsw32 to tsw38. The considerable sensitivity of simulated results to  $\gamma$  indicates that Carbon-14 data are useful for validating the AFM and for constraining the  $\gamma$  values for the TSw unit. For  $\gamma$  values ranging from 0.2 to 0.4, simulated results approximately match the observations. A larger  $\gamma$  value generally corresponds to a larger travel time for the matrix because of a smaller degree of matrix diffusion, resulting from a smaller fracture-matrix interfacial area available for mass transport between fractures and the matrix.

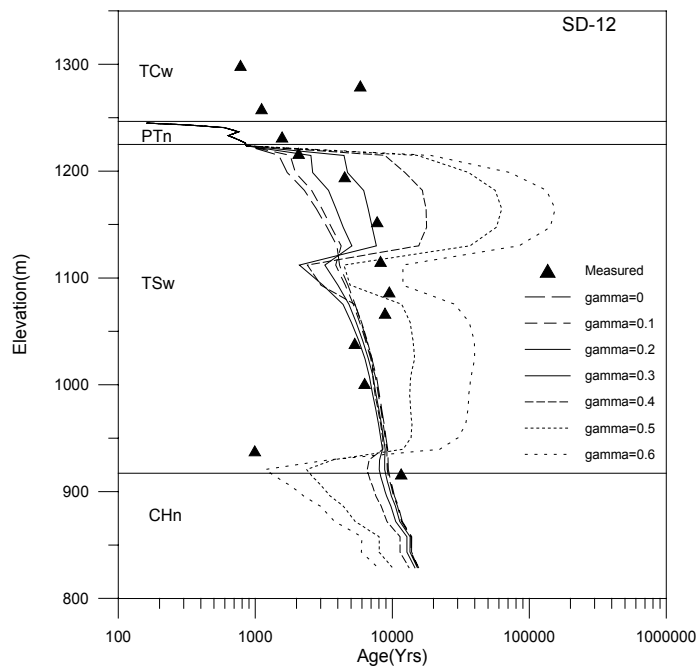
Simulated water travel times change sharply at an elevation of about 1,100 m for two boreholes (Figure 13). This is because the upper portion of the TSw unit has relatively small fracture density values and thus corresponds to a smaller degree of matrix diffusion for a given  $\gamma$  value (Table 7). For the borehole USW UZ-1, simulated water travel time is generally longer than the observation for a given elevation. This may be a result of subsurface heterogeneity, which gives larger fracture densities (resulting in a larger degree of matrix diffusion) at the borehole location than what are used in the numerical model. Layer-averaged fracture properties are used in the UZ Model (Section 5). Also note that unlike the case for USW SD-12, the simulation result for  $\gamma=0$  provides the best match to the data for USW UZ-1. This may again result from the spatial variability. Like many other hydraulic properties (e.g., permeability),  $\gamma$  is spatially variable. Nevertheless,  $\gamma=0.2-0.4$  gives the reasonable matches to the data from the two boreholes simultaneously.

In summary, a comparison between simulated water travel times and observed carbon-14 ages indicates that the AFM with  $\gamma$  values between 0.2 to 0.4 (for UZ model layers tsw32-tsw38) can reasonably represent the data.

(a)



(b)



Output - DTN: LB0212C14INFIL.002 (files: C14\_UZ-1\_age.doc and C14\_SD-12\_age.doc)

Source: Wang (2003 [161654], SN-LBNL-SCI-227-V1, p. 87)

Figure 13. Comparisons Between Simulated Water Travel Times (Ages) for Rock Matrix at Boreholes (a) USW UZ-1 and (b) USW SD-12, as well as the Corresponding Carbon-14 Ages for Several  $\gamma$  Values

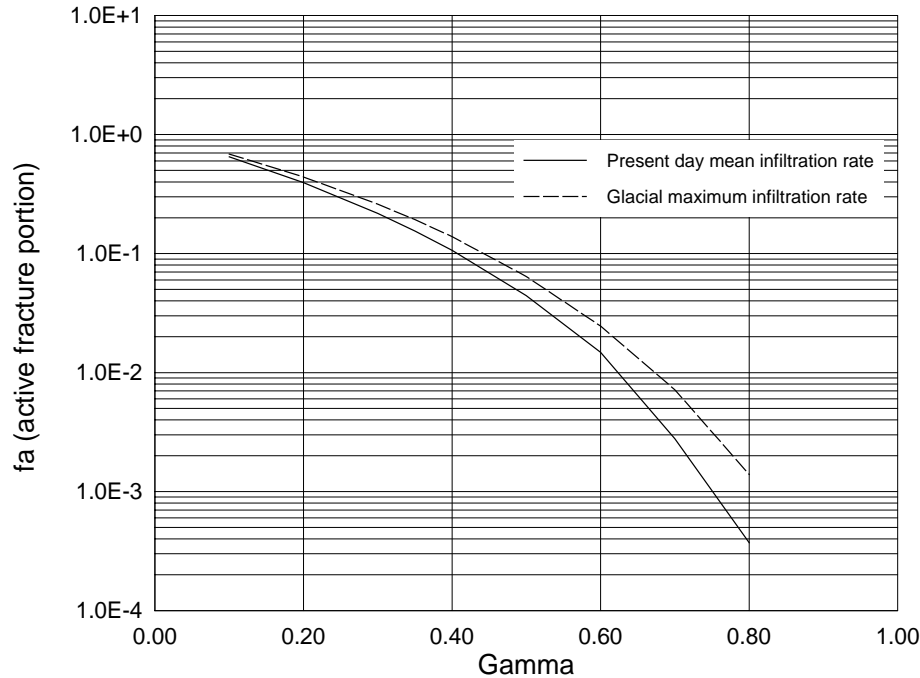
### 7.2.2 Model Validation with Mineral Coating Data

The process of UZ mineral deposition is initiated during infiltration. Here, meteoric water interacts with materials in the soil, after which a portion may then enter the bedrock fracture network. Fracture coating is generally a signature of water flow paths. Therefore, the coating data are useful for validating the AFM that describes water flow in fractures.

Fracture coating data were collected in the ESF (DTN: GS980308315215.008 [107355]). Observed spatial distribution of fractures with coatings is used to estimate the portion of active fractures in the UZ. For a given survey interval along ESF, a frequency of coated fractures can be estimated for a geologic unit, based on the total number of coated fractures. The ratio of coated-fracture frequency to total fracture frequency (Table 7) will provide an estimate of the portion of active fracture for the given geologic unit (Wang 2003 [161654], SN-LBNL-SCI-227-V1, pp. 70–71). The estimated average portion of the active fracture for the TSw is 7.2%. The abundance of mineral coating (coating volume divided by total rock volume), divided by the corresponding fracture porosity, gives another estimate of the portion of the active fractures in the UZ under ambient conditions. Abundance data for all intervals in welded tuffs have an arithmetic mean of 0.084% (BSC 2002 [160247], Section 6.10.1.1), while a typical fracture porosity is 1% (Table 7). Therefore, an estimate of the average portion of active fractures for welded units is  $\frac{0.084\%}{1\%} = 8.4\%$ , close to the estimate determined from frequency of coated fractures. Note that fracture coatings may not precisely represent active flow paths in the UZ and some flow paths may not have coatings (Liu et al. 1998 [105729]). Nevertheless, these values at least give a rough estimate of lower limits for the portion of active fractures in the UZ – about 10%.

Mineral growth rate data imply that the UZ fracture network has maintained a large degree of hydrologic stability over time, and fracture flow paths in the deep unsaturated zone are buffered from climate-induced variations in precipitation and infiltration (BSC 2002 [160247], Section 6.10.3.9). If the AFM actually represents water flow processes in the UZ, modeling results based on the AFM should be consistent with this important observation.

To check the consistency of the AFM against the coating data, a one-dimensional model for borehole USW SD-12 is used. The model is the same as that described in Section 7.2.1. USW SD-12 is chosen because it is located near the middle of the ESF, where coating data were collected. Two infiltration rates, present data mean infiltration rate and glacial maximum infiltration rate, are used for simulations. Again, uniform  $\gamma$  distributions within model layers tsw32 to tsw38 are employed. The latter infiltration rate is about five times as large as the former rate and represents the maximum infiltration rate in past climates.



Output - DTN: LB0212AFPGAMMA.002 (files: gamma\_analysis.doc, FA\_GA\_GU.dat and FA\_GA\_PM.dat)

Figure 14. Simulated Average Portion of Active Fracture for the Relevant Model Layers (tsw32 to tsw38) as a Function of Infiltration Rate and  $\gamma$

Figure 14 shows the simulated average portion of active fractures,  $f_a$ , for the relevant model layers (tsw32 to tsw38) as a function of infiltration rate and  $\gamma$ . The average portion is calculated from Equation 52 using the average effective saturation for model layers tsw32 to tsw38. The calculated  $f_a$  values range about 10% for  $\gamma$  values close to 0.4, which are similar to those used for matching the carbon-14 data. For the same range of  $\gamma$  values, the calculated  $f_a$  values do not change significantly for the two infiltration rates (Figure 14), which is consistent with the observation of flow-path stability over time. The present day mean infiltration rate is obtained from file GENER\_m\_rad\_200 in DTN: LB0208UZDSCPMI.001 [161285]. The glacial maximum infiltration rate is determined using software routine infil2grid V1.7 [154793] based on infiltration maps (USGS 2001 [160355]) (DTN: GS000308311221.005 [147613]) and UZ numerical grid (DTN: LB03023DKMGRID.001 [162354]) (Wang 2003 [161654], SN-LBNL-SCI-199-V1, pp. 92–99; SN-LBNL-SCI-227-V1, pp. 8–9). The determined glacial maximum infiltration rate is 17.3108 mm/yr (Wang 2003 [161654], SN-LBNL-SCI-227-V1, p. 8).

In summary, the simulation results based on the AFM are consistent with both carbon-14 data and fracture coating data, for a similar range of  $\gamma$  values. This result, together with the consistency of the AFM with fractal flow patterns (Section 6.7), supports the validity of the AFM. No further activities are needed to complete this model validation for its intended use.

## 8. CONCLUSIONS

Methodologies have been described for providing representative estimates of fracture and matrix properties for UZ Model layers, based on the relevant data. The fracture and matrix properties developed here were submitted to the TDMS under Output-DTNs: LB0205REVUZPRP.001 and LB0207REVUZPRP.002, respectively. Thermal properties developed here were submitted to the TDMS under Output-DTN: LB0210THRMLPRP.001. Fault properties developed here were submitted to the TDMS under Output-DTN: LB0207REVUZPRP.001. Estimated properties are also documented in this report for use as prior information in the inversion processes in a separate Model Report documenting the *Calibrated Properties Model* (BSC 2003 [160240]). The resultant fracture geometry properties are important inputs for the development of the UZ Model grids. The independent determination of fracture properties, based on ESF seepage test results, confirms the appropriateness of the estimated fracture properties and the procedures used for the estimation. The summarized simulation results for the AFM validation were also submitted to the TDMS under Output-DTNs: LB0212AFPGAMMA.002 and LB0212C14INFIL.002.

Like many field-scale problems, data availability and limitations in approaches for upscaling flow parameters directly from small-scale measurements are major sources of uncertainties in the estimated hydraulic properties. It is particularly true for the unsaturated fractured rocks, due to the complexity of the flow processes involved. To reduce the uncertainties, model calibrations are generally needed. Calibration is discussed in a separate Model Report describing the *Calibrated Properties Model* (BSC 2003 [160240]). Therefore, it should be emphasized that flow parameter estimates reported herein are only developed as inputs into model calibrations, and should not be directly used for modeling UZ flow and transport processes without careful evaluation. The calibrated properties should be used for the relevant modeling studies.

This report also documents activities to validate the AFM and the corresponding model validation results. The AFM is evaluated on the basis of (fractal) flow patterns in unsaturated systems, the consistency with different types of field observations, and a comparison with an alternative (film-flow) model. The AFM is shown to be consistent with fractal distributions of flow patterns that have been often observed from unsaturated or multiphase flow systems (porous media). Simulation results based on the AFM, with a similar range of AFM-parameter values, match both the carbon-14 ages and fracture coating data collected from the UZ. Furthermore, a simple comparison between the AFM and the film-flow model, an alternative model, shows that the AFM would capture the fast flow behavior of water film if film flow were the major mechanism for fracture flow. All these support the validity of the AFM in describing flow and transport processes in the UZ.

In addition to the Output-DTNs mentioned above, the output DTNs containing support files for the AFM validation study (LB0212C14INFIL.001 and LB0212AFPGAMMA.001) were also submitted for TDMS. All Output-DTNs from this report are listed in Section 9.4.

INTENTIONALLY LEFT BLANK

## 9. INPUTS AND REFERENCES

The following is a list of the references cited in this document. Column 1 represents the unique six digit numerical identifier (the Document Input Reference System [DIRS] number), which is placed in the text following the reference callout (e.g., BSC 2002 [155950]). The purpose of these numbers is to assist the reader in locating a specific reference. Within the reference list, multiple sources by the same author (e.g., BSC 2002) are sorted alphabetically by title.

### 9.1 CITED DOCUMENTS

- 155853 Ahlers, R. 2000. *Unsaturated Zone Modeling & Synthesis*. Scientific Notebook YMP-LBNL-GSB-1.1.2. ACC: MOL.20000726.0157.
- 116773 Bear, J.; Tsang, C.F.; and de Marsily, G., eds. 1993. *Flow and Contaminant Transport in Fractured Rock*. San Diego, California: Academic Press. TIC: 235461.
- 156915 Brooks, R.H. and Corey, A.T. 1964. *Hydraulic Properties of Porous Media*. Hydrology Paper No. 3. Fort Collins, Colorado: Colorado State University. TIC: 217453.
- 159725 BSC (Bechtel SAIC Company) 2001. *Analysis of Hydrologic Properties Data*. ANL-NBS-HS-000002 REV 00 ICN 01. Las Vegas, Nevada: Bechtel SAIC Company. ACC: MOL.20020429.0296.
- 158463 BSC (Bechtel SAIC Company) 2001. *In Situ Field Testing of Processes*. ANL-NBS-HS-000005 REV 01. Las Vegas, Nevada: Bechtel SAIC Company. ACC: MOL.20020108.0351.
- 160828 BSC (Bechtel SAIC Company) 2001. *Unsaturated Zone and Saturated Zone Transport Properties (U0100)*. ANL-NBS-HS-000019 REV 00 ICN 02. Las Vegas, Nevada: Bechtel SAIC Company. ACC: MOL.20020311.0017.
- 158726 BSC (Bechtel SAIC Company) 2001. *UZ Flow Models and Submodels*. MDL-NBS-HS-000006 REV 00 ICN 01. Las Vegas, Nevada: Bechtel SAIC Company. ACC: MOL.20020417.0382.
- 160247 BSC (Bechtel SAIC Company) 2002. *Analysis of Geochemical Data for the Unsaturated Zone*. ANL-NBS-HS-000017 REV 00 ICN 02. Las Vegas, Nevada: Bechtel SAIC Company. ACC: MOL.20020314.0051.
- 159124 BSC (Bechtel SAIC Company) 2002. *Geologic Framework Model (GFM2000)*. MDL-NBS-GS-000002 REV 01. Las Vegas, Nevada: Bechtel SAIC Company. ACC: MOL.20020530.0078.

- 160819 BSC (Bechtel SAIC Company) 2002. *Technical Work Plan for: Performance Assessment Unsaturated Zone*. TWP-NBS-HS-000003 REV 02. Las Vegas, Nevada: Bechtel SAIC Company. ACC: MOL.20030102.0108.
- 160319 BSC (Bechtel SAIC Company) 2002. *Thermal Conductivity of the Potential Repository Horizon Model Report*. MDL-NBS-GS-000005 REV 00. Las Vegas, Nevada: Bechtel SAIC Company. ACC: MOL.20020923.0167.
- 160146 BSC (Bechtel SAIC Company) 2002. *Total System Performance Assessment-License Application Methods and Approach*. TDR-WIS-PA-000006 REV 00. Las Vegas, Nevada: Bechtel SAIC Company. ACC: MOL.20020923.0175.
- 160240 BSC (Bechtel SAIC Company) 2003. *Calibrated Properties Model*. MDL-NBS-HS-000003 REV 01. Las Vegas, Nevada: Bechtel SAIC Company. ACC: DOC.20030219.0001.
- 160109 BSC (Bechtel SAIC Company) 2003. *Development of Numerical Grids for UZ Flow and Transport Modeling*. ANL-NBS-HS-000015 REV 01. Las Vegas, Nevada: Bechtel SAIC Company. URN-1080
- 102679 CRWMS M&O (Civilian Radioactive Waste Management System Management and Operating Contractor) 1998. *Geology of the Exploratory Studies Facility Topopah Spring Loop*. BAB000000-01717-0200-00002 REV 01. Las Vegas, Nevada: CRWMS M&O. ACC: MOL.19980415.0283.
- 141187 CRWMS M&O 2000. *Conceptual and Numerical Models for UZ Flow and Transport*. MDL-NBS-HS-000005 REV 00. Las Vegas, Nevada: CRWMS M&O. ACC: MOL.19990721.0526.
- 153045 CRWMS M&O 2001. *Seepage Calibration Model and Seepage Testing Data*. MDL-NBS-HS-000004 REV 01. Las Vegas, Nevada: CRWMS M&O. ACC: MOL.20010122.0093.
- 157916 Curry, P.M. and Loros, E.F. 2002. *Project Requirements Document*. TER-MGR-MD-000001 REV 00. Las Vegas, Nevada: Bechtel SAIC Company. ACC: MOL.20020806.0027.
- 100569 Domenico, P.A. and Schwartz, F.W. 1990. *Physical and Chemical Hydrogeology*. New York, New York: John Wiley & Sons. TIC: 234782.
- 160844 Feder, J. 1988. *Fractals*. New York, New York: Plenum Press. TIC: 253584.
- 151875 Finsterle, S. 2000. "Using the Continuum Approach to Model Unsaturated Flow in Fractured Rock." *Water Resources Research*, 36, (8), 2055-2066. [Washington, D.C.]: American Geophysical Union. TIC: 248769.

- 100033 Flint, L.E. 1998. *Characterization of Hydrogeologic Units Using Matrix Properties, Yucca Mountain, Nevada*. Water-Resources Investigations Report 97-4243. Denver, Colorado: U.S. Geological Survey. ACC: MOL.19980429.0512.
- 160845 Flury, M. and Flühler, H. 1995. "Modeling Solute Leaching in Soils by Diffusion-Limited Aggregation: Basic Concepts and Application to Conservative Solutes." *Water Resources Research*, 31, (10), 2443-2452. [Washington, D.C.]: American Geophysical Union. TIC: 253609.
- 127326 Francis, N.D. 1997. "The Base-Case Thermal Properties for TSPA-VA Modeling." Memorandum from N.D. Francis (SNL) to Distribution, April 16, 1997. ACC: MOL.19980518.0229.
- 154365 Freeze, G.A.; Brodsky, N.S.; and Swift, P.N. 2001. *The Development of Information Catalogued in REV00 of the YMP FEP Database*. TDR-WIS-MD-000003 REV 00 ICN 01. Las Vegas, Nevada: Bechtel SAIC Company. ACC: MOL.20010301.0237.
- 161806 Freifeld, B.M. 2001. *Estimation of Fracture Porosity in an Unsaturated Fractured Welded Tuff Using Gas Tracer Testing*. Ph.D. thesis. Berkeley, California: University of California, Berkeley, Department of Civil and Environmental Engineering. TIC: 253904.
- 101388 Gelhar, L.W. 1993. *Stochastic Subsurface Hydrology*. Englewood Cliffs, New Jersey: Prentice-Hall. TIC: 240652.
- 160751 Glass, R.J. 1993. "Modeling Gravity-Driven Fingering in Rough-Walled Fractures Using Modified Percolation Theory." *High Level Radioactive Waste Management, Proceedings of the Fourth Annual International Conference, Las Vegas, Nevada, April 26-30, 1993*. 2, 2042-2052. La Grange Park, Illinois: American Nuclear Society. TIC: 208542.
- 101868 Hvorslev, M.J. 1951. *Time Lag and Soil Permeability in Ground-Water Observations*. AEWES Bulletin 36. Vicksburg, Mississippi: U.S. Army Corps of Engineers, Waterways Experiment Station. TIC: 238956.
- 147209 Kazemi, H. and Gilman, J.R. 1993. "Multiphase Flow in Fractured Petroleum Reservoirs." Chapter 6 of *Flow and Contaminant Transport in Fractured Rock*. Bear, J.; Tsang, C-F.; and de Marsily, G., eds. San Diego, California: Academic Press. TIC: 235461.
- 101700 LeCain, G.D. 1995. *Pneumatic Testing in 45-Degree-Inclined Boreholes in Ash-Flow Tuff Near Superior, Arizona*. Water-Resources Investigations Report 95-4073. Denver, Colorado: U.S. Geological Survey. ACC: MOL.19960715.0083.

- 100052 LeCain, G.D. 1998. *Results from Air-Injection and Tracer Testing in the Upper Tiva Canyon, Bow Ridge Fault, and Upper Paintbrush Contact Alcoves of the Exploratory Studies Facility, August 1994 through July 1996, Yucca Mountain, Nevada*. Water-Resources Investigations Report 98-4058. Denver, Colorado: U.S. Geological Survey. ACC: MOL.19980625.0344.
- 144612 LeCain, G.D.; Anna, L.O.; and Fahy, M.F. 2000. *Results from Geothermal Logging, Air and Core-Water Chemistry Sampling, Air-Injection Testing, and Tracer Testing in the Northern Ghost Dance Fault, Yucca Mountain, Nevada, November 1996 to August 1998*. Water-Resources Investigations Report 99-4210. Denver, Colorado: U.S. Geological Survey. TIC: 247708.
- 160832 Lide, D.R., ed. 2002. *CRC Handbook of Chemistry and Physics*. 83rd Edition. Boca Raton, Florida: CRC Press. TIC: 253582.
- 116797 Lin, M.; Hardy, M.P.; and Bauer, S.J. 1993. *Fracture Analysis and Rock Quality Designation Estimation for the Yucca Mountain Site Characterization Project*. SAND92-0449. Albuquerque, New Mexico: Sandia National Laboratories. ACC: NNA.19921204.0012.
- 155675 Liu, H.H. 2001. *Unsaturated Zone Modeling and Synthesis*. Scientific Notebook YMP-LBNL-GSB-LHH-2. ACC: MOL.20010802.0134.
- 160110 Liu, H.H. and Bodvarsson, G.S. 2001. "Constitutive Relations for Unsaturated Flow in a Fracture Network." *Journal of Hydrology*, 252, ([1-4]), 116-125. [New York, New York]: Elsevier. TIC: 253269.
- 105729 Liu, H.H.; Doughty, C.; and Bodvarsson, G.S. 1998. "An Active Fracture Model for Unsaturated Flow and Transport in Fractured Rocks." *Water Resources Research*, 34, (10), 2633-2646. Washington, D.C.: American Geophysical Union. TIC: 243012.
- 160848 Mandelbrot, B.B. 1983. *The Fractal Geometry of Nature*. New York, New York: W.H. Freeman. TIC: 253583.
- 139143 Millington, R.J. and Quirk, J.M. 1961. "Permeability of Porous Solids." *Transactions of the Faraday Society*, 57, (7), 1200-1207. Toronto, Canada: Royal Society of Chemistry. TIC: 246707.
- 101146 Moench, A.F. 1989. "Convergent Radial Dispersion: A Laplace Transform Solution for Aquifer Tracer Testing." *Water Resources Research*, 25, (3), 439-447. Washington, D.C.: American Geophysical Union. TIC: 238283.
- 100161 Montazer, P. and Wilson, W.E. 1984. *Conceptual Hydrologic Model of Flow in the Unsaturated Zone, Yucca Mountain, Nevada*. Water-Resources Investigations Report 84-4345. Lakewood, Colorado: U.S. Geological Survey. ACC: NNA.19890327.0051.

- 139151 National Research Council 1996. *Rock Fractures and Fluid Flow, Contemporary Understanding and Applications*. Washington, D.C.: National Academy Press. TIC: 235913.
- 105731 Neuman, S.P. 1994. "Generalized Scaling of Permeabilities: Validation and Effect of Support Scale." *Geophysical Research Letters*, 21, (5), 349-352. Washington, D.C.: American Geophysical Union. TIC: 240142.
- 160849 Neuman, S.P.; Illman, W.A.; Vesselinov, V.V.; Thompson, D.L.; Chen, G.; and Guzman, A. 2001. "Lessons from Field Studies at the Apache Leap Research Site in Arizona." Chapter 10 of *Conceptual Models of Flow and Transport in the Fractured Vadose Zone*. Washington, D.C.: National Academy Press. TIC: 252777.
- 162418 NRC (U.S. Nuclear Regulatory Commission) 2003. *Yucca Mountain Review Plan, Information Only*. NUREG-1804, Draft Final Revision 2. Washington, D.C.: U.S. Nuclear Regulatory Commission, Office of Nuclear Material Safety and Safeguards. TIC: 254002.
- 105736 Paleologos, E.K.; Neuman, S.P.; and Tartakovsky, D. 1996. "Effective Hydraulic Conductivity of Bounded, Strongly Heterogeneous Porous Media." *Water Resources Research*, 32, (5), 1333-1341. Washington, D.C.: American Geophysical Union. TIC: 245760.
- 160840 Persson, M.; Yasuda, H.; Albergel, J.; Berndtsson, R.; Zante, P.; Nasri, S.; and Ohrstrom, P. 2001. "Modeling Plot Scale Dye Penetration by a Diffusion Limited Aggregation (DLA) Model." *Journal of Hydrology*, 250, ([1-4]), 98-105. [New York, New York]: Elsevier. TIC: 253606.
- 105743 Philip, J.R.; Knight, J.H.; and Waechter, R.T. 1989. "Unsaturated Seepage and Subterranean Holes: Conspectus, and Exclusion Problem for Circular Cylindrical Cavities." *Water Resources Research*, 25, (1), 16-28. Washington, D.C.: American Geophysical Union. TIC: 239117.
- 100684 Pruess, K. 1987. *TOUGH User's Guide*. NUREG/CR-4645. Washington, D.C.: U.S. Nuclear Regulatory Commission. TIC: 217275.
- 104250 Pruess, K. 1999. "A Mechanistic Model for Water Seepage Through Thick Unsaturated Zones in Fractured Rocks of Low Matrix." *Water Resources Research*, 35, (4), 1039-1051. Washington, D.C.: American Geophysical Union. TIC: 244913.
- 102097 Rousseau, J.P.; Kwicklis, E.M.; and Gillies, D.C., eds. 1999. *Hydrogeology of the Unsaturated Zone, North Ramp Area of the Exploratory Studies Facility, Yucca Mountain, Nevada*. Water-Resources Investigations Report 98-4050. Denver, Colorado: U.S. Geological Survey. ACC: MOL.19990419.0335.

- 160841 Schaap, M.G. and Leij, F.J. 2000. "Improved Prediction of Unsaturated Hydraulic Conductivity with the Mualem-van Genuchten Model." *Soil Science Society of America Journal*, 64, ([3]), 843-851. [Madison, Wisconsin]: Soil Science Society of America. TIC: 253607.
- 101479 Starr, R.C.; Gillham, R.W.; and Sudicky, E.A. 1985. "Experimental Investigation of Solute Transport in Stratified Porous Media, 2. The Reactive Case." *Water Resources Research*, 21, (7), 1043-1050. Washington, D.C.: American Geophysical Union. TIC: 222358.
- 160846 Stauffer, D. and Aharony, A. 2001. *Introduction to Percolation Theory*. 2nd Edition. Philadelphia, Pennsylvania: Taylor & Francis. TIC: 253585.
- 139195 Tokunaga, T.K. and Wan, J. 1997. "Water Film Flow Along Fracture Surfaces of Porous Rock." *Water Resources Research*, 33, (6), 1287-1295. Washington, D.C.: American Geophysical Union. TIC: 242739.
- 152914 Tokunaga, T.K.; Wan, J.; and Sutton, S.R. 2000. "Transient Film Flow on Rough Fracture Surfaces." *Water Resources Research*, 36, (7), 1737-1746. [Washington, D.C.]: American Geophysical Union. TIC: 249028.
- 160355 USGS (U.S. Geological Survey) 2001. *Simulation of Net Infiltration for Modern and Potential Future Climates*. ANL-NBS-HS-000032 REV 00 ICN 02. Denver, Colorado: U.S. Geological Survey. ACC: MOL.20011119.0334.
- 100610 van Genuchten, M.T. 1980. "A Closed-Form Equation for Predicting the Hydraulic Conductivity of Unsaturated Soils." *Soil Science Society of America Journal*, 44, (5), 892-898. Madison, Wisconsin: Soil Science Society of America. TIC: 217327.
- 161654 Wang, J.S. 2003. "Scientific Notebooks Referenced in Model Report U0090, Analysis of Hydrologic Properties Data, MDL-NBS-HS-000014 REV 00" Interoffice correspondence from J.S. Wang (BSC) to File, February 28, 2003, with attachments. ACC: MOL.20030306.0535.
- 106793 Wang, J.S.Y. and Narasimhan, T.N. 1993. "Unsaturated Flow in Fractured Porous Media." Chapter 7 of *Flow and Contaminant Transport in Fractured Rock*. Bear, J.; Tsang, C-F.; and de Marsily, G., eds. San Diego, California: Academic Press. TIC: 235461.
- 155770 Wang, Z.; Feyen, J.; and Elrick D.E. 1998. "Prediction of Fingering in Porous Media." *Water Resources Research*, 34, (9), 2183-2190. [Washington, D.C.]: American Geophysical Union. TIC: 250733.
- 160843 Yamamoto, H.; Kojima, K.; and Tosaka, H. 1993. "Fractal Clustering of Rock Fractures and Its Modeling Using Cascade Process." *Scale Effects in Rock Masses, [Proceedings of the Second International Workshop on Scale Effects in Rock Masses, Lisbon, Portugal, June 25, 1993]*. da Cunha, P., ed. Pages 81-86. Rotterdam, The Netherlands: A.A. Balkema. TIC: 253608.

- 160839 Yang, I.C. 2002. "Percolation Flux and Transport Velocity in the Unsaturated Zone, Yucca Mountain, Nevada." *Applied Geochemistry*, 17, ([6]), 807-817. [New York, New York]: Elsevier. TIC: 253605.

### Software Cited

- 134754 LBNL (Lawrence Berkeley National Laboratory) 1999. *Software Code: infil2grid*. V1.6. PC with Windows/95 or 98. Sun or DEC Workstation with Unix OS. 10077-1.6-00.
- 146654 LBNL (Lawrence Berkeley National Laboratory) 1999. *Software Code: T2R3D*. V1.4. FORTRAN 77, SUN, DEC / ALPHA. 10006-1.4-00.
- 146496 LBNL (Lawrence Berkeley National Laboratory) 2000. *Software Code: TOUGH2*. V1.4. Sun Workstation and DEC/ALPHA. 10007-1.4-01.
- 154793 LBNL (Lawrence Berkeley National Laboratory) 2002. *Software Code: infil2grid*. V1.7. DEC-Alpha, PC. 10077-1.7-00.

## 9.2 CODES, STANDARDS, REGULATIONS, AND PROCEDURES

- 156605 10 CFR 63. Energy: Disposal of High-Level Radioactive Wastes in a Geologic Repository at Yucca Mountain, Nevada. Readily available.
- AP-2.22Q, Rev. 0. *Classification Criteria and Maintenance of the Monitored Geologic Repository Q-List*. Washington, D.C.: U.S. Department of Energy, Office of Civilian Radioactive Waste Management. ACC: MOL.20020314.0046.
- AP-3.15Q, Rev. 3, ICN 4. *Managing Technical Product Inputs*. Washington, D.C.: U.S. Department of Energy, Office of Civilian Radioactive Waste Management. ACC: MOL.20021105.0163.
- AP-SI.1Q, Rev. 4. *Software Management*. Washington, D.C.: U.S. Department of Energy, Office of Civilian Radioactive Waste Management. ACC: MOL.20030113.0149.
- AP-SV.1Q, Rev. 0, ICN 3. *Control of the Electronic Management of Information*. Washington, D.C.: U.S. Department of Energy, Office of Civilian Radioactive Waste Management. ACC: MOL.20020917.0133.
- YMP-LBNL-QIP-SV.0 Rev. 2, Mod. 1. *Management of YMP-LBNL Electronic Data*. Berkeley, California: Lawrence Berkeley National Laboratory. ACC: MOL.20020717.0323.

## 9.3 SOURCE DATA, LISTED BY DATA TRACKING NUMBER

- 147613 GS000308311221.005. Net Infiltration Modeling Results for 3 Climate Scenarios for FY99. Submittal date: 03/01/2000.
- 160822 GS010608312242.001. Unsaturated Hydraulic Conductivity and Matric Potential in Busted Butte Volcanic Tuff Cores. Submittal date: 08/07/2001.

- 155533 GS940208314211.007. Table of Contacts in Borehole USW UZ-N35. Submittal date: 02/10/1994.
- 145581 GS940208314211.008. Table of Contacts in Boreholes USW UZ-N57, UZ-N58, UZ-N59, and UZ-N61. Submittal date: 02/10/1994.
- 145589 GS940308314211.018. Table of Contacts for the Tiva Canyon Tuff in Borehole USW UZ-N36. Submittal date: 03/28/1994.
- 152558 GS950108314211.008. Lithostratigraphic Data for Paintbrush Group Bedded Tuff Units TPBT3 and TPBT4 in Boreholes USW UZ-N11, USW UZ-14, USW NRG-7/7A, USW SD-9, USW UZ-N37, USW NRG-6, UE-25 NRG#2B, USW UZ-N31, USW UZ-N32, USW SD-12, UE-25 UZ#16, USW UZ-N54, USW UZ-N53. Submittal date: 01/20/1995.
- 152556 GS950108314211.009. Stratigraphic Descriptions and Data for the Yucca Mountain Tuff in Boreholes NRG#2B, NRG-7/7A, SD-9, UZ-14, UZ#16, UZ-N11, UZ-N33, UZ-N34, UZ-N53, UZ-N54, UZ-N55. Submittal date: 01/27/1995.
- 144662 GS950608312231.008. Moisture Retention Data from Boreholes USW UZ-N27 and UE-25 UZ#16. Submittal date: 06/06/1995.
- 160827 GS950708314211.028. Stratigraphic Descriptions of the Pah Canyon Tuff in Boreholes UE-25 NRG #2B, UE-25 NRG#4, USW NRG-6, USW NRG-7/7A, USW SD-9, USW SD-12, USW UZ-14, USW UZ-N31, USW UZ-N32, AND USW UZ-N37. Submittal date: 07/20/1995.
- 147590 GS960808312231.003. Moisture Retention Data for Samples from Boreholes USW SD-7, USW SD-9, USW SD-12 and UE-25 UZ#16. Submittal date: 08/30/1996.
- 105574 GS960908312232.013. Air-Injection Testing in Vertical Boreholes in Welded and Non-Welded Tuff, Yucca Mountain, Nevada. Submittal date: 09/26/1996.
- 121708 GS961108312271.002. Chemical and Isotopic Composition of Pore Water and Pore Gas, 1994–96, from Boreholes USW UZ-1, USW UZ-14, UE-25 UZ#16, USW NRG-6, USW NRG-7A, USW SD-7, USW SD-9, ESF-AL#3-RBT#1, and ESF-AL#3-RBT#4, and ESF Rubble. Submittal date: 12/04/1996.
- 105580 GS970183122410.001. Results from Air-Injection and Tracer Testing in the Upper Tiva Canyon, Bow Ridge Fault, and Upper Paintbrush Contact Alcoves of the Exploratory Studies Facility, August 1994 through July 1996, Yucca Mountain, Nevada. Submittal date: 02/03/1997.
- 107184 GS971008312231.006. Physical Properties and Saturated Hydraulic Conductivity of Cores from Surface Samples from the ESF Main Drift 29+00 M to 57+00 M. Submittal date: 10/06/1997.

- 107165 GS980308312242.005. Physical Properties of Lexan-Sealed Borehole Samples from the PTN Exposure in the ESF North Ramp (ESF Station 7+27 M to ESF Station 10+70 M). Submittal date: 03/11/1998.
- 107355 GS980308315215.008. Line Survey Information from the Exploratory Studies Facility Obtained to Estimate Secondary Mineral Abundance. Submittal date: 03/24/1998.
- 107161 GS980408312242.008. Unsaturated Hydraulic Properties of Borehole Samples from the PTN Exposure in the ESF North Ramp (ESF Station 7+27 M to ESF Station 10+70 M) Measured Using a Centrifuge. Submittal date: 04/17/1998.
- 106752 GS980708312242.010. Physical Properties of Borehole Core Samples, and Water Potential Measurements Using the Filter Paper Technique, for Borehole Samples from USW WT-24. Submittal date: 07/27/1998.
- 107150 GS980708312242.011. Physical Properties and Hydraulic Conductivity Measurements of Lexan-Sealed Samples from USW WT-24. Submittal date: 07/30/1998.
- 149375 GS980808312242.012. Unsaturated Hydraulic Properties of Lexan-Sealed Samples From USW WT-24, Measured Using a Centrifuge. Submittal date: 08/05/1998.
- 106748 GS980808312242.014. Physical Properties of Borehole Core Samples and Water Potential Measurements Using the Filter Paper Technique for Borehole Samples from USW SD-6. Submittal date: 08/11/1998.
- 107180 GS980908312242.037. Water Retention Data of Lexan-Sealed Borehole Samples and Surface Samples from ESF North Ramp Moisture Study. Submittal date: 09/23/1998.
- 107154 GS980908312242.038. Physical Properties and Saturated Hydraulic Conductivity Measurements of Lexan-Sealed Samples from USW SD-6. Submittal date: 09/22/1998.
- 145272 GS980908312242.039. Unsaturated Water Retention Data for Lexan-Sealed Samples from USW SD-6 Measured Using a Centrifuge. Submittal date: 09/22/1998.
- 107169 GS980908312242.040. Physical Properties and Saturated Hydraulic Conductivity Measurements of Core Plugs from Lexan-Sealed Samples from Boreholes in the ESF North Ramp. Submittal date: 09/24/1998.
- 107158 GS980908312242.041. Physical Properties and Saturated Hydraulic Conductivity Measurements of Core Plugs from Boreholes USW SD-7, USW SD-9, USW SD-12, USW UZ-14, and UE-25 UZ#16. Submittal date: 09/24/1998.
- 107185 GS990308312242.007. Laboratory and Centrifuge Measurements of Physical and Hydraulic Properties of Core Samples from Busted Butte Boreholes UZTT-BB-INJ-1,

- UZTT-BB-INJ-3, UZTT-BB-INJ-4, UZTT-BB-INJ-6, UZTT-BB-COL-5 and UZTT-BB-COL-8. Submittal date: 03/22/1999.
- 109822 GS990708312242.008. Physical and Hydraulic Properties of Core Samples from Busted Butte Boreholes. Submittal date: 07/01/1999.
- 135230 GS990883122410.002. Qualified Data in “Results from Geothermal Logging, Air and Core-Water Chemistry Sampling, Air-Injection Testing and Tracer Testing in the Northern Ghost Dance Fault, November, 1996 - August, 1998”. Submittal date: 08/16/1999.
- 148603 LA000000000034.002. Diffusion of Sorbing and Non-Sorbing Radionuclides. Submittal date: 06/22/1993.
- 160824 LA0207SL831372.001. Lithostratigraphic Classification of Hydrologic-Property Core-Sampling Depths, Busted Butte Phase 2 Test Block. Submittal date: 07/16/2002.
- 160825 LAJF831222AQ98.014. Chloride, Bromide, and Sulfate Analyses of Salts Leached from ESF-NR-Moiststddy Drillcore. Submittal date: 09/09/1998.
- 156907 LB0110LIQR0015.001. Developed Data for Liquid Release/Seepage Tests and Systematic Testing. Submittal date: 11/12/2001.
- 161285 LB0208UZDSCPMI.001. Drift-Scale Calibrated Property Sets: Mean Infiltration Supporting Files. Submittal date: 08/27/2002.
- 161292 LB02091DSSCP3I.001. 1-D Site Scale Calibrated Properties: Supporting Files. Submittal date: 09/18/2002.
- 161433 LB02091DSSCP3I.002. 1-D Site Scale Calibrated Properties: Data Summary. Submittal date: 09/18/2002.
- 162354 LB03023DKMGRID.001. UZ 3-D Site Scale Model Grids. Submittal date: 02/26/2003.
- 105587 LB960500834244.001. Hydrological Characterization of the Single Heater Test Area in ESF. Submittal date: 08/23/1996.
- 105589 LB970600123142.001. Ambient Characterization of the ESF Drift Scale Test Area by Field Air Permeability Measurements. Submittal date: 06/13/1997.
- 105590 LB980120123142.004. Air Injections in Boreholes 57 through 61, 74 through 78, 185 and 186 in the Drift Scale Test Area. Submittal date: 01/20/1998.
- 114134 LB980120123142.005. Hydrological Characterization by Air Injections Tests in Boreholes in Heated Drift in DST. Submittal date: 01/20/1998.

- 105592 LB980901233124.003. Liquid Release and Tracer Tests in Niches 3566, 3650, 3107, and 4788 in the ESF. Submittal date: 09/14/1998.
- 105593 LB980912332245.002. Gas Tracer Data from Niche 3107 of the ESF. Submittal date: 09/30/1998.
- 106787 LB990501233129.001. Fracture Properties for the UZ Model Grids and Uncalibrated Fracture and Matrix Properties for the UZ Model Layers for AMR U0090, "Analysis of Hydrologic Properties Data". Submittal date: 08/25/1999.
- 123273 LB990901233124.004. Air Permeability Cross-Hole Connectivity in Alcove 6, Alcove 4, and Niche 4 of the ESF for AMR U0015, "In Situ Testing of Field Processes". Submittal date: 11/01/1999.
- 153398 MO0012CARB1314.000. Water - Carbon 13 and Carbon 14 Abundance. Submittal date: 12/01/2000.
- 153777 MO0012MWDGFM02.002. Geologic Framework Model (GFM2000). Submittal date: 12/18/2000.
- 155989 MO0109HYMXP001.001. Matrix Hydrologic Properties Data. Submittal date: 09/17/2001.
- 161496 MO0301SEPFEPS1.000. LA FEP List. Submittal date: 01/21/2003. URN-1084
- 109059 MO9906GPS98410.000. Yucca Mountain Project (YMP) Borehole Locations. Submittal date: 06/23/1999.
- 160258 SN0206T0503102.005. Thermal Conductivity of the Non-Repository Layers of Yucca Mountain. Submittal date: 06/27/02.
- 160257 SN0208T0503102.007. Thermal Conductivity of the Potential Repository Horizon Rev 3. Submittal date: 08/26/2002.
- 160826 TM000000UZ7ARS.001. USW UZ-7A Shift Drilling Summaries, Lithologic Logs, Structural Logs, Weight Logs, and Composite Borehole Log from 0.0' to 770.0'. Submittal date: 09/05/1995.

#### **9.4 OUTPUT DATA, LISTED BY DATA TRACKING NUMBER**

LB0205REVUZPRP.001. Fracture Properties for UZ Model Layers Developed from Field Data. Submittal date: 05/14/2002.

LB0207REVUZPRP.001. Revised UZ Fault Zone Fracture Properties. Submittal date: 07/03/2002.

LB0207REVUZPRP.002. Matrix Properties for UZ Model Layers Developed from Field and Laboratory Data. Submittal date: 07/15/2002.

LB0210THRMLPRP.001. Thermal Properties of UZ Model Layers: Data Summary. Submittal date: 10/25/2002.

LB0212C14INFIL.001. 1-D Simulation and Sensitivity Analyses of Groundwater Age by Matching to C14 Age Data: 1. Supporting Files. Submittal date: 12/19/2002.

LB0212C14INFIL.002. 1-D Simulation and Sensitivity Analyses of Groundwater Age by Matching to C14 Age Data: 2. Data Summaries. Submittal date: 12/19/2002.

LB0212AFPGAMMA.001. Active Fracture Parameter Analysis: 1. Supporting Files. Submittal date: 12/23/2002.

LB0212AFPGAMMA.002. Active Fracture Parameter Analysis: 2. Data Summaries. Submittal date: 12/23/2002.

## **10. ATTACHMENTS**

Attachment I – Data Point Values in Figures 10 and 11

Attachment II – Data Point Values in Figure 7

Attachment III – Description of Excel Files Used

INTENTIONALLY LEFT BLANK

**ATTACHMENT I—DATA POINT VALUES IN FIGURES 10 AND 11.****Data point values in Figure 9 (estimated from Figure 9 of Tokunaga et al. (2000 [152914])):**

Average film thickness ( $\mu\text{m}$ )	Surface transmissivity ( $\text{m}^2/\text{s}$ )
1.2	2.5E-16
1.5	1.0E-14
2.0	1.5E-13
2.5	7.0E-13
3.0	2.0E-12
3.5	7.0E-12
4.0	1.0E-11
5.0	2.5E-11

**Data point values in Figure 10 (a) (estimated from Figure 7 of Tokunaga and Wan (1997 [139195])):**

Capillary potential (Pa)	Average film thickness ( $\mu\text{m}$ )
-310	1.0
-215	2.0
-165	3.0
-118	5.0
-93	7.0
-70	8.0
-45	20.0
-30	30.0
-14	70.0

**Data point values in Figure 10 (b) (estimated from Figure 6 of Tokunaga and Wan (1997 [139195])):**

Capillary pressure (Pa)	Surface transmissivity (m <sup>2</sup> /s)
-250	8.0E-11
-200	1.5E-10
-150	3.5E-10
-100	8.0E-10
-50	3.5E-9
-12	4.0E-8

**ATTACHMENT II—DATA POINT VALUES IN FIGURE 7.**

Coating data from DTN: GS980308315215.008 [107355] are used to determine the data point values. Since Tptpmn unit has the largest number of survey intervals, data from this unit are analyzed using the box counting method. There are 29 survey intervals (30 m long) for this unit that include coated fractures. The total number of coated fractures is 134. The locations of the coated fractures along the survey line form a set of points in a one-dimensional space. For a given box size (length of a segment)  $l$ , there are  $30/l$  small boxes (or segments) for a given survey interval.  $N$  denotes total numbers of boxes that cover at least one location of the coated fractures (along the survey line) for all the survey intervals. The determined  $N$  values as a function of  $l$  are given as follows:

$N$	$l$ (m)
102	3
91	3.75
83	5
81	6
68	7.5
63	10
50	15
29	30

## ATTACHMENT III - Description of Excel Files

This attachment describes Excel files used for developing uncalibrated hydraulic properties. All data mentioned in this attachment were downloaded directly from TDMS unless otherwise noted. All Excel files were also submitted to TDMS.

### hydroprops\_fin.xls (OUTPUT DTN: LB0207REVUZPRP.002)

This file was used to develop matrix properties for UZ model layers.

#### *Worksheet 'borehole data'*

- Import DTN: MO0109HYMXP.001 [155989].
- Import DTN: GS980708312242.010 [106752] (WT-24 physical properties), and GS980808312242.014 [106748] (SD-6 physical properties) into same columns used in MO0109HYMXP.001 [155989].
- Import DTN: GS980708312242.011 [107150] (WT-24 high pressure permeameter conductivity), GS980908312242.038 [107154] (SD-6 high pressure permeameter conductivity), and GS980908312242.041 [107158] (SD-7, SD-9, SD-12, UZ-14, and UZ#16 high pressure permeameter conductivity) into columns AA – AD.
- Added column D, depth in ft, converted from column F.
- Added column J, residual water content (RWC), with conditional formatting to highlight  $RWC \geq 5\%$ .
- Calculated saturation, in column N, for WT-24 and SD-6.
- Added GFM lithostratigraphy from MO0012MWDGFM02.002 [153777] file contacts00md.dat to columns S & T. Where contacts00md.dat did not have borehole, note in column U indicates source of lithostratigraphy (DTNs also listed in rows 5389-5398: GS950108314211.009 [152556], GS940208314211.007 [155533], GS940308314211.018 [145589], GS950108314211.008 [152558], GS950708314211.028 [160827], GS940208314211.008 [145581], TM000000UZ7ARS.001 [160826]).

Hydrostratigraphy (hydrogeologic unit – HGU) is determined in column V (based on rules of Flint (1998 [100033], pp. 21-32); groupings indicated below are for UZ Model layers:

- 1 & 2 = CCR & CUC  $\approx$  Tpcrn & Tpcrl, lower contact (l.c.) of CCR where porosity ( $\phi$ ) > 9%, l.c. of CUC where  $\phi < 20\%$ . Units are combined because greater property resolution is not needed at upper margin of UZ Model.
- 3 & 4 = CUL & CW  $\approx$  Tpcpul & Tpcpmn & Tpcpll & Tpcpln, l.c. of CUL at lithostratigraphic contact (l.c. of Tpcpul of identified in columns P & Q, but contact is unimportant for UZ Model hydrostratigraphy), l.c. of CW where  $\phi > 15\%$ . Units are combined because greater property resolution is not needed at upper margin of UZ Model.
- 5 = CMW  $\approx$  base of Tpcpln & Tpcpv3 & Tpcpv2, l.c. where  $\phi > 28\%$

- 6 = CNW  $\approx$  base of Tpcpv2 & Tpcpv1, l.c. at lithostratigraphic contact (l.c. of Tpcpv1)
- 7 = BT4  $\approx$  Tpbt4 & top of Tpy, l.c. where  $\phi > 30\%$  or at l.c. of Tpy whichever is stratigraphically higher
- 8 = TPY  $\approx$  moderately welded interior of Tpy, l.c. where  $\phi < 30\%$
- 9 = BT3  $\approx$  base of Tpy & Tpbt3, l.c. at lithostratigraphic contact (l.c. of Tpbt3) (note: if Tpbt4 is not present and Tpy  $\phi > 30\%$  then all Tpy is included in BT3)
- 10 = TPP = Tpp
- 11 = BT2  $\approx$  Tpbt2 & Tptrv3 & Tptrv2, l.c. at lithostratigraphic contact (l.c. of Tptrv2)
- 12 = TC  $\approx$  Tptrv1 & top of Tptrn, l.c. where  $\phi > 9\%$
- 13 = TR  $\approx$  Tptrn, l.c. at lithostratigraphic contact (l.c. of Tptrn)
- 14 = TUL = Tptrl & Tptpul
- 15 = TMN = Tptpmn
- 16 = TLL = Tptpll
- 17 & 18 = TM2 & TM1 = Tptpln
- 19 = PV3 = Tptpv3
- 20 = PV2a = altered Tptpv2 (altered vitric rocks defined where residual water content  $\geq 5\%$ )
- 20.1 = PV2v = vitric Tptpv2
- 21 = BT1a = altered Tptpv1 & Tpbt1
- 21.1 = BT1v = vitric Tptpv1 & Tpbt1
- 22 = CHV = vitric Tac
- 23 = CHZ = altered (zeolitic) Tac
- 24 = BTa = altered Tacbt
- 24.1 = BTv = vitric Tacbt
- 25 = PP4 = Tcpu
- 26 = PP3 = Tcpu
- 27 = PP2  $\approx$  Tcprn & Tcplc, l.c. where residual water content  $\geq 5\%$
- 28 = PP1  $\approx$  Tcplv & Tcplt & Tcbuv, l.c. where residual water content  $< 5\%$
- 29 = BF3  $\approx$  Tcbuc & Tcbrn & Tcble, l.c. at lithostratigraphic contact (l.c. of Tcble)
- 30 = BF2 = Tcblv & Tcbbt & Tctuv
- 31 = TR3 = Tctuc

Differences between HGU picks from MO0109HYMXP001 [155989] are indicated by non-zero values and highlighting in column W.

*Worksheet 'hydroprops'*

- Worksheet 'borehole data' is copied and renamed 'hydroprops'.
- Columns D, E, F, H, K, M, O-R, U, and W from 'borehole data' are deleted.
- Columns G, I, H, K, L, J, and N from 'hydroprops' are copied to columns D to J, respectively.
- All saturation values greater than one in column J are changed to one.
- The logarithm of all the hydraulic conductivity measurement are collected in column U. Where two hydraulic conductivity measurements were made on the same sample the high pressure permeameter measurement from column Q is chosen.
- Values are copied from column U to column V.
- Rows 62 to 5387 are sorted by column M (HGU).

*Worksheet '007 Ks'*

- Import DTN: GS990308312242.007 [107185] (Busted Butte lab measurements of hydrologic properties).
- The logarithm of hydraulic conductivity is calculated in column J.

*Worksheet '007 n'*

- Import DTN: GS990308312242.007 [107185] (Busted Butte lab measurements of physical properties).

*Worksheet '98.008 Ks'*

- Import DTN: GS990708312242.008 [109822] (Busted Butte lab measurements of hydrologic properties).
- The logarithm of hydraulic conductivity is calculated in column G.

*Worksheet '98.008 n'*

- Import DTN: GS990708312242.008 [109822] (Busted Butte lab measurements of physical properties).

*Worksheet '006 Ks'*

- Import DTN: GS971008312231.006 [107184] (ESF surface sample lab measurements of saturated hydraulic conductivity).

*Worksheet 'Ksat w ND'*

- All columns except F, G, and V from 'hydroprops' are copied to 'Ksat w ND'.
- All rows from 62 to 5387 without conductivity values are deleted.
- All rows in HGUs without non-detect conductivity measurements (noted as "nf" or "NF") are deleted.
- Hydraulic conductivity, SPC #, and sample # are copied from '006 Ks' to HGU #15 columns O, Q, and R, respectively.

- Within each HGU (or group of HGUs as defined above) rows are sorted by ascending conductivity with non-detects first.
- The conductivity for each remaining HGU is ranked in column T.
- The rank is converted to a percentile in column U, where percentile equals rank divided by (total number of measurements plus one).
- The NORMSINV function is applied to the percentile in column V. This gives (the value minus the expected value) divided by the standard deviation for that percentile in a normal distribution, which is analogous to plotting the log conductivity values on probability paper.

The intercept and slope of the line fitted through the NORMSINV values (x-axis) and the log conductivity values (y-axis) give the expected value and the standard deviation, respectively, of the log conductivity data and account for the unknown values of the non-detect measurements, which are assumed to be less than the lowest conductivity measured.

#### *Worksheet 'Summary'*

Matrix properties for each UZ Model layer are shown. Columns and rows are labeled.

For relative humidity porosity ( $\phi(RH)$ ), porosity ( $\phi$ ), saturation (S), bulk density ( $\rho$  bulk), and particle density ( $\rho$  particle), the arithmetic mean, standard deviation, number of samples, and standard error are given. Standard error is standard deviation divided by the square root of number of samples. Minimum and maximum values of saturation are also given. Note: data from only one sample are available for the BTv; these data are not inconsistent with the BT1v, so the BT1v will be used as an analog for the BTv.

Residual saturation ( $S_r$ ), here equal to porosity minus relative humidity porosity, is given in column O. Note: again BT1v should be used as an analog for the BTv.

For log conductivity, the arithmetic mean, standard deviation, number of samples with a measured conductivity, standard error (the standard deviation divided by the square root of the number of samples with a measured conductivity), and number of non-detect measurements are given in columns X – AB. Where there are non-detect measurements, these values are shown in red italics. Note: again BT1v should be used as an analog for the BTv.

The mean and standard deviation of the log conductivity data for layers with non-detect measurements (the intercept and slope of the data in worksheet 'Ksat w ND') are shown in columns AD and AE. The standard error is calculated in column AF as the standard deviation divided by the square root of the total number of conductivity measurements including non-detects.

Log conductivity is converted to log permeability in column AI, where permeability equals conductivity times water viscosity divided by water density and gravity. Permeability is shown in column AH. Upscaled log permeability is calculated in column AL, where permeability is upscaled by the factor of 0.38 times the variance. Upscaled permeability is shown in column AK. Note: again BT1v should be used as an analog for the BTv; additionally, BT1a should be used as an analog for the PV2a, and PP1 should be used as an analog for the BF2.

**MRC\_Q\_TCw\_fin.xls (OUTPUT-DTN: LB0207REVUZPRP.002)**

This file was used to develop matrix properties for UZ model layers.

*Worksheet '037 wc'*

- Import DTN: GS980908312242.037 [107180] (ESF North Ramp moisture study borehole sample water retention water content data).

*Worksheet '037 wp'*

- Import DTN: GS980908312242.037 [107180] (ESF North Ramp moisture study borehole sample water retention water potential data).

*Worksheet '008 wp & wc(g per g)'*

- Import DTN: GS980408312242.008 [107161] (ESF North Ramp moisture study borehole sample water retention data).

*Worksheet '040 Ks'*

- Import DTN: GS980908312242.040 [107169] (ESF North Ramp moisture study borehole sample saturated hydraulic conductivity data).

*Worksheet '040 por +'*

- Import DTN: GS980908312242.040 [107169] (ESF North Ramp moisture study borehole sample physical properties data).

*Worksheet '005 bd'*

- Import DTN: GS980308312242.005 [107165] (ESF North Ramp moisture study borehole sample bulk density data).

*Worksheet '005 105n'*

- Import DTN: GS980308312242.005 [107165] (ESF North Ramp moisture study borehole sample oven dried porosity data).

*Worksheet '005 RHn'*

- Import DTN: GS980308312242.005 [107165] (ESF North Ramp moisture study borehole sample relative humidity oven porosity data).

*Worksheet '008 Kr'*

- Import DTN: GS980408312242.008 [107161] (ESF North Ramp moisture study borehole sample relative permeability data).
- Calculate saturation in column H from water content (column G) by assuming that the maximum water content for each sample is equal to a saturation of one.
- Calculate saturation in column I from water content (column G) by assuming that the maximum water content for each sample as measured for the water potential data (worksheet '008 wp & wc(g per g)' column G) is equal to a saturation of one.
- Calculate saturation in column J from water content (column G) by assuming that a water content equal to the porosity (from either worksheet '040 por +' column G rows 39 to 49 or worksheet '005 105n' column B) represents a saturation of one.
- Calculate relative permeability in column K from conductivity (column B) by assuming that the maximum conductivity for each sample is equal to a relative permeability of one.
- Calculate relative permeability in column L from conductivity (column B) by assuming that the saturated conductivity (from worksheet '040 Ks' column B) is equal to a relative permeability of one.

*Worksheet '039 wc'*

- Import DTN: GS980908312242.039 [145272] (USW SD-6 water retention water content data).
- Use data from hydroprops.xls worksheet 'borehole data' to make HGU assignments for each sample (column G).

*Worksheet '039 wp'*

- Import DTN: GS980908312242.039 [145272] (USW SD-6 water retention water potential data).
- Use data from hydroprops.xls worksheet 'borehole data' to make HGU assignments for each sample (column G).

*Worksheet 'in-situ'*

- Copy average, minimum, and maximum in-situ saturation from hydroprops.xls worksheet summary to columns B, C, and D, respectively for HGUs in column A.
- Copy average in-situ water potential from DATAfix\_satsum.xls (Wang 2003 [161654], SN-LBNL-SCI-003-V2, p. 65; Ahlers 2000 [155853], pp. 93–94) worksheet 'summary' to column E for HGUs in column A. Note that the averaged data are used for demonstration and not used for calculations. Therefore, they do not have any effect on the determined matrix property.
- Dummy values for plotting in column F.

*Worksheet 'CUC'*

1. Import DTN: MO0109HYMXP.001 [155989] (water retention Hydrologic Properties data from File MRCQ, Worksheet-CUCQ).
2. Assignment of samples to HGU is checked against hydroprops.xls worksheet 'borehole data'.
3. Saturation (column D) is (re)calculated assuming that the highest measured water content for each sample is equivalent to full saturation.
4. Data with water potential values less than ~1.4 bars (note: for plotting reasons water potential is expressed here as a positive number rather than the conventional negative number) that were acquired with a chilled-mirror psychrometer (data from other than borehole USW SD-6 or moisture study boreholes in the ESF North Ramp) are moved to the bottom of columns A – E and are excluded from further use.
5. Water content is plotted vs. water potential with chilled-mirror psychrometer data shown in open diamond symbols. Each sample is shown in a different color.
6. van Genuchten parameters saturated saturation, residual saturation, alpha,  $n$ , and  $m$  are labeled and are at the top of columns G and H (note: saturated saturation fixed equal to one; residual saturation is fixed to the value calculated in hydroprops\_fin.xls 'Summary';  $m=1-(1/n)$ ).
7. Saturation,  $S$ , is predicted in column G based on the measured water potential and the van Genuchten parameters using the following expression,
 
$$S = S_r + (S_s - S_r) \left[ 1 + (\alpha P_c)^n \right]^{-m}$$
 where  $S_r$  is residual saturation,  $S_s$  is saturated saturation,  $P_c$  is water potential, and  $\alpha$ ,  $n$ , and  $m$  are van Genuchten parameters.
8. The squared error (difference) between the predicted saturation and the measured saturation is calculated in column H and summed in cell H29.

9. The solver function of Excel is used to estimate values for  $\alpha$  and  $n$  by minimizing the sum of the squared error (cell H29). Note: all optional solver settings are default; where necessary the following constraints are added:  
 $\alpha \geq 0 \quad n \geq 1$
10. Saturation is calculated in column J based on the van Genuchten water retention function, the estimated parameters, and a range of water potential values in column I. The results are plotted as a red line.
11. The Jacobian matrix is calculated numerically in columns L – M using the perturbed parameter values given in cells M26:M28.

$$J_{ij} = \frac{\partial z_i}{\partial p_j}$$

is an element of the Jacobian matrix where  $z_i$  is the  $i^{\text{th}}$  predicted value (of saturation for this problem), and  $p_j$  is the  $j^{\text{th}}$  parameter. Note because  $n$  and  $m$  are not independent, Jacobian elements for parameter  $n$  are not evaluated.

12. The parameter covariance matrix, evaluated in cells P32:Q33, is

$$\mathbf{C}_{pp} = s_0^2 (\mathbf{J}^T \mathbf{J})^{-1}$$

where  $s_0^2$  is the sum of the squared error divided by the degree of freedom (# of data points - # of parameters) and  $\mathbf{J}$  is the Jacobian matrix.

13. The uncertainty (analogous to the standard error calculated for other hydrologic parameters in hydroprops.xls worksheet ‘Summary’) of the estimated parameters is calculated in cells P36:P37 as the square root of the diagonal elements of  $\mathbf{C}_{pp}$ .
14. The 95% error band (two standard errors) on the fitted van Genuchten curve are calculated in columns R and S and plotted as gray lines.

#### *Worksheet ‘CUL & CW’*

1. Import DTN: MO0109HYMXPROP.001 [155989] (water retention Hydrologic Properties data from File MRCQ, Worksheet-CULQ and Worksheet CWQ).
  - 1a. Appropriate data from worksheets ‘039 wc’ and ‘039 wp’ are added to columns B, C, and E.
  2. Same as step 2 above.
  - 2a. Sample N27 61.9r is not within either the CUL or CW and is removed.
  3. Same as step 3 above.
  4. Same as step 4 above.
  - 4a. Data with water potential values of 0.0 bars that were acquired with a centrifuge (data from borehole USW SD-6 or moisture study boreholes in the ESF North Ramp) are moved to the bottom of columns A – E and are excluded from further use.
  5. Same as step 5 above
  - 5a. Centrifuge data are shown as filled circles. Each centrifuge sample is shown in a different color that is not necessarily different from the colors used for the chilled-mirror psychrometer data.
  6. Same as step 6 above.
  7. Same as step 7 above.
  8. Same as step 8 above.

9. Same as step 9 above.
10. Same as step 10 above.
11. Same as step 11 above.
12. Same as step 12 above.
13. Same as step 13 above.
14. Same as step 14 above.
15. Average in-situ water potential and saturation data from worksheet 'in-situ' is plotted with  $\pm 2$  bar error bars.

*Worksheet 'CMW'*

1. Import DTN: MO0109HYMXP.001 [155989] (water retention Hydrologic Properties data from File MRCQ, Worksheet-CMWQ).
- 1a. Appropriate data from worksheets '037 wc' and '037 wp' are identified by the lithostratigraphy and ESF station in DTN: LAJF831222AQ98.014 [160825] and ESF station of contacts from Table 2 in CRWMS M&O (1998 [102679]) and are added to columns B, C, and E.
- 1b. Appropriate data from worksheet '008 wp & wc(g per g)' are identified as in step 1a above are added to columns B, C, and E.
- 1c. Appropriate data from worksheets '039 wc' and '039 wp' are added to columns B, C, and E.
2. Same as step 2 above.
3. Same as step 3 above.
- 3a. The saturation for the data from 1a is calculated assuming that the highest water content from either worksheet '008 wp & wc(g per g)' or '008 Kr' for that sample represents the water content at full saturation.
4. Same as step 4 above.
- 4a. Same as step 4a above.
5. Same as step 5 above.
- 5a. Same as step 5a above.
6. Same as step 6 above.
7. Same as step 7 above.
8. Same as step 8 above.
9. Same as step 9 above.
10. Same as step 10 above.
- 10a. Plotting the estimated function shows that the shape of the curve does not match well with the data. The parameters ( $\alpha$  and  $n$ ) are adjusted by hand to improve the subjective match between the shape of the curve and the data. This adjustment results in an increase of 0.22 (9%) in the sum of the squared error.
11. Same as step 11 above.
12. Same as step 12 above.
13. Same as step 13 above.
14. Same as step 14 above.
15. Same as step 15 above.
16. Appropriate unsaturated conductivity data from worksheet '008 Kr' are identified as in step 1a above, added to columns V, W, and X, and are plotted as circles connected by a dashed line. As in 3a, the saturation is

calculated assuming that the highest water content measured for the sample represents full saturation (column W is linked to either column H or I in '008 Kr').

$$17. \text{ Relative permeability is } k_{rw} = (S_e)^\eta \left[ 1 - (1 - S_e^{1/m})^m \right]^2$$

where  $\eta$  and  $m$  are fitting parameters and

$$S_e = \frac{(S - S_r)}{(S_s - S_r)}$$

where  $S$  is saturation,  $S_r$  is residual saturation, and  $S_s$  is satiated saturation. Use of a match point,  $S_0$ , that is near, but not at, full saturation is recommended to avoid problems with identification of full saturation and large changes in unsaturated conductivity very near saturation due to macropores. Relative permeability can then be redefined in terms of the conductivity at the match point:

$$\frac{K_w(S_e)}{K_w(S_{e,0})} = \left( \frac{S_e}{S_{e,0}} \right)^\eta \left[ \frac{1 - (1 - S_e^{1/m})^m}{1 - (1 - S_{e,0}^{1/m})^m} \right]^2$$

where  $S_{e,0}$  is the effective saturation at the match point and  $K_w(S_{e,0})$  is the conductivity at the match point. A saturation match point,  $S_{e,0}$ , of 0.95 is used for the CMW. The unsaturated conductivity at the match point,  $K_w(S_{e,0})$ , is calculated in column Z for each sample by linear interpolation between the nearest saturation and log conductivity data points.

18. The redefined relative permeability, left side of last equation in step 17, is calculated in column Y.
19. The relative permeability predicted from the saturation data (column W), as expressed on the right side of the last equation in step 17, is calculated in column AA. Parameters  $m$  and  $S_r$  are the same as for the water retention function.
20. The squared error (difference) between the predicted relative permeability and the measured relative permeability is calculated in column AB and summed in cell AB31.
21. The solver function of Excel is used to estimate  $\eta$ , cell X29, by minimizing the sum of the squared error (cell X23, which is linked to cell AB31). Note: all optional solver settings are default.
22. The Jacobian matrix is calculated numerically in column AC using the perturbed  $\eta$  value given in cell AC29. The variance and standard error of  $\eta$  are calculated in cells AD34 and AE34, respectively.
23. Relative permeability is calculated in column U for a range of saturation values in column T. The results are plotted as an orange line.
24. The average, minimum, and maximum in-situ saturation are plotted as a gray circle and error bars.

**MRC\_Q\_PTn\_fin.xls (OUTPUT-DTN: LB0207REVUZPRP.002)****THIS FILE WAS USED TO DEVELOP MATRIX PROPERTIES FOR UZ MODEL LAYERS.**

Worksheets 'in-situ', '037 wc', '037 wp', '008 Kr', '040 por +', '005 bd', '005 105n', '005 RHn', '008 wp & wc(g per g)', '039 wc', '039 wp' are prepared as for MRC\_Q\_TCw\_fin.xls with the exception of relative permeability calculations documented in steps 16 - 23 below which are carried out in worksheet '008 Kr'.

*Worksheets 'CMW', 'BT4', 'TPY', 'BT3', 'TPP', and 'BT2'*

1. Import DTN: MO0109HYMXPROP.001 [155989] (water retention Hydrologic Properties data from File MRCQ, Worksheet-CNWQ, Worksheet-BT4Q, Worksheet-TPYQ, Worksheet-BT3Q, Worksheet-TPPQ, Worksheet-BT2Q).
- 1a. Same as step 1a above except that no data are identified for TPY.
- 1b. Same as step 1b above except that no data are identified for TPY.
- 1c. Same as step 1c above except that no data are identified for TPY.
2. Same as step 2 above. This results in sample UZ16 171.7r begin reassigned from TPY to BT4 and sample SD9 74.1 being removed from BT3 (it is already assigned correctly to CNW).
3. Same as step 3 above.
- 3a. Same as step 3a above.
4. Same as step 4 above.
- 4a. Same as step 4a above.
5. Water content is plotted vs. water potential on worksheets 'PTn curves' and 'PTn curves (2)' for HGU groups CNW, BT4, and TPY and BT3, TPP, and BT2, respectively, with chilled-mirror psychrometer data shown in open diamond symbols. Each sample is shown in a different color.
- 5a. Centrifuge data are shown as filled circles. Each centrifuge sample is shown in a different color that is not necessarily different from the colors used for the chilled-mirror psychrometer data. Note: there are no centrifuge data for TPY.
6. Same as step 6 above.
7. Same as step 7 above.
8. Same as step 8 above.
9. Same as step 9 above.
10. Same as step 10 above. Results are plotted in worksheets 'PTn curves' and 'PTn curves (2)'.  
11. Same as step 11 above.
12. Same as step 12 above.
13. Same as step 13 above.
14. Same as step 14 above. Results are plotted in worksheets 'PTn curves' and 'PTn curves (2)'.  
15. Same as step 15 above. Results are plotted in worksheets 'PTn curves' and 'PTn curves (2)'.

16. Appropriate unsaturated conductivity data in worksheet '008 Kr' are identified as in step 1a above and are plotted as circles connected by a dashed line in worksheets 'PTn curves' and 'PTn curves (2)'. As in 3a, the appropriate saturation data are identified and highlighted in either column H or I in '008 Kr' by assuming that the highest water content measured for the sample represents full saturation.
17. Same as step 17 above except that the saturation match points are
  - CNW:  $S_0 = 0.85$ ,
  - BT4:  $S_0 = 0.65$ ,
  - BT3:  $S_0 = 0.95$ ,
  - TPP:  $S_0 = 0.80$ ,
  - BT2:  $S_0 = 0.83$ ,
 and there are no relative permeability data for TPY.
18. Same as step 18 above except the calculation is carried out in worksheet '008 Kr' in column M.
19. Same as step 19 above except the calculation is carried out in worksheet '008 Kr' in column N.
20. In worksheet '008 Kr', the squared error (difference) between the predicted relative permeability and the measured relative permeability is calculated in column X and summed in cells W18:W22 for each of the HGUs identified in cells V18:V22.
21. In worksheet '008 Kr', the solver function of Excel is used to estimate  $\eta$ , cells Z18:Z22, for each HGU identified in cells V18:V22 by minimizing the sum of the squared error for the same HGU, cells W18:W22. Note: all optional solver settings are default.
22. In worksheet '008 Kr', the Jacobian matrix is calculated numerically in column Y using the perturbed  $\eta$  value given in cells AA18:AA22. The variance and standard error of  $\eta$  are calculated in cells AB18:AB22 and AC18:AC22, respectively.
23. In worksheet '008 Kr', relative permeability is calculated in columns Q:U for a range of saturation values in column P. The results are plotted as an orange line in worksheets 'PTn curves' and 'PTn curves (2)'.
24. The average, minimum, and maximum in-situ saturation are plotted as a gray circle and error bars in worksheets 'PTn curves' and 'PTn curves (2)'.

### **MRC\_Q\_TSw\_fin.xls (OUTPUT-DTN: LB0207REVUZPRP.002)**

This file was used to develop matrix properties for UZ model layers.

Worksheets 'in-situ', '037 wc', '037 wp', '008 wp & wc(g per g)', '039 wc', '039 wp' are prepared as for MRC\_Q\_TCw\_fin.xls.

#### *Worksheet '007 S wp'*

- Import DTN: GS990308312242.007 [107185] (Busted Butte water retention data).
- Use data from DTN: LA0207SL831372.001 [160824] to make HGU assignments for each sample (column F).

*Worksheet '007 Ks'*

- Import DTN: GS990308312242.007 [107185] (Busted Butte hydraulic conductivity data).

*Worksheet '007 S K'*

- Import DTN: GS990308312242.007 [107185] (Busted Butte relative permeability data).
- Use data from DTN: LA0207SL831372.001 [160824] to make HGU assignments for each sample (column F).
- In column G, calculate relative permeability from conductivity in column E assuming that the saturated conductivity in worksheet '007 Ks' column H represents a relative permeability of one. Note: there is no saturated conductivity measurement for sample INJ-4-16.8B, so the highest conductivity measured is assumed to equal a relative permeability of one, and relative permeability is calculated in column H.

*Worksheet '99.008 S wp'*

- Import DTN: GS990708312242.008 [109822] (Busted Butte water retention data).
- Use data from DTN: LA0207SL831372.001 [160824] to make HGU assignments for each sample (column G).

*Worksheet '99.008 Ks'*

- Import DTN: GS990708312242.008 [109822] (Busted Butte hydraulic conductivity data).

*Worksheet '99.008 S K'*

- Import DTN: GS990708312242.008 [109822] (Busted Butte relative permeability data).
- Use data from DTN: LA0207SL831372.001 [160824] to make HGU assignments for each sample (column G).
- In column H, calculate relative permeability from conductivity in column E assuming that the saturated conductivity in worksheet '007 Ks' column H represents a relative permeability of one.

*Worksheet '012 wc'*

- Import DTN: GS980808312242.012 [149375] (USW WT-24 water retention water content data).
- Use data from hydroprops.xls worksheet 'borehole data' to make HGU assignments for each sample (column G).

*Worksheet '012 wp'*

- Import DTN: GS980808312242.012 [149375] (USW WT-24 water retention water potential data).
- Use data from hydroprops.xls worksheet 'borehole data' to make HGU assignments for each sample (column G).

*Worksheet '95.008 wc'*

- Import DTN: GS950608312231.008 [144662] (USW UZ-N27 and UE-25 UZ#16 water retention water content data). Note: for the most part, these data are already included under DTN: MO0109HYMXPROM.001 [155989], however, there are some additional data under this DTN.

*Worksheet '95.008 wp'*

- Import DTN: GS950608312231.008 [144662] (USW UZ-N27 and UE-25 UZ#16 water retention water potential data). Note: for the most part, these data are already included under DTN: MO0109HYMXPROM.001 [155989], however, there are some additional data under this DTN.

*Worksheets 'TC', 'TR', 'TUL', 'TMN', 'TLL', 'TM2 & TM1', 'PV3', 'PV2a', and 'PV2v'*

1. Import DTN: MO0109HYMXPROM.001 [155989] (water retention Hydrologic Properties data from File MRCQ, Worksheet-TCQ, Worksheet-TRQ, Worksheet-TULQ, Worksheet-TMNQ, Worksheet-TLLQ, Worksheet-TM2Q, Worksheet-TM1Q, Worksheet-PV3Q, Worksheet-PV2Q). Note: Data from Worksheet-TM2Q and Worksheet-TM1Q are combined in worksheet 'TM2 & TM1'.
  - 1a. Appropriate data from worksheets '037 wc' and '037 wp' are identified by the lithostratigraphy and ESF station in DTN: LAJF831222AQ98.014 [160825] and ESF station of contacts from Table 2 in CRWMS M&O (1998 [102679]) and are added to columns B, C, and E of worksheets 'TC' and 'TR'.
  - 1b. Appropriate data from worksheet '008 wp & wc(g per g)' are identified as in step 1a above are added to columns B, C, and E of worksheet 'TC'.
  - 1c. Appropriate data from worksheets '039 wc' and '039 wp' are added to columns B, C, and E of worksheets 'TC', 'TR', 'TM2 & TM1', and 'PV3'.
  - 1d. Appropriate data from worksheets '007 S wp' and '99.008 S wp' are added to columns B, D, and E of worksheet 'PV2v'.
  - 1e. Appropriate data from worksheets '012 wc' and '012 wp' are added to columns B, C, and E of worksheet 'PV2a'.
  - 1f. Appropriate data from worksheets '95.008 wc' and '95.008 wp' are added to columns B, C, and E of worksheets 'TLL' and 'PV3'.
2. Same as step 2 above.
  - 2a. Sample SD9-1440.5r is not within the PV2 and is removed.
3. Same as step 3 above except for worksheet 'PV2v' where data are given in terms of saturation rather than water content.

4. Same as step 4 above.
- 4a. Same as step 4a above.
5. Same as step 5 above.
- 5a. Same as step 5a above.
6. Same as step 6 above.
7. Same as step 7 above.
8. Same as step 8 above.
9. Same as step 9 above.
10. Same as step 10 above.
- 10a. Plotting the estimated function for PV3 shows that the shape of the curve does not match well with the data. The parameters ( $\alpha$  and  $n$ ) are adjusted by hand to improve the subjective match between the shape of the curve and the data. This adjustment results in an increase of 0.14 (16%) in the sum of the squared error.
11. Same as step 11 above.
12. Same as step 12 above.
13. Same as step 13 above.
14. Same as step 14 above.
15. Same as step 15 above.
16. In worksheet 'PV2v' only, appropriate unsaturated conductivity data from worksheets '007 S K' and '99.008 S K' are identified as in step 1d above, added to columns V, W, and X, and are plotted as circles connected by a dashed line.
17. In worksheet 'PV2v' only, same as step 17 under spreadsheet MRC\_Q\_TCw\_fin.xls, worksheet 'CMW', except  $S_{e,0} = 0.9$ .
18. In worksheet 'PV2v' only, same as step 18 under spreadsheet MRC\_Q\_TCw\_fin.xls, worksheet 'CMW'.
19. In worksheet 'PV2v' only, same as step 19 under spreadsheet MRC\_Q\_TCw\_fin.xls, worksheet 'CMW'.
20. In worksheet 'PV2v' only, same as step 20 under spreadsheet MRC\_Q\_TCw\_fin.xls, worksheet 'CMW'.
21. In worksheet 'PV2v' only, same as step 21 under spreadsheet MRC\_Q\_TCw\_fin.xls, worksheet 'CMW'.
22. In worksheet 'PV2v' only, same as step 22 under spreadsheet MRC\_Q\_TCw\_fin.xls, worksheet 'CMW'.
23. In worksheet 'PV2v' only, same as step 23 under spreadsheet MRC\_Q\_TCw\_fin.xls, worksheet 'CMW'.
24. In worksheet 'PV2v' only, same as step 24 under spreadsheet MRC\_Q\_TCw\_fin.xls, worksheet 'CMW'.

### **MRC\_Q\_CHCF\_fin.xls (OUTPUT-DTN: LB0207REVUZPRP.002)**

This file was used to develop matrix properties for UZ model layers.

Worksheets 'in-situ', '039 wc', '039 wp', '007 S wp', '007 Ks', '007 S K', '99.008 S wp', '99.008 Ks', '99.008 S K', '012 wc', '012 wp', '95.008 wc', and '95.008 wp' are prepared as for MRC\_Q\_TSw\_fin.xls.

*Worksheet '001 wc wp'*

- Import DTN: GS010608312242.001 [160822] (Busted Butte water retention data).

- Use data from DTN: LA0207SL831372.001 [160824] to make HGU assignments for each sample (column F).

*Worksheet '001 wc K'*

- Import DTN: GS010608312242.001 [160822] (Busted Butte relative permeability data).
- Use data from DTN: LA0207SL831372.001 [160824] to make HGU assignments for each sample (column G).
- In column I, calculate the saturation from water content in column D assuming that the highest water content listed for the same sample in worksheet '001 wc wp' (if measured) is the water content at full saturation.
- In column J, calculate the saturation from water content in column D assuming that the highest water content listed for each sample is the water content at full saturation.
- In column K, calculate relative permeability from conductivity in column E assuming that the highest conductivity for each sample is the saturated conductivity.

*Worksheet '96.003 wp wc'*

- Import DTN: GS960808312231.003 [147590] (USW SD-7, USW SD-9, USW SD-12, and UE-25 UZ#16 water retention data). Note: for the most part, these data are already included under DTN: MO0109HYMXPROP.001 [155989], however, there are some additional data under this DTN.

*Worksheets 'BT1v', 'BT1a', 'CHV', 'CHZ', 'BTv', 'BTa', 'PP4', 'PP3', 'PP2', 'PP1', 'BF3', and 'BF2'*

1. Import DTN: MO0109HYMXPROP.001 [155989] (water retention Hydrologic Properties data from File MRCQ, Worksheet-BT1aQ, Worksheet-CHZQ, Worksheet-BTQ, Worksheet-PP4Q, Worksheet-PP3Q, Worksheet-PP2Q, Worksheet-PP1Q, Worksheet-BF3Q, Worksheet-BF2Q). Note: Data from Worksheet-BTQ are assigned to HGU BTa; no data are identified in this DTN for HGUs BT1v, CHV, and BTv.
  - 1a. Appropriate data from worksheets '039 wc' and '039 wp' are added to columns B, C, and E of worksheets 'BT1v', 'CHV', 'BTv', 'PP4', 'PP3', and 'BF3'.
  - 1b. Appropriate data from worksheet '99.008 S wp' are added to columns B, D, and E of worksheets 'BT1v' and 'CHV'.
  - 1c. Appropriate data from worksheet '007 S wp' are added to columns B, D, and E of worksheet 'BT1v'.
  - 1d. Appropriate data from worksheets '001 wc wp' are added to columns B, C, and E of worksheets 'BT1v' and 'CHV'.
  - 1e. Appropriate data from worksheets '012 wc' and '012 wp' are added to columns B, C, and E of worksheets 'BT1a' and 'CHZ'.
  - 1f. Appropriate data from worksheets '95.008 wc' and '95.008 wp' are added to columns B, C, and E of worksheets 'CHZ', 'PP4', 'PP2', and 'PP1'.
  - 1g. Appropriate data from worksheet '96.003 wc wp' are added to columns B, C, and E of worksheet 'CHV'.
2. Same as step 2 above.

- 2a. Sample SD9-1440.5r, which was not within PV2 (see step 2a above) is within the BT1v and is added.
3. Same as step 3 above except for data from worksheets '007 S wp' and '99.008 S wp' where data are given in terms of saturation rather than water content.
- 3a. The saturation for the data from 1d is calculated assuming that the highest water content from either worksheet '001 wc wp' or '001 wc K' for that sample represents the water content at full saturation.
4. Same as step 4 above.
- 4a. Same as step 4a above.
5. Same as step 5 above.
- 5a. Same as step 5a above.
6. Same as step 6 above.
7. Same as step 7 above.
8. Same as step 8 above.
9. Same as step 9 above.
10. Same as step 10 above.
- 10a. Plotting the estimated function for PP4 shows that the shape of the curve does not match well with the data. The parameters ( $\alpha$  and  $n$ ) are adjusted by hand to improve the subjective match between the shape of the curve and the data. This adjustment results in an increase of 0.951 (65%) in the sum of the squared error.
11. Same as step 11 above.
12. Same as step 12 above.
13. Same as step 13 above.
14. Same as step 14 above.
15. Same as step 15 above.
16. In worksheets 'BT1v' and 'CHV' only, appropriate unsaturated conductivity data from worksheets '99.008 S K', '007 S K', and '001 wc K' are identified as in steps 1b, 1c, and 1d above, added to columns V, W, and X, and are plotted as circles connected by a dashed line.
- 16a. As in step 3a above, the saturation for the data from '001 wc K' is calculated assuming that the highest water content from either worksheet '001 wc wp' or '001 wc K' for that sample represents the water content at full saturation.
17. In worksheets 'BT1v' and 'CHV' only, same as step 17 above.
18. In worksheets 'BT1v' and 'CHV' only, same as step 18 above.
19. In worksheets 'BT1v' and 'CHV' only, same as step 19 above.
20. In worksheets 'BT1v' and 'CHV' only, same as step 20 above.
21. In worksheets 'BT1v' and 'CHV' only, same as step 21 above.
22. In worksheets 'BT1v' and 'CHV' only, same as step 22 above.
23. In worksheets 'BT1v' and 'CHV' only, same as step 23 above.
24. In worksheets 'BT1v' and 'CHV' only, same as step 24 above.

**vG\_Summary\_fin.xls (OUTPUT-DTN: LB0207REVUZPRP.002)**

This file was used to develop matrix properties for UZ model layers.

Note: This spreadsheet contains links to hydroprops\_fin.xls, MRC\_Q\_TCw\_fin.xls, MRC\_Q\_PTn\_fin.xls, MRC\_Q\_TSw\_fin.xls, and MRC\_Q\_CHCF\_fin.xls; these spreadsheets must be open at the same time this spreadsheet is open.

*Worksheet 'vG Summary'*

All values shown in columns C, D, E, G, H, and J are linked to the spreadsheets (above) where they are estimated.

Values of  $\eta$  and  $\sigma_\eta$  (columns L and M) for CMW, CNW, BT4, BT3, TPP, BT2, PV2v, BT1v, and CHV are those estimated by fitting relative permeability data. All other values of  $\eta$  and  $\sigma_\eta$  are estimated as

$$\eta = Am - B \log(k) + C$$

and

$$\sigma_\eta = (A + \sigma_A)m - (B + \sigma_B)\log(k) + (C + \sigma_C) - \eta$$

where  $m$  is the van Genuchten parameter,  $k$  is upscaled permeability, and  $A$ ,  $B$ , and  $C$  are fitting parameters. Note: the minus sign before  $B$  is because  $\eta$  is correlated to  $\log(k^{-1})$ . The fitting parameters are estimated in worksheet 'fitted kr'.

*Worksheet 'fitted kr'*

For each layer, column A, where  $\eta$ , column D, has been estimated from relative permeability data, the estimates of upscaled permeability, column B, and the van Genuchten parameter  $m$ , column C, are given.

The parameter  $\eta$  is predicted in column E using the equation given above and the parameters in cells F1:F3. The squared difference between the two values of  $\eta$  is calculated in column F and summed in cell F4.

The Jacobian matrix (see step 11 under spreadsheet MRC\_Q\_TCw\_fin.xls worksheet CUC) is calculated in columns G – I using the perturbed parameter values in cells G1:G3. The covariance matrix (see step 12 under spreadsheet MRC\_Q\_TCw\_fin.xls worksheet CUC) is calculated in cells K5:M7. The standard error (see step 13 under spreadsheet MRC\_Q\_TCw\_fin.xls worksheet CUC) is calculated in cells K1:K3. The parameter values perturbed by one standard error are given in cells N1:N3.

**PV2 deep borehole data.xls (OUTPUT DTN: LB0207REVUZPRP.002)**

This file was used to develop matrix properties for UZ model layers.

This spreadsheet is a copy of cells B3756:U3793 from hydroprops\_fin.xls worksheet 'hydroprops'. Note: column A in this spreadsheet should be ignored.

**lecan97.xls** (output DTN: LB0205REVUZPRP.001)

This file was used for estimating fracture parameters.

In this spreadsheet, only the workbook "New Layers" was used to calculate fracture permeability for UZ model layers that have been documented in the Model Report. Therefore, the documentation is limited to this workbook.

In this spreadsheet, columns A, B, and C contain data from DTN: GS960908312232.013 [105574]. Column D corresponds to log of air permeability calculated from column C. Columns H, I, J contain total number of air k measurements, average of log of air permeability and standard deviation of log(air permeability) for each geologic unit within a single borehole, respectively. Columns L, M, N contain total number of air k measurements, average of log of air permeability and standard deviation of log(air permeability) for each geologic unit for all the boreholes, respectively.

**UTCA\_BRFA.xls** (output DTN: LB0205REVUZPRP.001)

This file was used for estimating fracture parameters.

In this spreadsheet, there are two notebooks UPCA and UTCA\_BRFA. In UPCA, columns A-E contain data from Alcove 3 (DTN: GS970183122410.001 [105580]). Column F corresponds to log of air permeability calculated from column C. Columns H, I and J contain total number of air k measurements, average of log of air permeability and standard deviation of log(air permeability) for each geologic unit within a single borehole (labeled as "location"), respectively. Columns M, N and O contain total number of air k measurements, average of log of air permeability and standard deviation of log(air permeability) for each geologic unit for all the boreholes, respectively.

In UTCA\_BRFA, columns C-E contain data from Alcove 1 (DTN: GS970183122410.001 [105580]). Column F corresponds to log of air permeability calculated from column E. Columns H, I, J, K contain total number of air k measurements, geometric mean of air k, log of geometric mean of air permeability and standard deviation of log(air permeability) for each geologic unit within a single borehole (labeled as "location"), respectively. Columns V, W and X contain total number of air k measurements, average of log of air permeability and standard deviation of log(air permeability) for each geologic unit for all the boreholes, respectively.

**drift.xls** (Output DTN: LB0205REVUZPRP.001)

In this spreadsheet, column D contains air permeability data from DTNs: LB970600123142.001 [105589], LB980120123142.004 [105590], LB980120123142.005 [114134], and LB960500834244.001 [105587]. Column E corresponds to log of permeability values calculated from column D. Columns J and K contain total number of air permeability measurements, geometric mean of log of air permeability and standard deviation of log(air permeability), respectively.

**airk.xls** (output DTN: LB0205REVUZPRP.001)

This file was used for estimating fracture parameters.

Since the equations used in the spreadsheet are simple standard functions of MS Excel, the supplementation needed here is a description of the specific cells that contain the input, output and calculation used in the spreadsheet application. A description of the equations is provided. This spreadsheet is linked to lecan97.xls, drift.xls and UTCA\_BRFA.xls that discussed above.

In this spreadsheet, only the work book “New Layers” was used to calculate fracture permeability for UZ model layers that has been documented in the Model Report. Therefore, the documentation is limited to this workbook. This spreadsheet calculates layer-averaged fracture permeability information based on air k data contained in lecan97.xls, UTCA\_BRFA.xls and drift.xls.

In the workbook “New Layers”, columns A, B, C, and D contain model layer name, total number of air k measurements from different sources, mean of log(air permeability), and the standard deviation of log(air permeability), respectively.

To demonstrate the calculation procedure, model layer tcw12 is used as an example. In this discussion subscripts 1, 2, 3 refer to data from Lecan97.xls, UTCA (UTCA\_BRFA.xls) and UPCA (UTCA\_BRFA.xls), respectively.

1. Cell B5 contains the total number of measurements, denoted by N, that was calculated as follows: Cells J4-J6 contain the number of measurements from the three data sources ( $N_1$ ,  $N_2$  and  $N_3$ ), respectively, by linking with the relevant cells in lecan97.xls and UTCA\_BRFA.xls). The total number is given in Cell J7 calculated by

$$N = N_1 + N_2 + N_3$$

The value in Cell J7 was then assigned to B5.

2. Cell C5 contains the mean of log(air permeability) ( $X_m$ ) that was calculated as follows: Cells K4-K6 contain the means from the three data sources ( $X_{m1}$ ,  $X_{m2}$  and  $X_{m3}$ ), respectively, by linking with the relevant cells in lecan97.xls and UTCA\_BRFA.xls. Values in cells P4-P6 are calculated as  $N_1 X_{m1}$ ,  $N_2 X_{m2}$ , and  $N_3 X_{m3}$ . Cell P7 summates values in the three cells. Then, the mean  $X_m$  was stored in cell K7 and calculated by

$$X_m = (N_1 X_{m1} + N_2 X_{m2} + N_3 X_{m3}) / N = (\text{the value in cell P7}) / (\text{the value in cell J4})$$

The value in K7 was assigned to C5.

3. Cell D5 contains standard deviation of log(air permeability) ( $\sigma$ ) that was calculated as follows: Cells L4-L6 contain the standard deviation values from the three data sources ( $\sigma_1$ ,  $\sigma_2$  and  $\sigma_3$ ), respectively, by linking with the relevant cells in lecan97.xls and UTCA\_BRFA.xls. Variances in cells N4-N6 ( $\sigma_1^2$ ,  $\sigma_2^2$  and  $\sigma_3^2$ ) were then calculated from cells L4-L6. Cells Q4 was calculated by

$$\frac{(N_1 X_{1m})^2 + \sigma_1^2 N_1 (N_1 - 1)}{N_1} = \sum_{i=1}^{N_1} x_i^2$$

where  $x_i$  refers to log(air permeability) for measurement  $i$ . Similar calculations were performed for the other two data sources. Cell Q7 summates values in the three cells Q4-Q6. The value in Q7 corresponds to

$$\sum_{i=1}^N x_i^2$$

where N is the total number of measurements from the three data sources. If using the cell names to represent values in them, N7 was calculated as

$$N7 = \frac{J7Q7 - (P7)^2}{J7(J7 - 1)} = \frac{N \sum_{i=1}^N x_i^2 - (NX_m)^2}{N(N - 1)} = \frac{\sum_{i=1}^N (x_i - X_m)^2}{N - 1}$$

By definition, N7 is the overall variance of log(air permeability) for air k data from the three data sources. L7 contains the corresponding standard deviation calculated from N7. Its value was assigned to D5.

The similar procedure was used for all the model layers that have measurement from different sources. If a model layer only has data from a single source (lecan97.xls, drift.xls and UTCA\_BRFA.xls), the above calculation procedure was not needed. The relevant value can be directly obtained from the data source. Also in the spreadsheet, some standard deviation values were assigned to model layers that only contain one measurement. These values were not used.

**Fpor.xls** (output DTN: LB0205REVUZPRP.001)

This file was used for estimating fracture parameters.

'Sheet 1' contains fracture porosity values calculated from other sources (Section 6.1.3.4). The input sources and calculations are explicitly indicated in the workbook.

In 'sheet2', Column A contains names of UZ model layers and Column C contains the corresponding aperture values (output DTN: LB0205REVUZPRP.001). Column E contains van Genuchten  $\alpha$  calculated using Equation (9). Column G contains fracture intensity or frequency values (DTN: LB990501233129.001 [106787]). Column I contains fracture porosity values calculated from Equation (12). Column M contains log( $\alpha$ ) values. Below Row 32 was used for estimating fracture porosity for tsw34. The input sources and calculations are explicitly indicated in the workbook for this estimation.